Remote epitaxy of cubic gallium nitride on graphene-covered 3C-SiC substrates

Presented to the Faculty of Science
Department of Physics
Paderborn University

In partial fulfillment of requirements
for the degree of
Dr. rer. nat.

Dissertation

By

Mario Littmann

Abstract

The remote epitaxy is a relatively new method that offers several advantages. Among other things, it allows to reduce the influence of lattice mismatches and the possibility of detaching epitaxial layers from the substrate. This scientific work investigates the possibility of applying this new technique to the growth of metastable cubic gallium nitride. For this purpose, a graphene-covered 3C-SiC/Si (001) pseudosubstrate is used. The additional graphene layer is a 2D material that only forms covalent bonds within itself and acts as a barrier that prevents the formation of covalent bonds between the substrate and the epitaxial layer. Because of this, the interaction between the epilayer and substrate is only limited to Van-der-Waals forces. A significant challenge hereby is the nucleation of the metastable cubic phase, which is hindered due to the weak interaction between the substrate and the epitaxial layer.

The initial attempts to apply remote epitaxy resulted in polycrystalline and hexagonal layers. Optimizing the substrate temperature and introducing an additional cubic aluminum nitride buffer layer improved the layer quality. The fabricated samples were analyzed and evaluated using various characterization methods, such as high-resolution X-ray diffraction and scanning electron microscopy. These techniques provide valuable insights into the effects of optimized growth parameters and the quality of the cubic GaN layer. High-resolution X-ray diffraction measurements confirmed that the proportion of hexagonal inclusions could be reduced from 80% to 23%.

However, the current layer quality is limited by the transfer graphene used. This kind of graphene consists of many small domains and incorporates further defects due to the transfer process. Electron backscatter diffraction measurements indicate that the majority of the hexagonal inclusions are located around these defects. This suggests that further improvement can be achieved by using a different kind of graphene creation process.

Kurzfassung

Die Remote Epitaxie ist eine relativ neue Methode, die mehrere Vorteile bietet. Unteranderem ermöglicht sie den Einfluss von Gitterfehlpassungen zu reduzieren und die Möglichkeit, Epitaxieschichten von dem Substrat abzulösen. Diese wissenschaftliche Arbeit untersucht die Möglichkeit dieses neue Verfahren für das Wachstum von metastabilen kubischem Galliumnitrid anzuwenden. Hierzu wird ein mit Graphen bedecktes 3C-SiC/Si (001) Pseudosubstrat verwendet. Das Graphen ist ein 2D Material, welches keine kovalenten Bindungen zu anderen Schichten aufbaut. Auf diese Weiße fungiert das Graphen als eine Art Barriere, die es verhindert, dass der Epitaxieschicht direkte Bindungen mit dem Substrat aufbauen kann. Die größte Herausforderung hierbei ist die Nukleation der metastabilen kubischen Phase, welche aufgrund der schwachen Wechselwirkung zwischen dem Substrat und der Epitaxieschicht erschwert wird. Die ersten Versuche die Remote Epitaxie anzuwenden resultierten in polykristallinen und hexagonalen Schichten. Die Optimierung der Substrattemperatur und die Einführung einer zusätzlichen kubischen Aluminiumnitrid-Pufferschicht ermöglichten eine Verbesserung der Schichtqualität.

Die hergestellten Proben wurden mit verschiedenen Charakteriesrungsmethoden, wie zum Beispiel hochauflösender Röntgendiffraktometrie und Rasterelektronenmikroskopie analysiert und bewertet. Diese Techniken liefern wertvolle Erkenntnisse über die Auswirkungen der optimierten Wachstumsparameter und die Qualität der kubischen GaN-Schicht. Hochauflösende Röntgendiffraktionsmessungen bestätigten, dass der Anteil hexagonaler Einschlüsse von 80% auf 23% reduziert werden konnte.

Die aktuelle Schichtqualität wird jedoch durch das verwendete Transfergraphen begrenzt. Diese Art von Graphen besteht aus vielen kleinen Domänen und weist aufgrund des Transferprozesses weitere Defekte auf. Elektronenrückstreudiffraktometrie Messungen deuten darauf hin, dass der Großteil der hexagonalen Einschlüsse um diese Defekte herum lokalisiert ist. Dies legt nahe, dass durch die Verwendung eines anderen Herstellungsverfahrens für das Graphen weitere Verbesserungen erzielt, werden können.

Acronyms

Abbreviation	Definition
AFM	Atomic force microscope
BOE	Buffered oxide etch
BSF	Basal stacking fault
BX	Bound exciton
CCD	Charge coupled device
CVD	Chemical vapor deposition
EBSD	Electron backscatter diffraction
FWHM	Full-width half maximum
FX	Free exciton
HF	Hydrofluoric acid
HRXRD	High-resolution x-ray diffraction
LASER	Light amplification by stimulated emission of radiation
LED	Light-emitting diode
MBE	Molecular beam epitaxy
MOCVD	Metalorganic chemical vapor deposition
PAMBE	Plasma-assisted molecular beam epitaxy
PL	Photoluminescence
PMMA	Polymethyl methacrylate
QCSE	Quantum-confined Stark effect
QMS	Quadrupole mass spectrometer
QW	Quantum well
RF	Radiofrequency
RHEED	Reflection high-energy electron diffraction
RSM	Reciprocal space map

SEM	Scanning electron microscope
SF	Stacking fault
TMP	Turbomolecular pump
VESTA	Visualization for Electronic and Structural Analysis (Software)

Table of Contents

1. Introduction

Group III nitrides, primarily comprising the elements gallium (Ga), indium (In), and aluminum (Al), are semiconductor materials that have garnered significant attention in the electronic and optoelectronics industries[1]. Their exceptional physical and chemical properties, including a wide bandgap, make them irreplaceable for the development of cutting-edge optoelectronic devices, such as light-emitting diodes (LEDs) and lasers and high-power electronics[2,3]. The wide bandgap of these materials allows them to operate efficiently at higher temperatures, enhancing their durability. However, one inherent challenge associated with the use of group III nitrides is the wurtzite crystal structure, which can lead to the quantum-confined Stark effect (QCSE). The QCSE can potentially diminish the efficiency of devices, prompting researchers to explore alternatives like the meta-stable cubic GaN. However, the growth of cubic nitrides is already challenging because they can only be synthesized by heteroepitaxy with high lattice mismatch. The additional challenge of growing the metastable zincblende phase makes it more difficult to grow high-quality nitride layers.

While a widely used method for semiconductor synthesis, heteroepitaxy brings some limitations, particularly the need for a compatible substrate material. The quality of the grown films depends heavily on the lattice mismatch between the epitaxial layer and the chosen substrate. A high lattice mismatch can have a negative influence by enhancing the formation of defects that reduce the efficiency of devices. Recently, different approaches have been tested to modify the heteroepitaxial process to reduce the influence of the lattice mismatch. One of these methods is the remote epitaxy process [4].

The remote epitaxy has been an area of intense research in recent years[5]. While it offers to reduce the influence of the lattice mismatch[6], it further introduces the possibility of an easy-to-perform lift-off process. This brings additional benefits like the possibility of reusing the necessary expensive substrate material. Additionally, it is possible to use this for material systems where no selective etching process for releasing the layer exists[7] C. Youtsey, R. McCarthy, P. Fay, in Semiconductors and Semimetals, Elsevier 2019.. Several studies have already demonstrated these advantages[5,8–10]. The process of remote epitaxy has been successfully applied for various materials like wurtzite nitrides[11] as well as arsenides [10,12]. In these studies, the epitaxy was performed by metal oxide chemical vapor deposition (MOCVD) and molecular beam epitaxy (MBE).

This work discusses the adaptation of the remote epitaxy process for the cubic zincblende gallium nitride. This is a novel application to use the remote epitaxy for the growth of a meta-stable phase. The conventional method of growing cubic GaN has been on (001) zincblende silicon carbide (3C-SiC), which despite having the smallest possible lattice mismatch of 3.2%, is still susceptible to considerable defect formation. The remote epitaxy process was employed to address this problem. A monolayer thin layer of the 2D material graphene was placed between the substrate and the epitaxial layer. This graphene layer, only bonds to the substrate through van-der-Waals forces and not covalent bonds, reducing the interactions between the substrate and the epitaxial layer. In an ideal case, the dangling bonds of the underlying crystal structure influence the adatoms during the epitaxy step to guide them into the desired crystal phase.

2. Fundamentals

The following chapter delves into the fundamental physical properties and characteristics that are important to understand this thesis. Firstly, the unique properties of the group-III nitrides are described. The chapter starts with the basic bandgap energies and crystal phases and delves later into the negative aspects like the quantum-confined Stark effect and the influence of a high lattice mismatch for heteroepitaxy processes. This is followed by a detailed description of the remote epitaxy process and a description of the properties and synthetic methods to create graphene.

2.1 Nitrides

One of the most important groups of semiconductor materials is the group III nitrides. They refer to compounds formed between the elements Aluminum (Al), Gallium (Ga), Indium (In), and Nitrogen (N). They possess unique physical and chemical properties, making them extremely valuable for various applications in optoelectronics and power electronics. The most important characteristic is the wide band gap. The bandgap of the alloys can range from 0.8 eV to 6.1 eV. This includes the complete visible light spectrum and reaches into the ultraviolet range. Figure 1 shows the unique bandgap compared to the other essential semiconductor materials. They are also direct band gap materials, which makes them suitable for optoelectronic applications like light-emitting diodes (LEDs) and LASER diodes.[3]

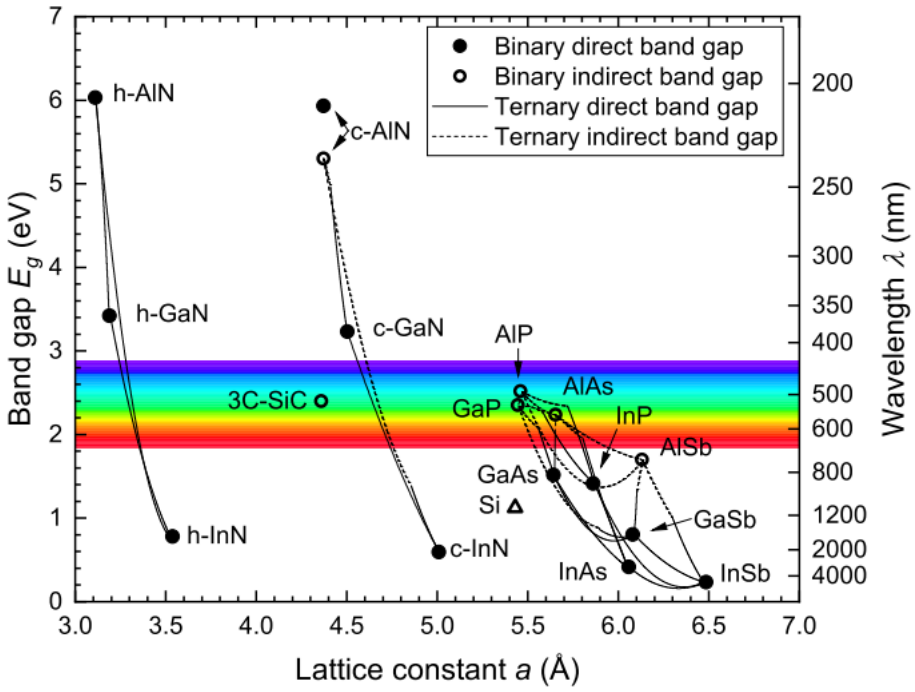

Figure 1: Band gap E_g versus the lattice constant a of the most important III-V semiconductors. Taken from [13].

The high bandgap also allows them to withstand high voltages, electric fields, and temperatures. In particular, GaN and AlN are mechanically and chemically resistant. In this work, we will concentrate on the GaN material.

However, there are also two crucial drawbacks. First, the nitrides stable phase is the hexagonal wurtzite structure. This can be a disadvantage for optoelectronic applications.

Inside the wurtzite structure, the length of the atomic bonds is different in the [0001] direction. Due to the polarized bond between the gallium and nitrogen atoms, an electric field is created inside the crystal. The different crystal lattices for the wurtzite and zincblende structure are visualized in Figure 2.

Inside a quantum well, this electric field will cause the quantum-confined Stark effect (QCSE).

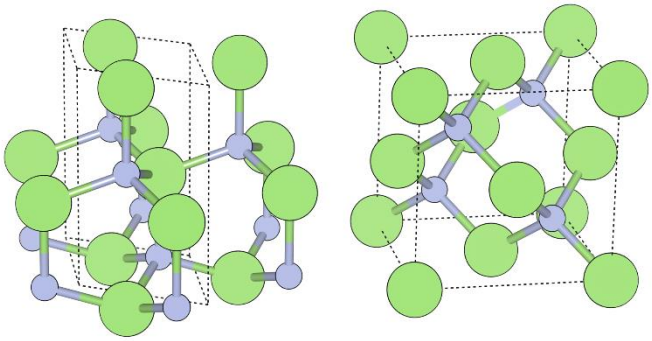

Figure 2: Sketch of the wurtzite and zincblende structure created with VESTA[14]

2.2 Quantum-confined Stark effect

The quantum-confined Stark effect is a phenomenon that is observed in quantum wells (QWs), which are inside an electric field. One example of this are InGaN/GaN quantum wells. The internal electric fields of the polarized bonds in the (0001) direction will cause this effect. In essence, the QCSE leads to a reduction in the overlap of the electron and hole wave function. An example of the wavefunctions inside a quantum well with and without an electric field is visualized in Figure 3. The electric field forces the electrons toward the minimum of the conduction band (in this case, the left side). On the other side, the holes are moved in the opposite direction (the right side). This reduces the recombination probability due to the spatial separation of the electron and holes. Consequently, the recombination rate is also reduced. This can have a subsequential impact on the device performance of LEDs.[15,16]

The transition probability can be increased by reducing the width of the quantum well. A thinner QW will reduce the separation of the electrons and holes. However, this method will only reduce the impact of the QCSE and will not completely overcome it. Furthermore, thinner QWs also have other problems, like a lower capture rate of electrons. Additionally, a requirement for thin QWs also complicates the optimization of the emitting wavelength.

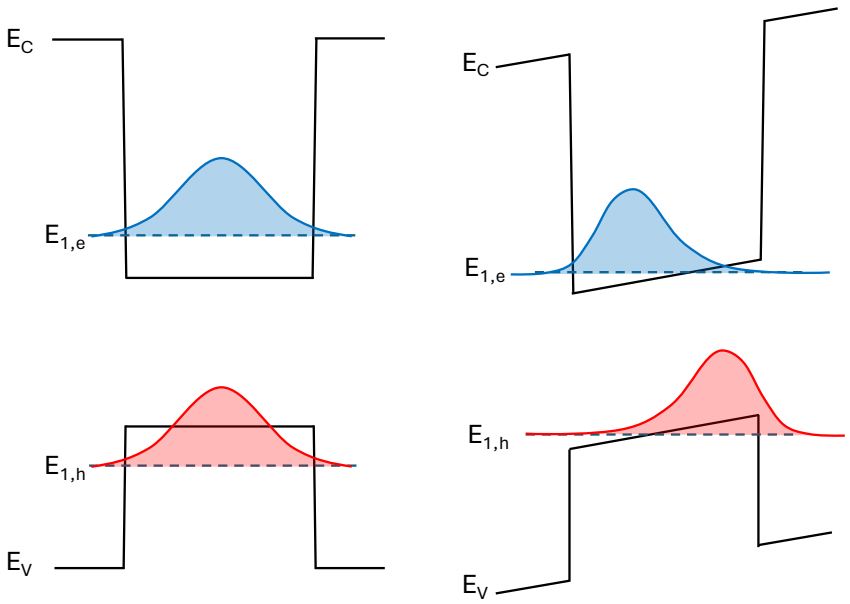

Figure 3: Illustration of the wave function for a quantum well without an electric field (left) and within an electric field (right). The electric field forces the electrons toward the minimum of the conduction band, while the holes are moved in the opposite direction. The spatial separation reduces the recombination rate. This effect is the QCSE.

2.3 Cubic gallium nitride

The solution to this problem would be to change the crystal structure. Even though the wurtzite structure is the preferred phase of the nitrides, it is possible to grow them in the zincblende structure. The bond length is the same in every direction compared to the wurtzite structure. The zincblende structure can be grown using a substrate material already in the cubic phase and oriented in the (001) direction. The epitaxial-grown gallium nitride layer can then be forced into the metastable zincblende phase. Gallium nitride grown in the zincblende structure is referred to as cubic gallium nitride (c-GaN).[16]

Table 1: Characteristic values of the lattice constant and band gap for the nitrides AlN, GaN and InN. The table contains the values for the wurtzite (wz) and zincblende (zb) phases.

	AlN	GaN	InN
a_{zb}	4.373 Å[17]	4.503 Å[18]	5.01 Å[19]
a_{wz}	3.1106 Å [20]	3.189 Å [20]	2.538 Å[20]
c_{wz}	4.9795 Å [20]	5.1864 Å [20]	5.703 Å[20]
$E_{g,zb}$	5.93 eV [21]	3.23 eV[22]	0.595 eV[19]
$E_{g,wz}$	6.03 eV [20]	3.42 eV [20]	0.78 eV[20]

2.4 Epitaxy

Gallium nitride can be epitaxially grown using metal-organic chemical vapor deposition (MOCVD) or molecular beam epitaxy (MBE). It is well known that the most used method for commercial purposes is the MOCVD. However, the MBE has many advantages in comparison. Due to the higher precision, it allows for abrupt interfaces and sharper doping profiles. Furthermore, the MBE system allows superior in situ growth control by using reflective high-energy electron diffraction (RHEED). Due to these benefits, the MBE system is especially useful for research applications, where a high production efficiency is not essential.[23]

There are two concepts of Nitride MBEs. They differ in the used nitrogen source. The first one is the ammonia MBE. In this case, the nitrogen is supplied in an ammonia molecule. The nitrogen will be separated from the hydrogen atoms at the substrate surface. This reaction is comparable to the CVD process. However, a disadvantage is that it induces hydrogen atoms into the growth chamber. Removing light atoms, like hydrogen, with pumps is especially difficult. Furthermore, ammonia requires a high growth temperature, and the corrosive nature of ammonia can have a negative impact.[23]

The second nitride MBE system is a plasma-assisted molecular beam epitaxy (PAMBE). In this case, the nitrogen is supplied by a radiofrequency plasma source. The nitrogen molecules are broken into separate nitrogen ions, free to be integrated into the crystal.

Since gallium nitride can only be epitaxially produced, performing homoepitaxy is impossible. Therefore, both the hexagonal gallium nitride (h-GaN) and the c-GaN can only be grown heteroepitaxial with a high lattice mismatch. This is also why it was challenging to grow single crystalline gallium nitride in the first place.

2.5 Lattice mismatch

In the case of c-GaN, the best possible substrate material is the cubic silicon carbide (3C-SiC). The lattice constant of c-GaN is 4.503 Å[18], and the lattice constant of 3C-SiC is 4.3596 Å[24]. The lattice mismatch can be calculated by the following formula. The lattice constant of the substrate material is $a_{sub,}$ and the lattice constant of the epitaxial layer is a_{epi}.[25]

$$f = \frac{a_{sub} - a_{epi}}{a_{epi}}$$

The lattice mismatch for these two materials is 3.2%. Compared to other semiconductor materials, like in the arsenides, this value is very high and induces a lot of strain in the layer. If the strain becomes too high, it will relax. This will lead to the formation of defects such as dislocations and stacking faults. A true-to-scale visualization of the different lattice constants of 3C-SiC and c-GaN is shown in Figure 4.

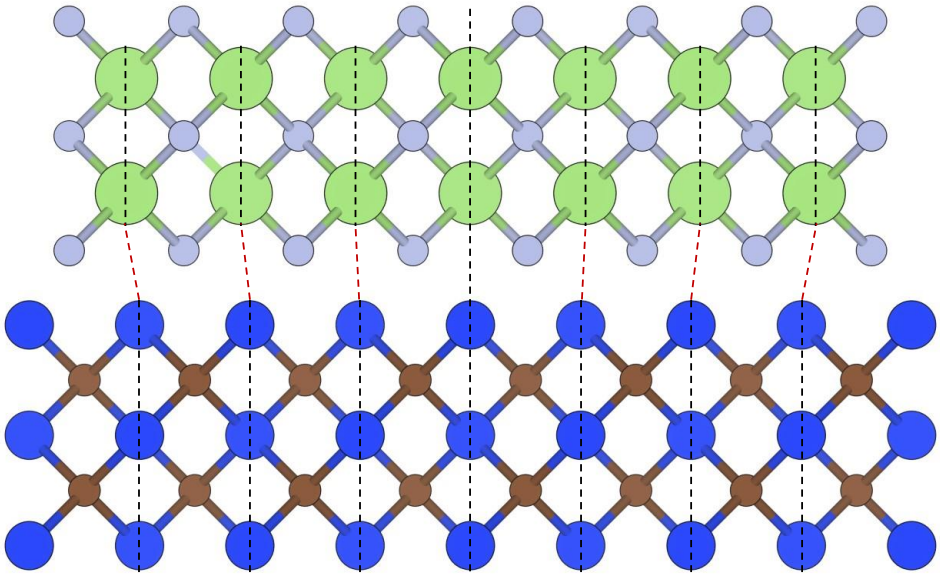

Figure 4: Visualization of the true-to-scale lattice mismatch between 3C-SiC and c-GaN. Si atoms are blue, carbon atoms are brown, nitrogen atoms are grey, and gallium atoms are green. Created with VESTA[14].

Figure 5 a) is a schematic sketch of a pseudomorph layer grown on a substrate with a smaller lattice constant. The distance between the atoms of the layer parallel to the interface is matched to the substrate. This induces strain, which results in a larger distance vertically to the interface. If the strain becomes too large, the layer is tempted to form dislocations to release the stress. An example of a dislocation is shown in Figure 5 b).

This point is called the critical thickness. It is the maximum thickness of a layer above which the strain becomes too high. The exact value always depends on the used materials and their lattice mismatch. Furthermore, the growth conditions will also affect the critical thickness. The growth temperature will significantly affect the strain due to the different thermal expansion coefficients.

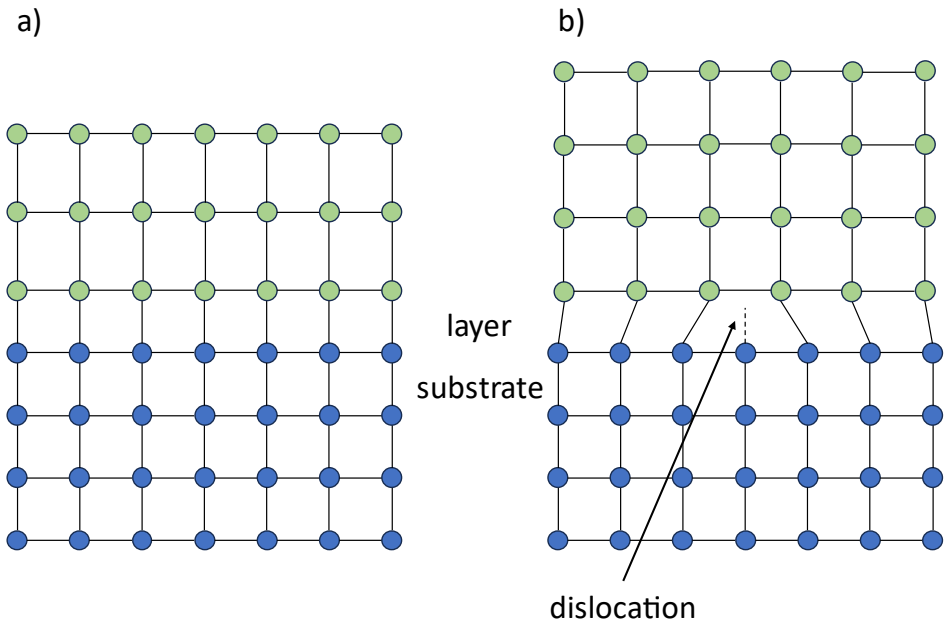

Figure 5: Schematic sketch of a) a pseudomorph layer grown on a substrate with a smaller lattice constant and b) a layer above the critical thickness. The strain of the film was relaxed through the formation of a dislocation.

An ideal material system like gallium arsenide and aluminum arsenide only has a lattice mismatch of 0.1%, which results in a critical thickness of several hundred nanometers. The critical thickness of c-GaN on a 3C-SiC substrate is about 0.7 nm.[26,27] Due to this, growing a low defect layer of GaN is challenging.

These defects will reduce the layer quality and affect the electrical, optical and mechanical properties. The dislocations can act as additional donors or acceptors, which can impact the carrier concentration and trap carriers. Furthermore, they act as scattering centers for charge carriers and reduce mobility. Additionally, they can serve as recombination centers and reduce the carrier lifetime. This will reduce the efficiency of optical devices such as solar cells and photodetectors, which require a long carrier lifetime. Furthermore, these unwanted recombinations will reduce the quantum efficiency of light-emitting diodes and lasers.[25]

2.6 Modes of thin film growth

Three different growth modes can describe the nucleation process during heteroepitaxial growth. These modes vary by how the atoms arrange themselves on the substrate surface during deposition. The three main types of growth modes are: Frank-van der Merwe, Volmer-Weber, and Stranski-Krastanov. The different growth modes are visualized in Figure 6.

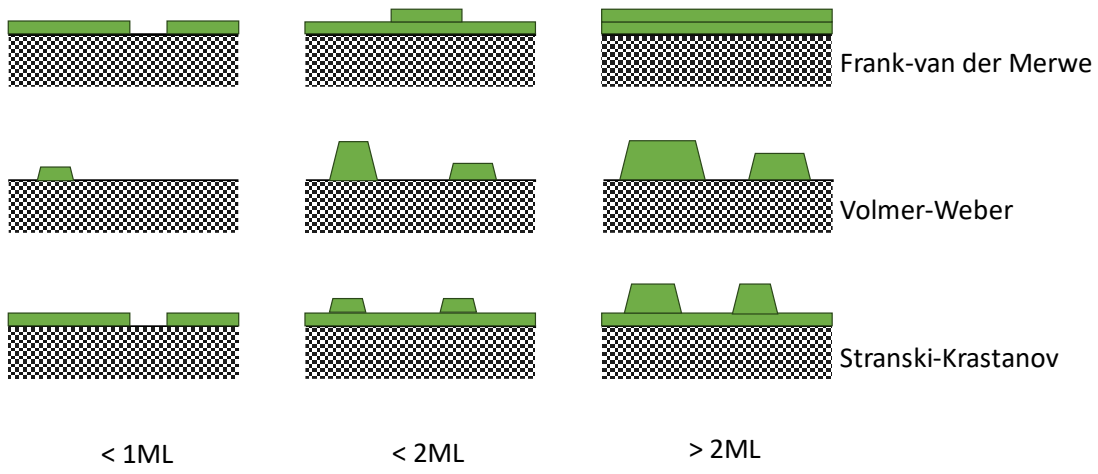

Figure 6: Visualization of the three different growth modes for heteroepitaxy. Frank-van der Merwe is a layer-by-layer 2D growth mode. Volmer-Weber is a 3D island growth where the interactions of the adatoms are higher than the interaction with the substrate. The Stranski-Krastanov growth mode is a 3D growth mode caused by a high lattice mismatch.

The Frank-van der Merwe mode occurs when the adatoms have a stronger interaction with the substrate than with each other. The atoms tend to form a complete monolayer above the substrate before starting the second layer. This growth mode generally produces smooth and coherent films. The Frank-van der Merwe growth can also be called a layer-by-layer growth.

The second growth method is the Volmer-Weber mode. This mode occurs when the interactions between the adatoms are higher than the interactions with the substrate. It is the opposite of the Frank-van der Merwe growth mode. The adatoms tend to cluster together and form larger islands. The area between the islands is uncovered during the first growth stage. After some time, the islands grow in size and merge together.

The last growth mode is the Stranski-Krastanov mode. This mode occurs when there is a high lattice mismatch between the substrate and the epitaxial layer. The adatoms arrange themselves in a strained monolayer. To release the strain, the adatoms form an island above the critical thickness. These islands have a higher lattice constant than the substrate.[25]

2.7 Stacking faults

A further disadvantage of the c-GaN is that the zincblende structure is only the metastable phase. This can result in further defects since the atoms prefer the formation of the hexagonal phase. Therefore, it will result in the formation of inclusions of the hexagonal phase in the cubic crystal. However, this aspect is very dependent on the growth condition.

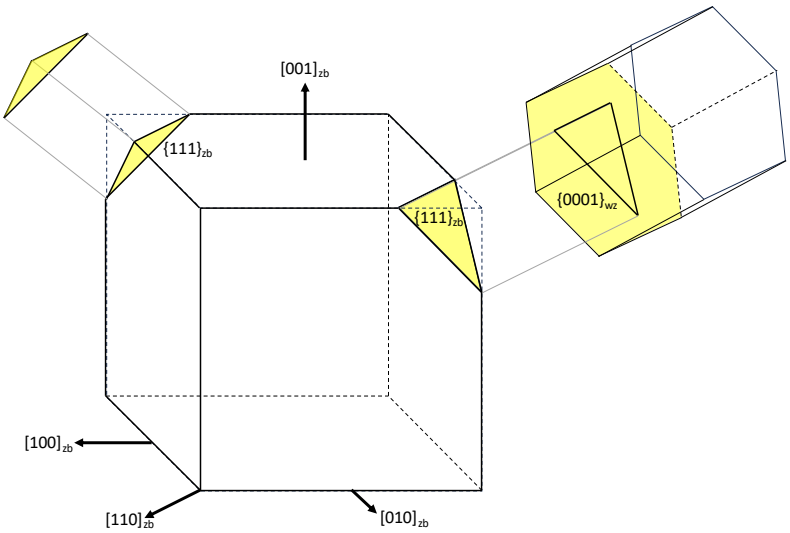

Figure 7: Illustration of the crystallographic arrangement of the {111}zb plane to the {0001} plane of the wutzite phase. Adapted from [28]

A stacking fault is a type of defect in the crystal structure. It results from the structural resemblance of the hcp and fcc crystal structure. The (0001) plane of the hcp structure is similar to the (111) plane of the fcc structure. If we only look at a single monolayer of these structures, they are identical. However, they differ in the stacking order. The hcp structure only consists of two different orientations of these monolayers, which alternate one by one. This stacking order is visualized in Figure 8. The two types of orientations are labeled as A and B. Therefore, the stacking order of the hcp structure is called ABAB.[29]

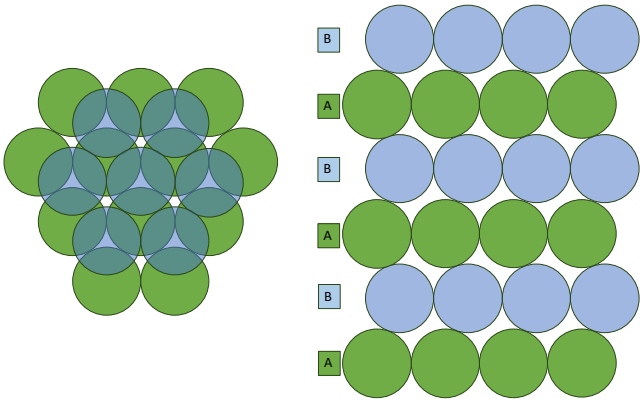

Figure 8: Visualization of the stacking order of the hcp structure in [0001] direction.

On the other hand, the fcc structure contains all three possible orientations of the monolayers. The stacking order is visualized in Figure 9. The orientations are rotated in the ABCABC order.

A stacking fault is a crystal defect that breaks the crystal's original stacking order. For example, a hexagonal inclusion in a cubic crystal would disrupt the ABCABC order. An example of this would be the following stacking order ABCABABC. They can occur during the growth process when the growth happens on one of the two mentioned crystal layers. They mainly occur during the growth of the metastable phase. Because if the atoms can nucleate on a freestanding (111) facet, they can tend to nucleate in the more stable hexagonal structure. Therefore, this is primarily a problem for the growth of cubic gallium nitride. The stacking faults can affect the electrical and optical properties of the crystal negatively.

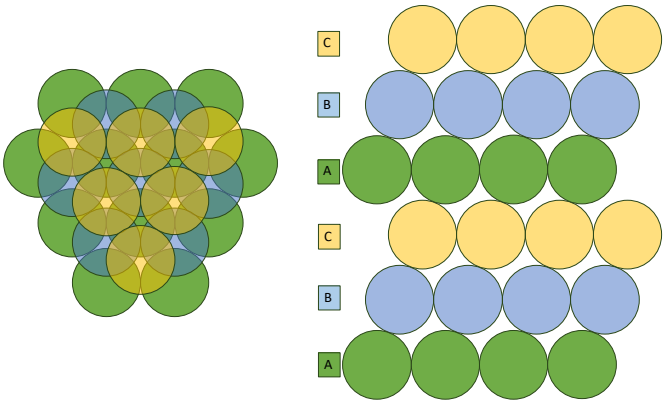

Figure 9: Visualization of the stacking order of the fcc structure in [111] direction.

2.8 Remote epitaxy

Remote epitaxy is a relatively new area of research, showing significant promise in addressing challenges tied to lattice mismatches in heteroepitaxy[6]. At its core, this method integrates a 2D material as an interlayer positioned between the substrate and the epitaxial layer. The primary objective is to leverage the 2D-material interlayer as a buffer, which acts to prevent the formation of covalent bonds between the substrate and the epitaxial layer. Figure 10 shows an example of a remote epitaxy structure. A graphene monolayer is placed on a 3C-SiC substrate. The graphene-covered substrate is then used to grow c-GaN on top. The sketch is true to scale.

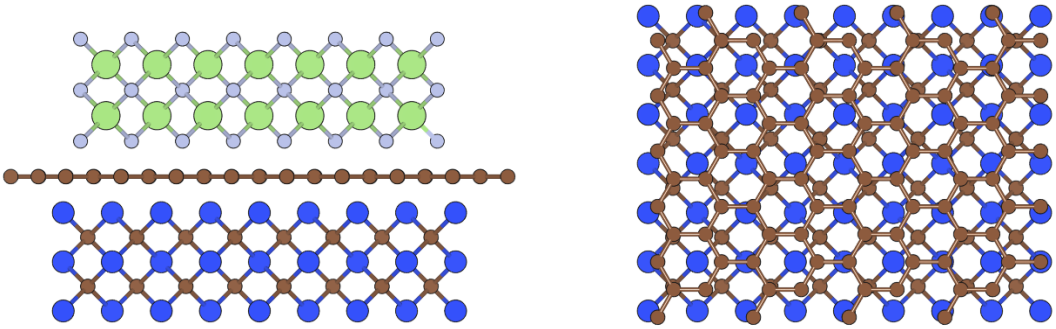

Figure 10: VESTA[14] sketch of the crystal structure of a graphene-covered 3C-SiC layer. (left) Sketch of a side view of a c-GaN layer above a graphene-covered 3C-SiC substrate. (right) Top view of a graphene-covered 3C-SiC substrate. Si atoms are blue, carbon atoms are brown, nitrogen atoms are grey, and gallium atoms are green.

Under optimal conditions, the adatoms will naturally orient themselves in alignment with the dangling bonds of the underlying substrate. This still allows the formation of the same crystal structure on top of the substrate but will reduce strain formation in the epitaxial layer. Consequently, this process minimizes the formation of dislocations, enhancing the overall crystal quality.

The benefits of this growth technique are manifold:

The first benefit is the versatility of substrate Choice. Remote epitaxy broadens the horizon for substrate material options. Traditionally, certain substrate materials were deemed incompatible with heteroepitaxy due to pronounced lattice mismatches. This technique potentially allows for the incorporation of more cost-effective substrate materials, thereby driving down the overall expenses tied to the growth process.

Secondly, it allows for layer transferability. A notable feature of this method is the theoretical ease with which one can detach the epitaxial layer. Due to the absence of covalent bonds, this layer can be effortlessly lifted and transferred to a different substrate. This feature is invaluable for niche applications where the original substrate's absorption properties might be less than ideal. Furthermore, it allows reuse of the substrate. If an expansive substrate is necessary, repetitive usage becomes a viable option, further presenting cost-saving opportunities.[30]

So far, the remote epitaxy has been successfully performed for different material systems. The work of J. Kim et al.[5] was able to grow h-GaN epitaxially on graphene-covered SiC substrates. Using epitaxial graphene grown on SiC as both a template for h-GaN growth and a release layer for its transfer, they managed to produce high-quality h-GaN films. These films boasted a low defect density and surface roughness comparable to those cultivated on traditional substrates like SiC or sapphire. Interestingly, the team was able to reuse the graphene/SiC substrate for multiple GaN growth and transfer cycles without necessitating any surface treatments. Furthermore, by growing InGaN/GaN heterostructures on these recycled graphene/SiC substrates, they successfully crafted fully operational blue LEDs, which were then transferred onto flexible tapes. The layers were grown with a MOCVD.

To achieve perfect remote epitaxy conditions, the graphene must fulfill two requirements[31,32]. First, the graphene has to only consist of one monolayer. By increasing the graphene layer count, the substrate-to-layer interactions decreases rapidly[33]. The work of Y. Kim et al.[10] determined the maximum graphene layer count for remote epitaxy to be two layers. With three layers or more, the adatoms will no longer feel the transmission of crystallographic information. This effect depends on the used materials system. However, it can be concluded that the optimal conditions are only achievable using single-layer graphene.

Using three or more graphene layers changes the growth mechanism from remote epitaxy to Van-der-Waals epitaxy. In this case, the nucleation of the adatoms will only happen due to the van-der-Waals forces. With no interaction between the substrate and the adatoms, the nucleation will occur in random orientations that do not align with the substrate material. A schematic of this is shown in Figure 11. While the Van-der-Waals epitaxy process does not fulfill the requirements for bulk material growth it is used to grow 2D materials[34].

The second requirement for remote epitaxy is a low number of defects in the graphene monolayer. Small holes throughout the layer can cause a growth mechanism called pin-hole epitaxy. In this case, the first nucleation will only be limited to these holes since the adatoms can form covalent bonds directly with the substrate. Therefore, the nucleation probability is significantly enhanced compared to the remote epitaxy nucleation. Consequently, the following adatoms will bond to the nucleation centers in the defect holes and laterally overgrow the graphene layer. A schematic of this is also shown in Figure 11. While this process is not perfect remote epitaxy, it still has comparable characteristics. The epilayer will show a crystallographic alignment with the substrate and it will also reduce the influence of the lattice mismatch. However, the layer can be locally strained at the nucleation centers. The main drawback of Pin-hole epitaxy is that the exfoliation of the epilayer can be impossible depending on the size and number of holes in the graphene layer. The work of D. Jang et al.[35] shows that it can be possible to perform an exfoliation. This, however, requires the number and size of the holes in the graphene layer to be minimal.

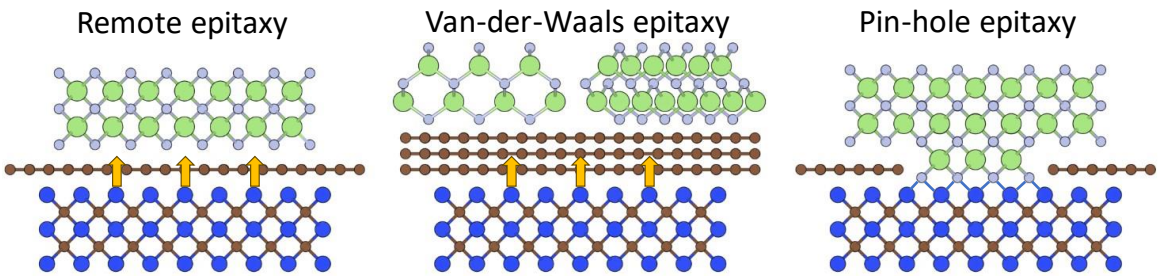

Figure 11: Schematic of the three different growth mechanisms for GaN on a graphene-covered 3C-SiC substrate. Si atoms are blue, carbon atoms are brown, nitrogen atoms are grey, and gallium atoms are green.

2.9 Graphene

Graphene is the most interesting 2D material. With its unique characteristics, it is expected to have many use cases in the future. Graphene consists of atomically thin layers of carbon atoms. The atoms are arranged in hexagonal orientations.[36]

Carbon is a part of the fourth group in the periodic table. This means it has four valence electrons. In graphene, each carbon atom will form three sigma bonds with the three nearest carbon atoms. The one remaining electron will form a pi bond. This bonding scheme requires the three 2p orbitals and the 2s orbitals of carbon. These orbitals mix to form three equivalent sp2 hybrid orbitals.

Compared to the diamond structure, the bond will no longer form a tetrahedron. Instead, the bonds will all lie in the same plane, creating a flat structure. The angle between the bonds is 120°, resulting in the lattice's hexagonal arrangement. The lattice structure of a graphene monolayer is shown in Figure 12.

The fourth valence electron of each carbon is in a hybridized 2p orbital. These electrons are delocalized over the entire graphene layer. This delocalization is responsible for the many unique properties of graphene such as high electron mobility.[37]

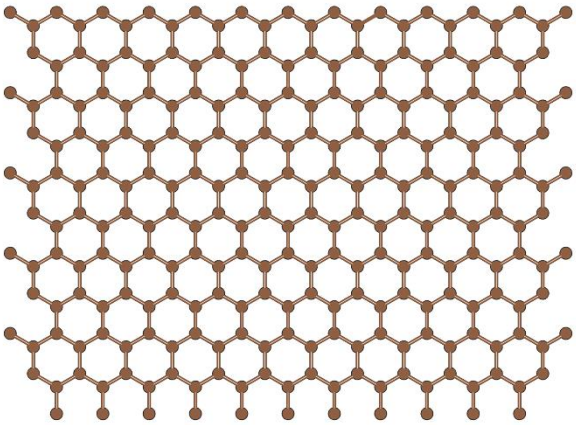

Figure 12: Visualization of the atomic structure of graphene created with VESTA[14]

The most common form of carbon is graphite, which consists of stacked graphene layers. This is the stable form since diamonds will only be formed by applying high amounts of pressure. Due to this similarity between graphite and graphene, the first method to create graphene was to extract a thin layer of graphite with a scotch tape. This method, however, is limited to only small micrometer-sized flakes of graphene and is therefore not suitable for epitaxial applications.

Today, there are two more methods to create graphene. The first method is chemical vapor deposition (CVD)[38,39]. This method has the benefit that the graphene can be transferred onto every desirable substrate material. The second method is the thermal decomposition of silicon carbide. This has been successfully used in the work of Kim et al.[5] The benefit of this method is the high quality of the graphene. Due to the underlying single crystalline characteristic of the SiC the graphene will contain significantly fewer defects than the CVD method[40].

3. Experimental setup

In this chapter the fundamental principle and set-up of the molecular beam epitaxy will be explained. Firstly, the used plasma-assisted MBE system will be described. Then, the reflection high-energy electron diffraction method for the in-situ growth observation will be explained.

3.1 Plasma-assisted molecular beam epitaxy

The epitaxy of the gallium nitride layers was performed with a plasma-assisted molecular beam epitaxy. The used MBE system is a Riber32 MBE. It has a horizontal layout. Nitrogen is generated by an Oxford HD25 plasma source. The system contains effusion cells for gallium, aluminum, indium, silicon, and germanium. This allows the growth of all three nitride semiconductors: gallium nitride GaN, aluminum nitride AlN, and indium nitride InN. The silicon and germanium sources are used for n-type doping.

The substrate holder contains a heater that can reach temperatures of 1000°C and be rotated continuously during the growth. A thermocouple measures the temperature. The vacuum is generated by a turbo-molecular pump (TMP). The system pressure can reach 10^{-9} mbar. During the growth, the chamber walls can be cooled by a liquid nitrogen cryo shield. The system vacuum is monitored by a quadrupole mass spectrometer (QMS).

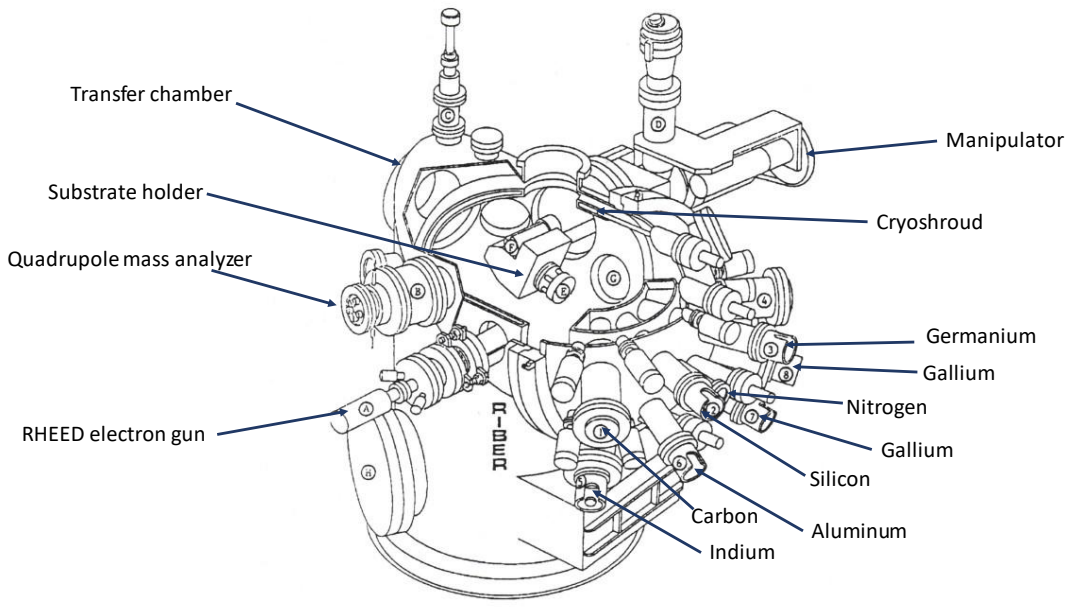

Figure 13: Schematic sketch of the used RIBER32 MBE setup.

Furthermore, the system contains a RHEED system to monitor the growth in situ. The RHEED cannon can accelerate the electron with an acceleration voltage of 16 kV. The electrons hit a fluorescence screen after they are diffracted by the sample. The RHEED pattern will be recorded by a camera and analyzed by computer software to compare the intensity of the different reflections.

3.2 Reflection high-energy electron diffraction

Reflection high-energy electron diffraction (RHEED) is an in-situ technique to analyze the crystal structure of the surface layer during the growth in an MBE. The RHEED system generates a diffraction pattern by accelerating electrons onto the sample surface at a shallow angle. The diffracted electron will then fly to the fluorescence screen on the opposite side, creating the diffraction pattern. The electrons are being accelerated under a high voltage of about 15 kV. The shallow angle is vital to ensure that only the surface layers are measured. A sketch of the setup is shown in Figure 14.

Central to understanding the diffraction patterns of a RHEED measurement is the concept of Ewald's sphere. The sphere is a geometric construction of the electron wave vector in reciprocal space. In this case, the electrons will only interact with the surface atoms. Due to the limited expansion in one direction, the surface atoms are considered two-dimensional. In the reciprocal space, the surface is represented by rods. The intersections of the rods and the Ewald's sphere form the diffractions spots on the screen.

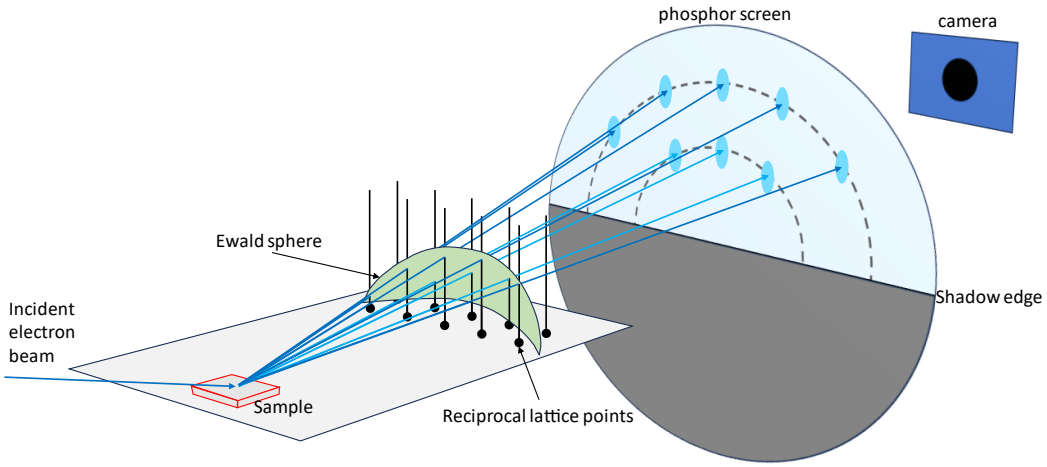

Figure 14: Schematic diagram of RHEED apparatus, including a sketch of the Ewald sphere and the intersection of the truncation rods with the sphere. Adapted from [25]

The diffraction pattern is being recorded by a camera and analyzed by a computer program. This allows for a precise measurement of the intensity change over time. The intensity of the reflection depends on many factors. One of these is the fact that the intensity is dependent on the surface roughness. A higher surface roughness will lead to enhanced scattering phenomena consequently, reducing the number of electrons

reaching the fluorescence screen. This allows, therefore, quantitative assessment of the alternations in the surface roughness during the growth process. It also allows for a precise measurement of the growth rate in specific cases. This accuracy is achieved when observing the changes in surface roughness that occur with each successive monolayer during growth. However, such precise measurements are only possible when the growth occurs one monolayer at a time.

Depending on the surface structure, the RHEED will create different kinds of patterns. The most common kinds of patterns are visualized in Figure 15. The pattern will provide information over different morphologies like the difference between a perfect monocrystalline surface and a crystal consisting of different anti-phase domains (Figure 15 a),b)). Since this work used a 3C-SiC/Si (001) substrate, containing anti-phase domains the second pattern is the most important one for this work. Especially during the beginning of the growth process, it often results in the formation of 3D-island, creating the spot pattern shown in Figure 15 f).

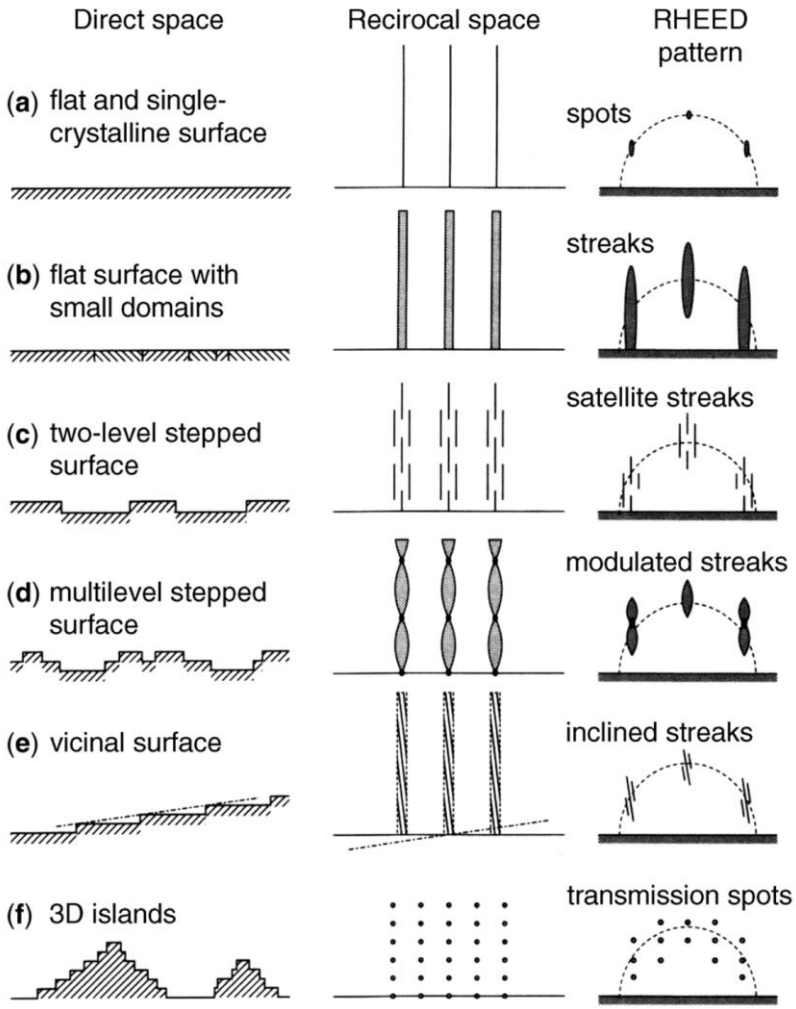

Figure 15: Schematics of various kinds of realistic surfaces in real-space morphology, in reciprocal space, and their RHEED patterns. Taken from [41]

4. Characterization methods

This chapter presents the devices used to analyze the graphene layers and the grown GaN films. The first one is Raman spectroscopy, which has been used to ensure the usage of monolayer graphene. This measurement was done by Elias Kluth of the group of Prof. Rüdiger Goldhahn from the Otto von Guericke University Magdeburg. For the understanding of the crystal quality and phase composition of the GaN layers, high-resolution x-ray diffraction (HRXRD) is used. The surface roughness and state will be observed by atomic force microscopy (AFM) and scanning electron microscopy (SEM).

Furthermore, photoluminescence spectroscopy (PL) was used to gain information about the phase purity, stacking faults, and impurities. Lastly, electron backscatter diffraction (EBSD) was used to analyze the phase composition on a microscopic level. This measurement was performed by Olga Augst of the group of Prof. Jürgen Christen from Otto von Guericke University Magdeburg.

4.1 Raman spectroscopy

Raman spectroscopy is an optical measurement technique used to analyze the vibrational modes of molecules. Besides analyzing molecules, it can also be used to investigate the phonons in a crystal. The technique relies on Raman scattering between a light photon and a molecule or crystal. When a photon interacts with a particle, a scattering can occur. Most interactions are elastic scattering processes that do not change the photon energy. This is called the Rayleigh scattering. The probability of scattering increases with a decreasing wavelength. This results in a higher probability of scattering blue photons than red photons. However, it is also possible that an inelastic scattering happens. This is called the Raman scattering and is the foundation of the Raman spectroscopy.

The scattering process is visualized in Figure 16 to understand these scattering processes better. The incoming green photon with a frequency of ν_0 scatters with a molecule. During the scattering, the molecule absorbs the photon, and the molecule's energy state shifts to a higher virtual state. The molecule has the desire to fall back into a vibrational state. If it falls back into the same state as before the scattering, the molecule will emit a photon with the same frequency as the absorbed photon. The elastic Rayleigh scattering has the highest probability of occurring. However, there is a probability that the molecule falls into a different vibrational state. When the molecule has a higher vibrational state after the scattering, it will have absorbed a part of the photon's energy. Therefore, the emission photon will have a smaller energy and a larger wavelength. This change is called Stokes shift and is one kind of Raman scattering. The change in the energy will be equivalent to the difference between the two vibrational states of the molecule. This difference is a characteristic value depending on the type of molecule. Different elements and bonds between the atoms will result in different vibrational states. If the molecule already has an excited vibrational state before the scattering, the emission photon may have a higher energy than the absorbed photon. This energy shift is called the anti-Stokes shift. The change in the energy is also equivalent to the difference between the two states of the molecule.

Besides the scattering between a photon and a molecule, the Raman scattering can also be observed for interactions with a crystal. In this case, a phonon is either created for a Stokes shift or absorbed for an anti-stokes shift.

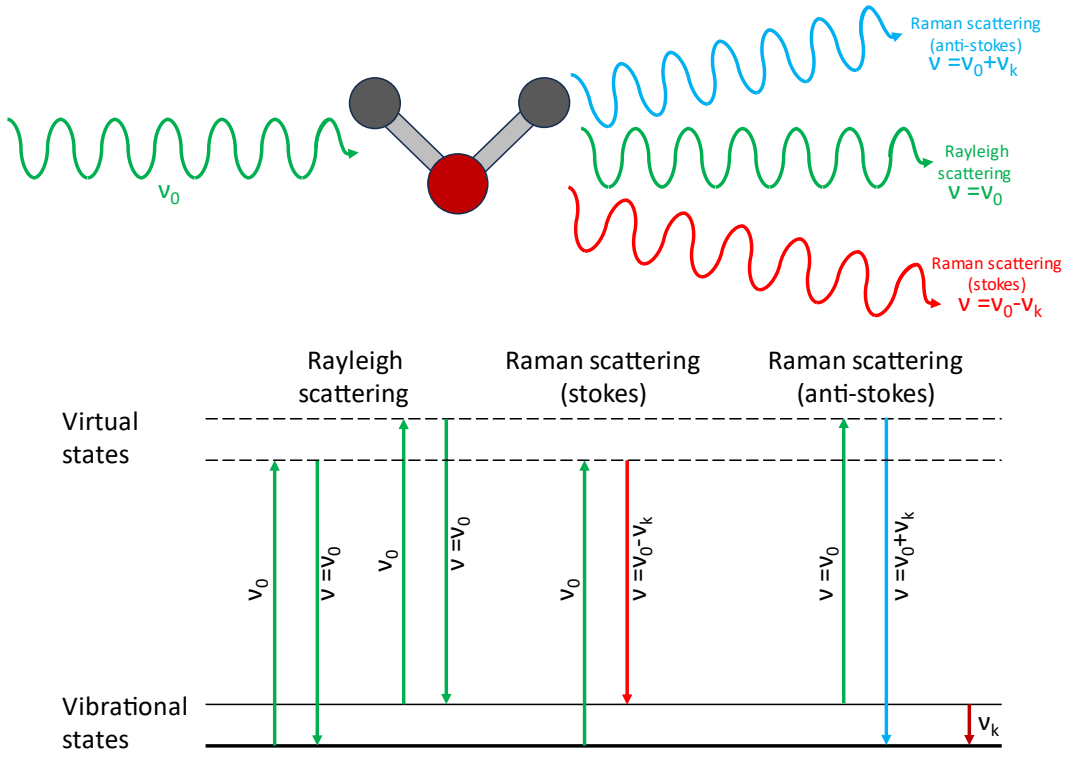

Figure 16: Schematic diagram of Rayleigh and Raman scattering processes. This figure illustrates the interaction of incident light (frequency ν_0) with a molecule, resulting in Rayleigh scattering ($\nu = \nu_0$) and Raman scattering (Stokes shift: $\nu = \nu_0 - \nu_k$, Anti-Stokes shift: $\nu = \nu_0 + \nu_k$). The transitions between vibrational states are also depicted.

The distinct change in photon energy caused by the Raman scattering can be used to perform Raman spectroscopy and gain information about the different energy states and, therefore, chemical and structural information about a sample. For this, a laser is directed onto a sample, and the scattered light is being measured. It is important to use a monochromatic light source to distinguish between the Rayleigh scattered photons and the Raman scattered photons. The difficult part is that Raman scattering is very weak compared to the much more intense Rayleigh scattered laser light. Approximately only $1/10^7$ of the scattered light is caused by Raman scattering.

Regarding the remote epitaxy process, Raman spectroscopy can be applied to distinguish between monolayer graphene and multilayer graphene. As discussed previously, the remote epitaxy process needs to use monolayer graphene. This is essential to ensure the strongest interactions of the dangling bonds through the graphene. Monolayer graphene has two unique characteristics in the Raman spectrum. Figure 17 compares two Raman

spectra of monolayer graphene and graphite. The first peak at wavenumber 1580 cm^{-1} corresponds to the G band. This peak originates from in-plane vibrations of the sp^2 carbon atoms[42]. The intensity is supposed to increase with the amount of graphene layers. While this peak provides a difference for monolayer graphene, it is complicated to use the peak information to determine a monolayer characteristic accurately. The second peak at a wavenumber of 2670 cm^{-1} can only be observed for monolayer graphene. According to Ferrari et al.[43], this peak will change into a band of multiple smaller peaks caused by two phonon resonance processes. This change is caused by the splitting of the electronic bands, which occurs in multilayer graphene. In summary, a single sharp and symmetric peak in the Raman spectrum at 2670 cm^{-1} is a clear indication of monolayer graphene.

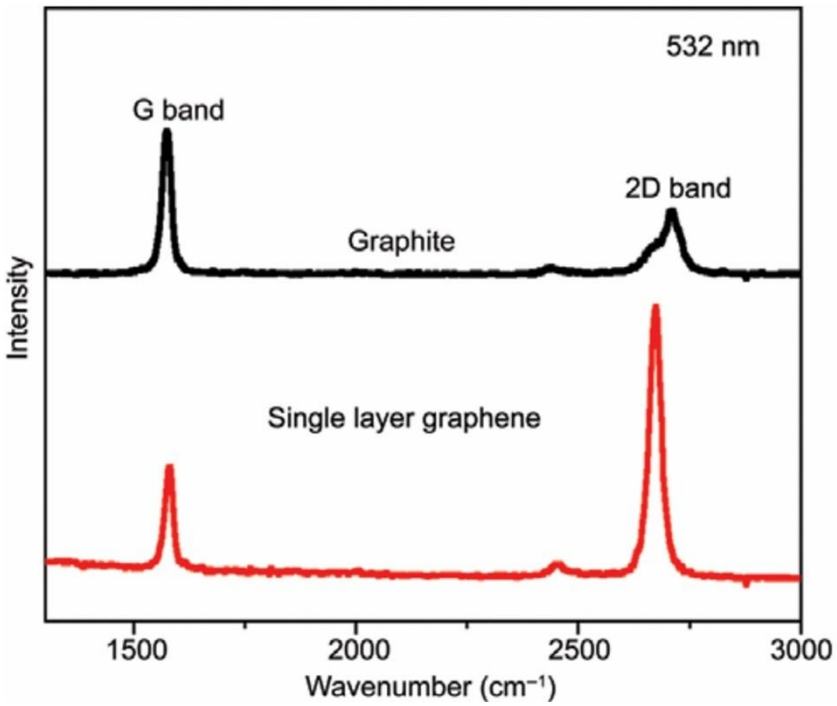

Figure 17: Raman spectra of single-layer graphene compared to graphite. Taken from [42]

4.2 High-resolution x-ray diffraction

The high-resolution X-ray diffraction (HRXRD) characterization method is a destruction-free measurement method to analyze crystal quality. Comparable to the RHEED, this measurement is based on the diffraction with the periodic arranged atoms. In contrast, this method uses X-ray photons to analyze the whole crystal instead of the surface.

The fundamental principle this method uses is Bragg's law. It describes the fundamental interaction between an electromagnetic wave and a periodic lattice of atoms. The wave will be scattered by the atoms, and depending on the angle, it will result in constructive interference. Figure 18 illustrates the scattering of a wave at two atomic layers. Notably, the wave interacting with the bottom layer will travel a longer way. Constructive interference occurs when the path length difference matches a multiple of the wavelength. The subsequent equation outlines this relationship: the separation between atomic layers is represented by 'd', the wavelength is indicated by 'λ', 'n' is a natural number, and 'θ' symbolizes the angle between the incident wave and the crystal lattice.[44]

$$n\lambda = 2d\ sin\ \theta$$

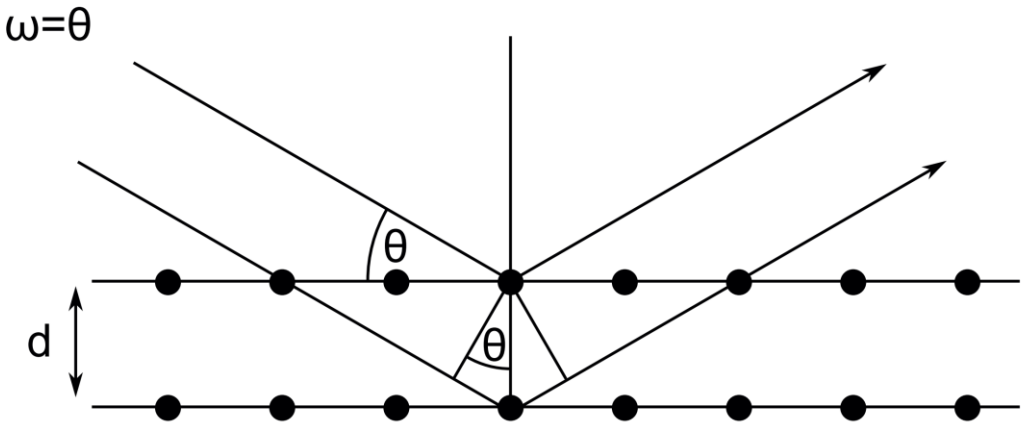

Figure 18: Visualization of Bragg's law. Taken from [13]

HRXRD measurements utilize this law to characterize crystal quality. Figure 19 visualizes a simplified setup of an HRXRD system. The wavelength must be of a similar order of magnitude to match the lattice constant. Consequently, only X-ray is suitable. A HRXRD

system consists of an X-ray tube with a line focus. A monochromator is used to filter out the Kα line of the used material in the X-ray tube. This results in a monochromatic and parallel wave directed at the sample. Subsequently, a detector measures the diffracted radiation. The angle between the sample and the X-ray source is denoted as ω, while the angle between the sample and the detector is referred to as 2θ.

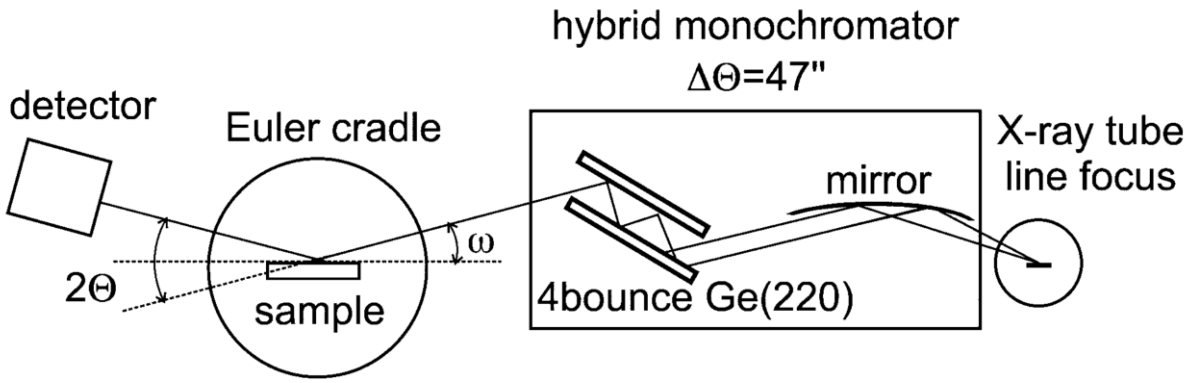

Figure 19: Schematic setup of the HRXRD device. Taken from [45]

Rocking curve

An HRXRD machine offers a variety of measurement techniques. Among these, the rocking curve measurement stands out as being the most common. In this procedure, the incident ω-angle is systematically varied around a specific plane reflection. The curve's intensity and full width at half maximum (FWHM) is a measurement of the uniformity of the lattice plane alignment perpendicular to the sample surface. The FWHM gives insights into the homogeneity of the crystal. A broader FWHM value implies a more irregular or uneven crystal structure, which can be caused by defects, strain gradients, dislocations, mosaic spread, or misaligned crystallites.[46]

The practical application of the measurement is manifold. It plays a crucial role in assessing the crystal quality of epitaxial layers. It can be used to compare different growth processes with each other easily. However, a comparison is only possible when the essential characteristics of the epitaxial layer, like thickness and composition, are identical.

Reciprocal space maps

Another essential measurement method is the reciprocal space map (RSM). Contrary to the one-dimensional rocking curve, this measurement scans a two-dimensional area around a singular reflection point in the reciprocal space. In this case, the 2θ-angle is

additionally varied throughout the measurement. This method is especially useful in heteroepitaxial systems, where the different lattice constants of the different materials result in different positions in the reciprocal space. The relative position between these spots can provide different information[46]. The following equations are used to calculate the coordinates in the reciprocal space from the ω and 2θ-angle.

$$q_{\parallel} = R(cos\ \omega - cos(2\theta - \omega))$$

$$q_{\perp} = R(\sin\omega + sin(2\theta - \omega))$$

The reflection of a 3D crystal translates to a 0D dot in the reciprocal space. Using the Ewald construction, one can specify the area of the reciprocal space that can be captured by measuring Bragg reflections, see Figure 20. All the reciprocal lattice points drawn in black can be captured with the diffractometer. The radius of the half circles depends on the wavelength of the used X-ray source. The points outside the larger radius can be measured using a shorter wavelength.

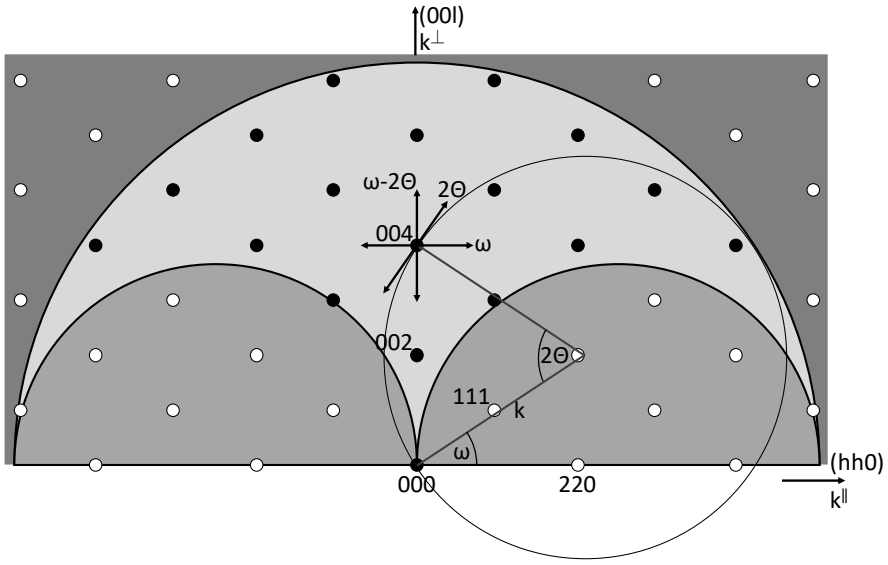

Figure 20: Measurement area in the reciprocal space. The Ewald construction of the symmetrical (004) reflection of a (001) surface material in the zincblende structure is highlighted. Adapted from [46].

Figure 20 shows the Ewald construction of cubic material with a (001) surface. The ω and 2θ-angle are marked along the wavevectors k. The arrows around the (004) reflection mark the different scan directions according to the labeled angles.

In the case of heteroepitaxial sample, the reciprocal space contains a superposition of the reciprocal spaces of each layer. One has to distinguish between layers that are pseudo morphically strained and fully relaxed. A pseudo morphically strained layer has the same lattice constant parallel to the surface. This can be seen in the reciprocal space when the two points of different layers are positioned at the same x coordinate, see Figure 21 a). When the layer is fully relaxed, the reflection points are moved according to their lattice constant, see Figure 21 b).

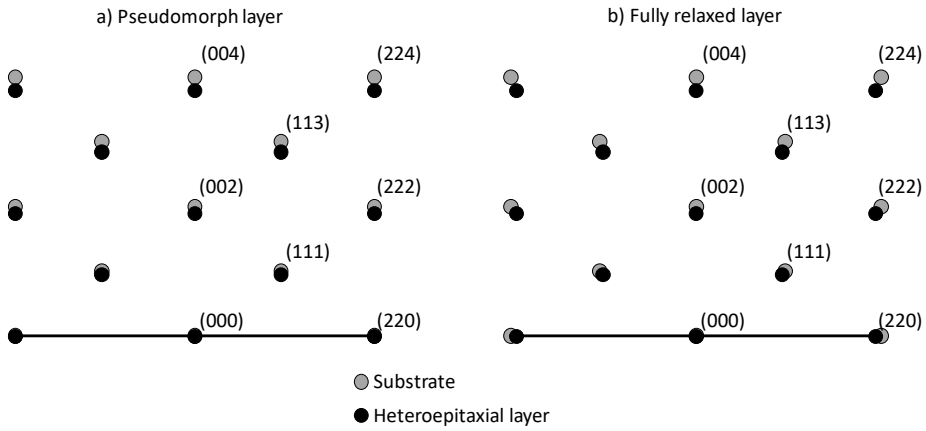

Figure 21: Reflections of a heteroepitaxial layer in the reciprocal space for a) a pseudomorph layer and b) a fully relaxed layer. Adapted from [46]

There are two kinds of RSMs. The first is the asymmetrical RSM, which measures a reflection point not positioned in the middle of the reciprocal space. In this case, the ω and θ angles are not identical. By looking at Figure 21, one can see that these reflections are highly dependent on the strain in the layer. Therefore, these measurements can be used to calculate the strain in the epitaxial layer. This is especially interesting for materials with a small lattice mismatch, where a pseudomorphically strained layer is possible.

For this work, the measurement of a symmetrical map is especially interesting. A symmetrical map is taken around a symmetrical reflection in the middle of the reciprocal space, such as (002). In this case, the ω and θ angles are the same. In the case of cubic GaN, the (002) RSM contains information about the hexagonal inclusions. Figure 22 shows an example of a symmetrical RSM of a cubic GaN with a high amount of hexagonal inclusions[28]. The stacking fault described in Chapter 2.7 can be seen as lines in the reciprocal space (marked with SF). When the stacking faults result in the formation of a multilayer hexagonal phase, two new reflections can be measured close to the position of

the (002) reflection. These new reflections can be attributed to the (10-11) and (-1011) planes in the wurtzite crystal. The comparison of the integral intensity of these reflections allows to quantify the hexagonal inclusions in the cubic layer. The other labeled features are the detector streak (DS), the crystal truncation rod (CTR), and the Bragg ring (BR). The CTR is a feature caused by the crystal surface, and polycrystalline SiC inclusions cause the BR.

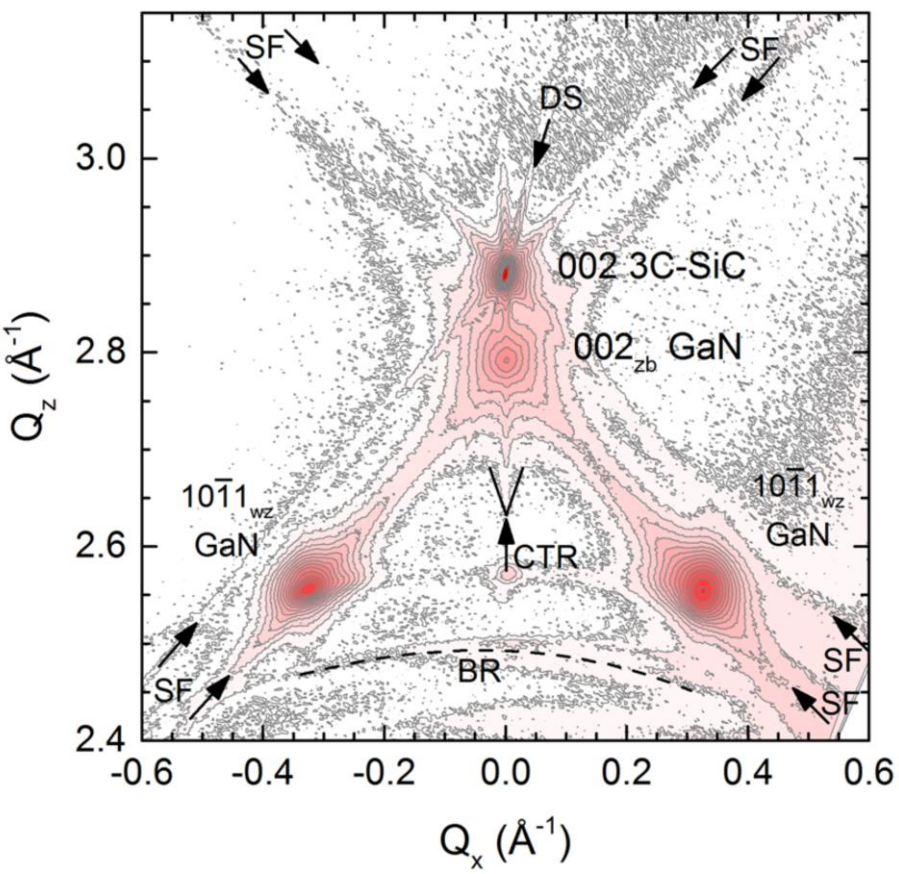

Figure 22: Symmetrical RSM of the cubic (002) reflection of GaN grown under non-optimized conditions. The measured sample has a high amount of hexagonal inclusions. Taken from[28].

4.3 Atomic force microscopy

Atomic force microscopy (AFM) is suitable for investigating surface height profiles. The principle of operation is shown in a simplified form in Figure 23. A cantilever is moved over the surface by piezoelectric elements. Ideally, the tip of the cantilever consists of just one atom. In the used contact mode, the tip is in direct contact with the surface and bends the cantilever accordingly when there is a change in height. At the same time, a laser is directed onto the back of the cantilever. The reflection of the laser beam then hits a

photodetector. The bending of the cantilever can be determined by analyzing the position of the laser beam on the photodetector. By scanning the surface, it is thus possible to create a detailed height profile of it.

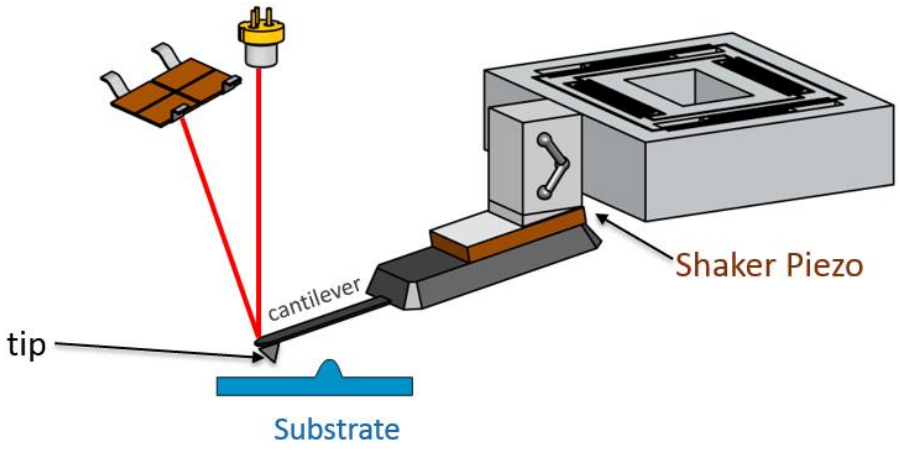

Figure 23: Schematic illustration of the AFM setup. Taken from [47]

In this work, a Nanosurf Mobile S atomic force microscope is used. The measurements were all performed in contact mode. The used cantilevers are the ppp-xycontr cantilevers from NanoAndMore GmbH. The device was used to measure areas of up to 10 x 10 µm².

4.4 Scanning electron microscopy

For the observation of larger areas of the surface, a scanning electron microscopy (SEM) was used. Due to the shorter wavelength of electrons in comparison to light photons, electron microscopy can be used to take pictures with a higher resolution.

The standard setup of a SEM is shown in Figure 24 a). The whole setup is located inside a vacuum chamber to prevent the electrons from colliding with air molecules. The electron gun produces the electron beam and is located at the top of the microscope. A tungsten filament is heated to emit electrons. By applying a voltage between the filament and the Anode, the electrons are accelerated to the desired energy. The accelerated electrons will pass through the magnetic field of the underlying magnetic lenses that are used to focus the electron beam onto the sample surface. The position of the electron beam on the sample surface can be adjusted by the scanning coils. To create images of the surface, the beam is moved in a raster pattern across the sample surface. The scanning speed and resolution are adjustable and depend on the desired image quality and magnification.

When the electron beam hits the sample surface, different interactions can take place. Some electrons will be scattered backward after the interaction with the target sample. They take roughly the same path and can be detected by a detector near the incoming beam. The second type of electrons are the secondary electrons. These are electrons that belonged to the atoms in the sample but were excited by the electron beam. The secondary electrons do not move in the same directions as the backscattered electrons. They can be detected by an additional detector that is located further away from the electron beam optics. An electrostatic field helps to attract the secondary electrons.

Both the generation of the backscattered and the secondary electrons depends on the surface features. By scanning the electron beam over a specific area on the sample surface, the detected intensity can be used to create an image of the surface.

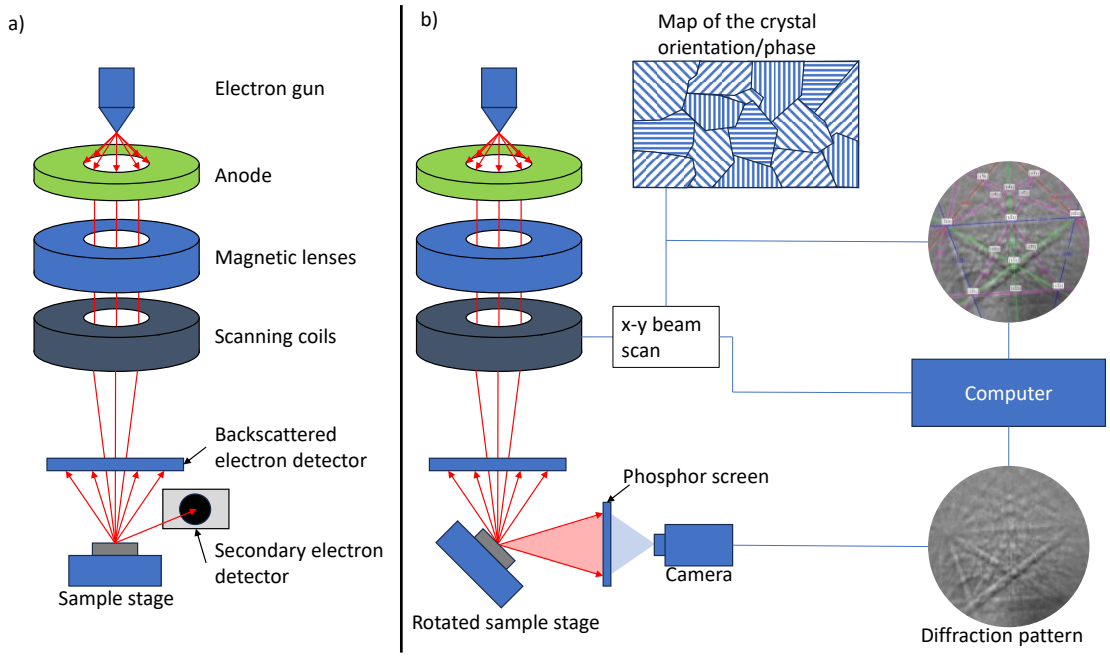

Figure 24: Schematic illustration of the standard setup of an SEM (left) and an SEM used for EBSD measurements (right)

4.5 Electron backscatter diffraction

While a standard SEM provides information about the surface structure of a sample, the addition of a rotatable sample stage and a phosphor screen allows to perform electron backscatter diffraction (EBSD) measurements. Figure 24 b) shows the changes to the setup. EBSD is a powerful technique to analyze the crystallographic orientation and phase of crystalline materials. Like X-ray diffraction, the EBSD technique uses the diffraction process to identify the crystal orientation and phase. However, the use of an electron

beam as the source of radiation allows for a high spatial resolution. The HRXRD on the other hand is used for large areas and characterization of the bulk sample.

The diffraction pattern is created by the interaction between the electron beam and the crystal lattice of the sample. When the electrons hit the material, some electrons are scattered by the atoms. These electrons form a cone that emerges from the material's surface and hits the phosphor screen. The screen shows a pattern consisting of bright and dark lines, which correspond to the different crystal planes that satisfy the Bragg condition. These lines are called Kikuchi lines.

The resulting diffraction pattern is unique to each crystal structure and rotation. A database containing the known crystal structures and orientations is used to compare the pattern and identify the characteristics of the sample. In combination with the microscope's scanning mode, a complete map of the crystal orientations and phases can be created of a small sample surface area. In this work, the EBSD technique is used to differentiate between the wurtzite and zincblende structure of GaN.[48–50] Figure 25 shows an example of two EBSD patterns. The first pattern corresponds to a cubic GaN layer. To the right is an overlay highlighting the Kikuchi lines identified by a computer program. The second diffraction pattern serves as an example of hexagonal GaN.

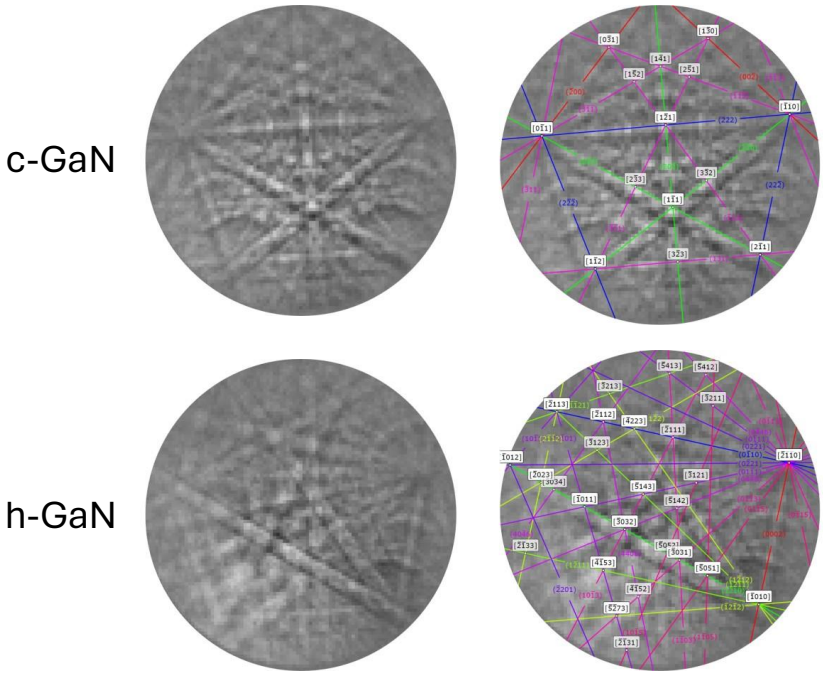

Figure 25: Comparison of an EBSD pattern for c-Gan and h-GaN. The left side shows the measured pattern. On the right side is an overlay highlighting the Kikuchi lines identified by a computer program.

4.6 Photoluminescence

Photoluminescence is a destruction-free characterization method for semiconductor crystals. This measurement is based on the emission of light from a material after it has absorbed photons. Information about the semiconductor's properties can be gathered by observing and analyzing the emitting light.[51]

At its core, photoluminescence is based on the interactions between semiconductor material and light. When a photon with a higher energy than the material's bandgap hits the semiconductor, an electron from the valance band is excited to the conduction band. The electron leaves a hole behind in the valence band. The combination of both is called an electron-hole pair. As time progresses, the electron and hole will move through thermalization to the lowest point in the conduction band and the highest point in the valence band. When the electron-hole pair is located at the same position, they will recombine over time. During this recombination, a new photon is emitted. The energy of this photon will be below the band gap energy. Figure 26 visualizes the process from the absorption to the recombination. The exact energy depends on the excitonic binding energy, and the existence of localized energy states induced by defects or impurities.

Besides the possibility of measuring the band gap of a semiconductor material, the photoluminescence method can gain information about the overall quality of the crystal. A high-quality crystal will usually emit a single pronounced PL peak. Materials with defects and dislocations will typically emit more and weaker peaks.[52]

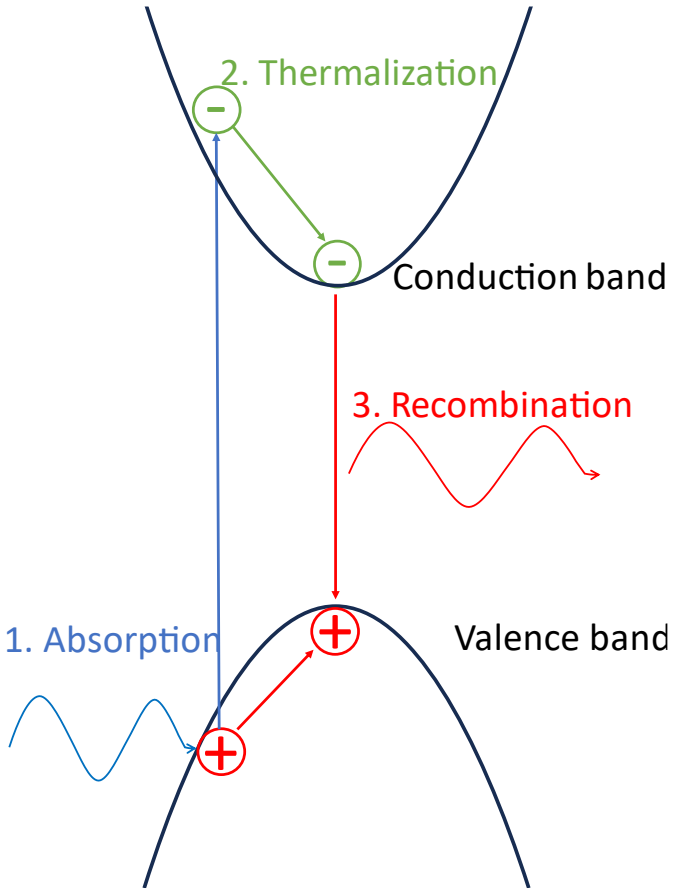

Figure 26: Illustration of the fundamental process of photoluminescence. A photon is absorbed by an electron, which is excited into the conduction band. The generated electron-hole pair will move to the band edges. Afterwards, the pair will recombine, and a photon with a longer wavelength will be emitted.

Unintentional impurities and defects in the crystal lattice will introduce mid-gap states. The states can be seen in the spectrum as additional peaks. Figure 27 contains different possible recombination processes containing these mid-gap states. The first recombination (e,h) is the standard recombination between an electron in the conduction band and a hole in the valence band. In general, however, an electron-hole pair will exist in a bound state. Due to the Coulomb force, they will be attracted to each other and form the quasiparticle an exciton. Their energy will be less than the band gap energy in case of a recombination.

The excitons in a semiconductor can be divided into two types. The first one is the free exciton (FX). A free exciton has a low binding energy, which means the electron and hole are weakly bound to each other and they can move freely but together through the semiconductor. The thermal energy at room temperature can easily dissociate free

excitons. Because of this, they can only be measured at low-temperature spectroscopy. When they recombine, the photon energy will be less but close to the band gap energy.[53]

The second kind of exciton is the bound exciton. The electron and hole are strongly attracted to each other and are closer together. The bound exciton gets usually bound to impurities or lattice defects in the crystal. Due to this, they are less mobile than the free excitons. When they recombine, the photon energy will be less than the energy of the free excitons.

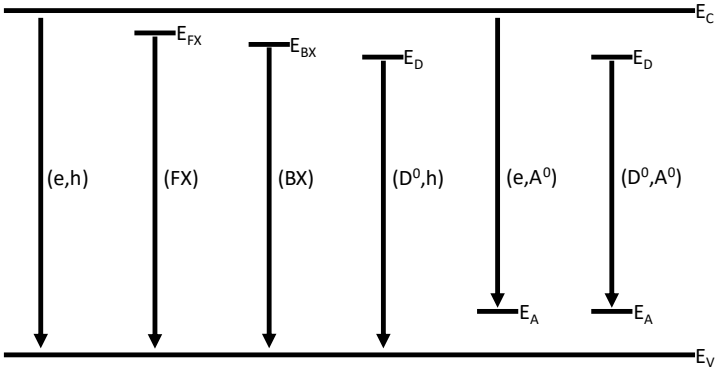

Figure 27: Selection of possible radiative recombination processes in a semiconductor. (FX) free exciton, (BX) bound exciton, (D) donor, (A) acceptor

Impurities and defects can act as donators and acceptors in the crystal. A donator can be described as an additional energy state underneath the conduction band and an acceptor can be described as an additional energy state above the valence band. The electrons and holes can fall into the states, and the following recombination will create a photon with a unique energy that is less than the band gap energy of the material. Different kinds of peaks in the measured spectrum can, therefore, be associated with different kinds of impurities.

Photoluminescence can not only be used to study bulk material properties. Optical nanostructures like quantum wells, dots and wires will show different kinds of luminescence behavior according to the quantum confinement. While this work does not contain specific nanostructures, the previously described stacking faults act as a kind of quantum well. The confinement will result in a specific peak in the spectrum that can be associated to the stacking faults[54].

To perform a photoluminescence measurement, a specific setup is required. A laser with a photon energy above the bandgap energy is used to excite the electrons from the valence band. The sample itself is placed inside a cryostat that can be cooled by liquid helium. The light from the recombination process is collected into a monochromator and detected by a CCD sensor.

5. Experimental Details

For a better understanding of the remote epitaxy process, it is essential first to describe the standard epitaxy process of cubic GaN. The following chapter is a detailed description of the epitaxy process. It starts with a description of the used substrate material and follows with a description of the used chemical cleaning steps. Afterwards, the epitaxy process inside the MBE is described step by step.

The second chapter uses the previously mentioned characterization methods to measure the characteristics of an ideal 600 nm c-GaN layer. The results are used in the later chapters to make comparisons between the c-GaN grown with and without remote epitaxy.

5.1 Epitaxy of cubic GaN

In the realm of heteroepitaxial growth of c-GaN, the most optimal available substrate material is 3C-SiC (001). For the purpose of this research, a 3C-SiC/Si (001) pseudo substrate was used. The substrates were acquired in the form of 10 cm wafers from the company NovaSiC. These substrates consist of a 500 µm thick Si wafer. On top of this Si wafer, a 10 µm thick layer of 3C-SiC (001) was deposited using a CVD step. Notably, the orientation of the substrate surface aligns with the (001) plane. The average surface roughness of the NovaSiC substrate is between 0.3 nm to 0.4 nm. Considering the lattice constant of 3C-SiC of 0.43596 nm, this represents an optimal polished surface.

For the epitaxy, the substrate wafers have to be cut into smaller pieces of 1 cm by 1 cm. This is necessary to mount them on the sample holder for the MBE. Afterward, the newly cut piece must be chemically cleaned. The samples will be cleaned with acetone for 5 minutes in an ultrasonic bath to remove possible dirt particles from the cutting. Afterward, the samples will be cleaned again with isopropyl alcohol for 5 minutes in the ultra-sonic bath. The last step is to remove the oxide layer on top of the 3C-SiC layer. The SiO_2 has to be removed by a hydrofluoride (HF) acid step. For this, a buffer oxide etch (BOE) consisting of a mixture of NH_4F and HF is used. The concentration of HF in this mixture is 8%. The samples will be immersed in the BOE for 8 minutes. After this step, the sample is ready to be mounted on the substrate holder and transferred into the MBE chamber.

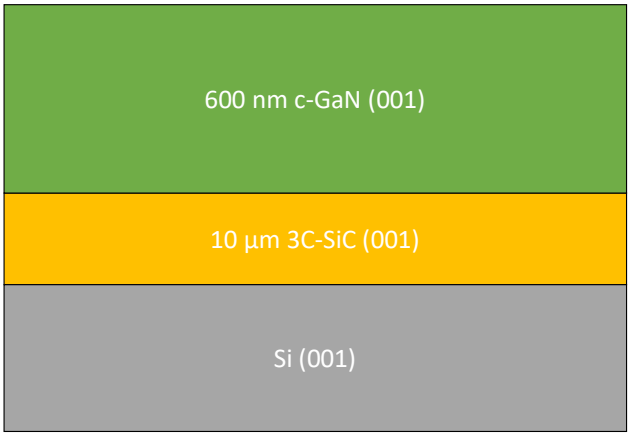

Figure 28: Example of a sample structure of a c-GaN layer grown on a 3C-SiC/Si (001) pseudo substrate.

The previously best possible c-GaN layers were grown with a gallium flux of 3.6×10^{14} atoms $[cm^2\ s]^{-1}$, and the plasma source was operated with an RF power of 260 W and an N_2 flux of 0.5 sccm. Under these conditions, the growth velocity is 150 nm h^{-1} or 0.4 Å s^{-1}. The work of Schörmann et al.[55] describes the growth process in more detail. After a growth time of four hours, a 600 nm thick c-GaN can be grown. The resulting sample structure can be seen in Figure 28.

At the beginning, the sample is heated to 900°C and is deoxidized by short aluminum depositions. This step is called aluminum flashes. The aluminum atoms will bond to the surface oxygen atoms and remove them from the 3C-SiC surface during evaporation[17].

Afterward, the substrate temperature is lowered to 740°C. Since the thermocouple temperature is not perfectly accurate, gallium flashes were performed to adjust the temperature according to the evaporation and deposition rates of gallium. Figure 29 shows the intensity of the RHEED reflection during the gallium flashes. The ratio between the slope during the deposition and evaporation is called the sticking coefficient. The best growth conditions are for a sticking coefficient of 0.5. A sticking coefficient of 0.5 means that 50% of the deposited Ga atoms will evaporate and not be incorporated into the layer.

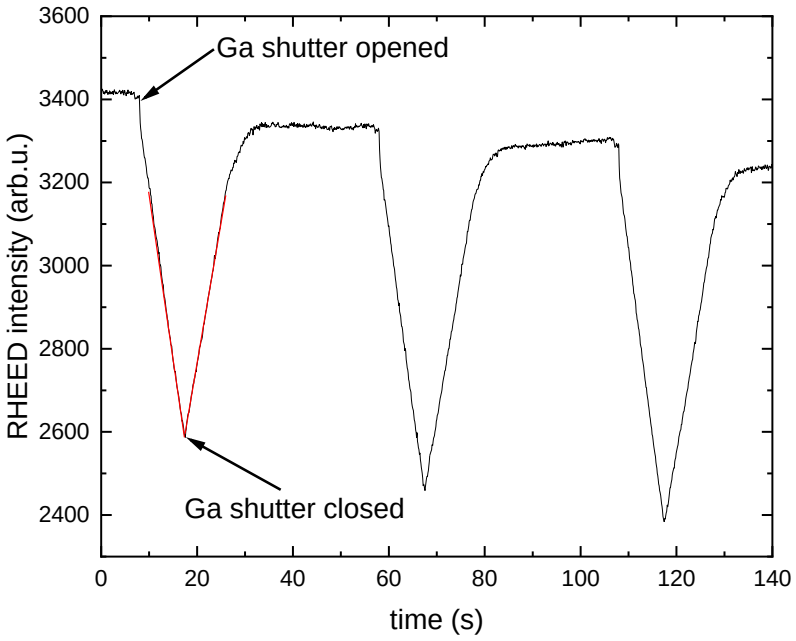

Figure 29: Intensity of the RHEED reflection plotted overtime during the gallium flashes

After the aluminum and gallium flashes, the growth process is started by depositing gallium for 7 seconds. After the seven seconds, the nitrogen shutter is opened additionally. Both shutters are kept open for a duration of 30 seconds. Then, the growth is stopped for 30 seconds before the process starts again, with gallium being deposited for 7 seconds. These steps will be repeated ten times.

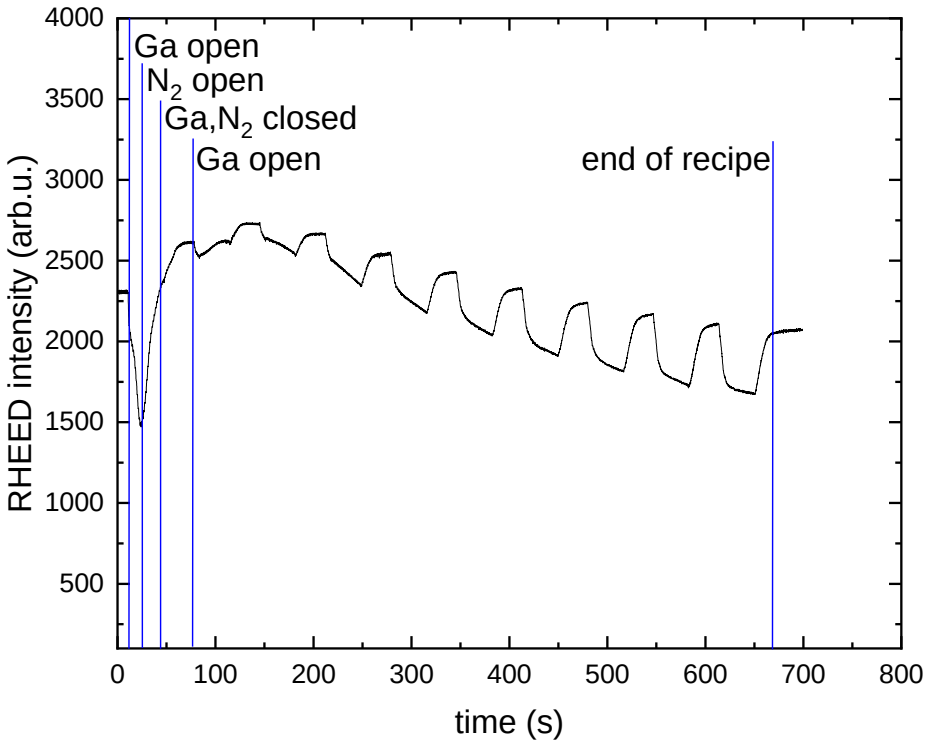

Figure 30: Intensity of the RHEED during the start growth recipe. The growth is segmented into 30-second intervals followed by 30-second-long pauses.

The change in the RHEED intensity during this growth recipe can be seen in Figure 30. During the initial start of the recipe, the intensity falls rapidly. As soon as the nitrogen source is opened, the intensity rises again. During the next cycles, the intensity falls slightly. However, with each growth interruption, the intensity begins to rise again. During these interruptions, the surface atoms have a short time to rearrange themselves and migrate to energetically favorable positions. Since the heteroepitaxial aspect of the growth process is the main cause of defect formation, these growth pauses can help to reduce the defect density and surface roughness.

Simultaneously, the RHEED pattern changes into a point pattern during the first three to four cycles. This indicated the formation of 3D islands on the surface. Due to the high lattice mismatch the nucleation layer tends to form islands to reduce the strain. During the following growth cycles, the form of the points changes slowly into an elongated ellipse, and an underlying line pattern begins to form. This indicates the shift from a 3D island surface to a smoother 2D surface. With each growth cycle, the intensity of the line pattern increases further, and the point pattern loses intensity.

In the next step of the process, continuous growth is initiated. By utilizing the calibrated gallium sticking coefficient, it is possible to deposit a monolayer of gallium and maintain it on the surface throughout the entire growth duration. This monolayer increases the adatom diffusion length on the surface[56–58].

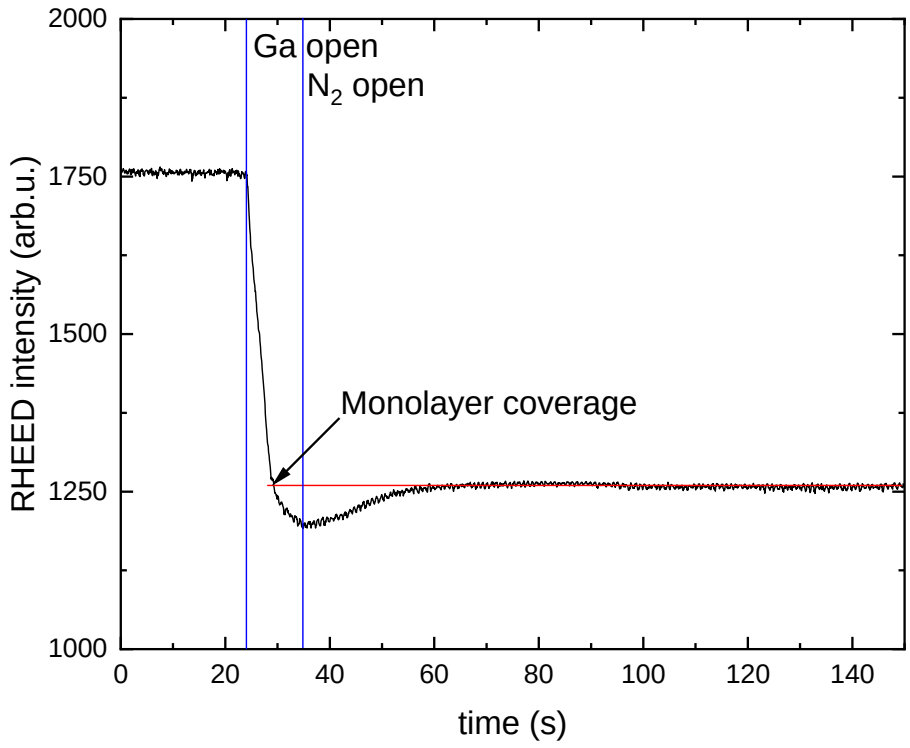

Figure 31: RHEED intensity during the start of the continuous growth.

Figure 31 serves as a visual showcase of the shifts in the RHEED intensity during the beginning of the continuous growth process. At the beginning, the gallium shutter is opened. The RHEED intensity immediately begins a steady decline. This decline unfolds in

a consistent manner. However, after approximately seven seconds, a noteworthy change occurs. The rate of intensity decline changes and slows down. This point results in a visible kink in the graph. The transition signifies that the surface has reached full coverage by a gallium monolayer. After another seven seconds, the nitrogen shutter was opened. Ideally, with a stochiometric balance of nitrogen and gallium supply, the monolayer coverage persists throughout the growth. This is verified by the fact that the RHEED intensity rises again to the height of the initial monolayer kink. The intensity should remain constant throughout the further growth. If the intensity does not settle at the monolayer coverage, the gallium sticking coefficient has to be optimized again by slightly changing the substrate temperature. The growth should be interrupted every 30 minutes to ensure ideal conditions for the complete process.

5.2 Characterization of a cubic gallium nitride sample

In the following chapter, the characterization of a cubic GaN layer is discussed. The characterization methods described in chapter 4 were used to analyze a standard c-GaN layer for future comparisons. For these characterizations, the sample GNL2998 was used. This name stands for gallium nitride (GN-) sample grown by Littmann (-L) number 2998. It is the 2998th sample grown in the used MBE system. The sample is 580 nm thick and was grown according to the description in chapter 5.1.

The first characterization of the sample was done by the RHEED system directly after the end of the growth. Figure 32 shows the RHEED pattern at the end of the growth process. By comparing the observed pattern with the ones shown in Figure 15, we attribute it to a streaky pattern. This is equivalent to a flat surface with small domains[41]. Furthermore, it shows a 4-fold reconstruction. This can be identified by the three weaker lines in between. Since the pattern has the same reconstruction when the sample is rotated by 90 degrees, it can be concluded that the reconstruction is a 4x4.

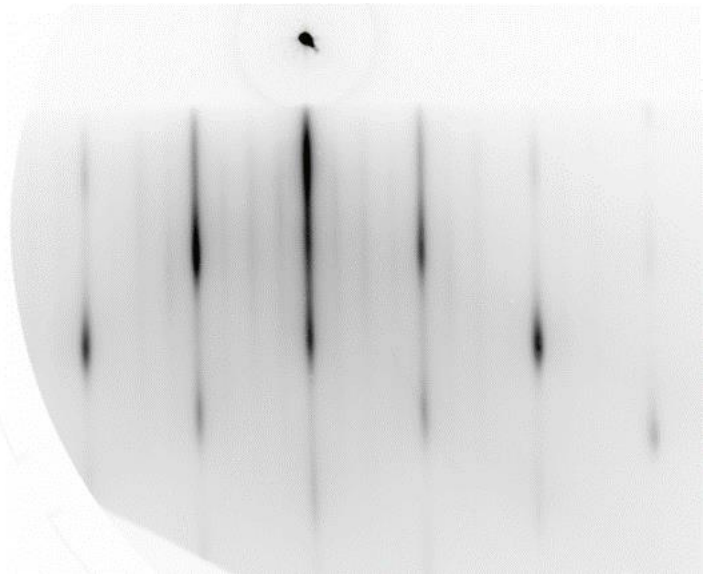

Figure 32: RHEED-pattern of a 600 nm thick GaN layer at the end of the growth process.

The flat surface indicated by the RHEED pattern was further analyzed by AFM measurements. In Figure 33, the images taken by the AFM are shown. The measurements were performed in a 10 µm by 10 µm area and a 5 µm by 5 µm area. The root mean square of the surface roughness for the 10 µm measurement is 3.9 nm. This is an increase by one order of magnitude compared to the used 3C-SiC/Si substrates. The main reason for this increase is the high lattice mismatch. The highest increase of the surface roughness occurs immediately at the beginning, caused by the 3D island growth.

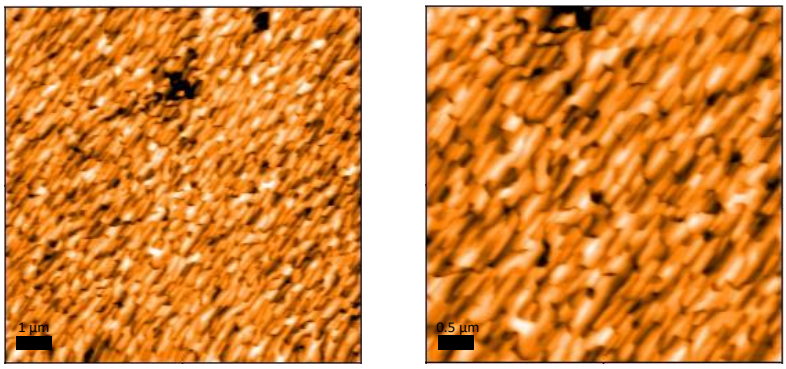

Figure 33: AFM image of a 580 nm thick c-GaN layer in a 10 µm by 10 µm and a 5 µm by 5 µm area. The roughness for the 10 µm by 10 µm area is 3.9 nm.

RHEED and AFM measurements serve as valuable tools to gain information about the sample surface properties. HRXRD and PL measurements were employed to characterize the bulk crystal. Rocking curve measurements were performed to determine the FWHM of the (002) reflection. This value can be used to compare the defect densities quantitatively. A smaller value indicates a lower defect density. The rocking curve measurements were carried out twice. For the second measurement, the sample was rotated by 90°. The resulting curves can be seen in Figure 34. For future comparison, the average value of both FWHM is used. The average FWHM of the sample GNL2998 is 29.8 arcmin.

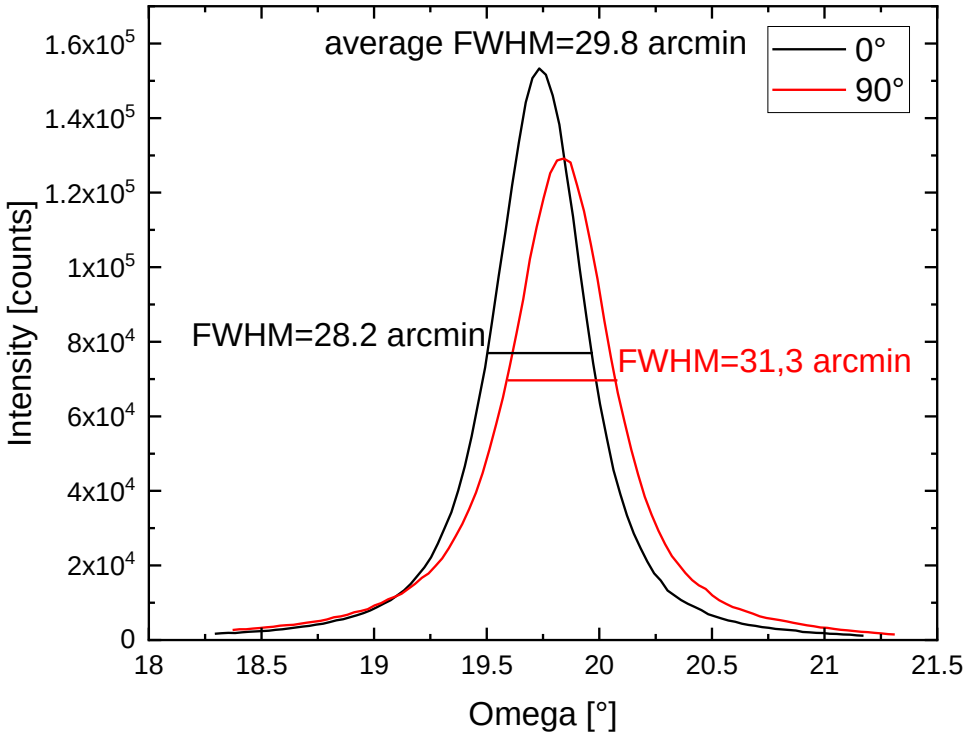

Figure 34: Omega rocking curve of the (002) reflection of the sample GNL2998

Additionally, the RSM of the (002) reflection was measured two times for the 0° and 90° direction. The first one is shown in Figure 35. The hexagonal reflections mentioned in chapter 4.1 should be inside the three marked areas. Since the intensity of these reflections cannot be distinguished from the background noise, the hexagonal inclusions

are below 1%. However, the existence of the lines implies that stacking faults are present in the crystal.

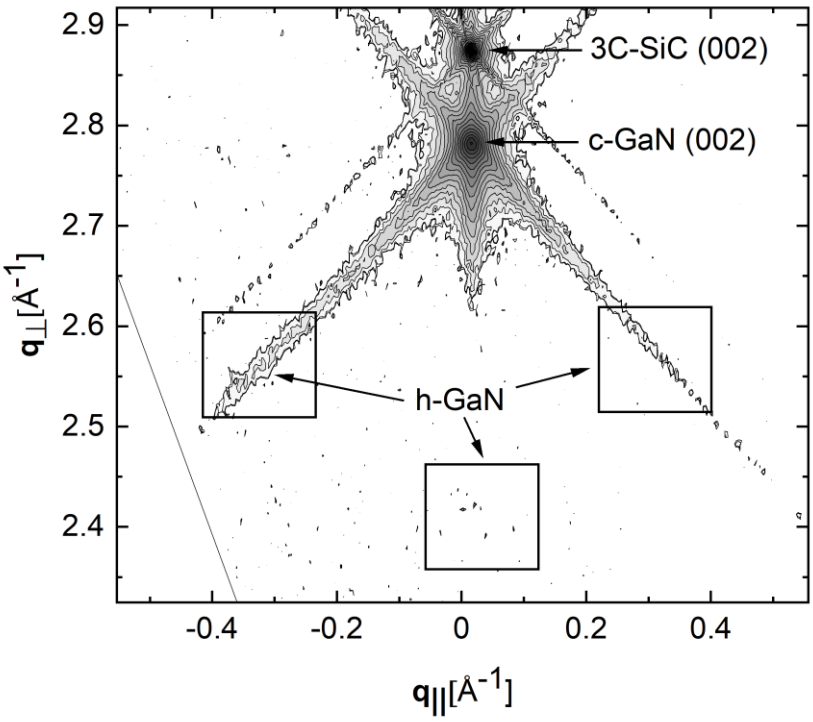

Figure 35: RSM of (002) reflection of the sample GNL2998. The boxes mark the areas where the hexagonal reflections would be located. The intensity of the hexagonal reflections in this RSM is below 1% in comparison to the cubic reflection.

Additionally, PL measurements of the sample were performed. The PL spectrum of the sample was obtained using an Nd:YAG laser with a wavelength of 266 nm. The laser power was set to 5 mW. The samples were cooled to a temperature of 13 K within a cryostat to achieve optimal conditions for the PL measurements. Cooling the sample is crucial as it minimizes thermal effects that can broaden spectral lines and obscure important features in the PL spectrum.

The resulting PL spectrum is depicted in Figure 36. Two key features are the bandgap energies at 0 K for cubic GaN and hexagonal GaN, which are marked at 3.28 eV and 3.47 eV, respectively[59]. Interestingly, the spectrum shows no peaks beyond the cubic bandgap energy. This suggests that the presence of hexagonal inclusions in the sample is minimal. This observation aligns with the results from the RSM measurements, providing consistent evidence for the sample's composition.

Another notable feature in the spectrum is the excitonic peak, denoted by (X), which is located slightly below the bandgap energy at 3.25 eV. Furthermore, there are additional peaks at lower energies, marked as (D^0,A^0)[22,60,61]. These peaks represent various donor-to-acceptor transitions.

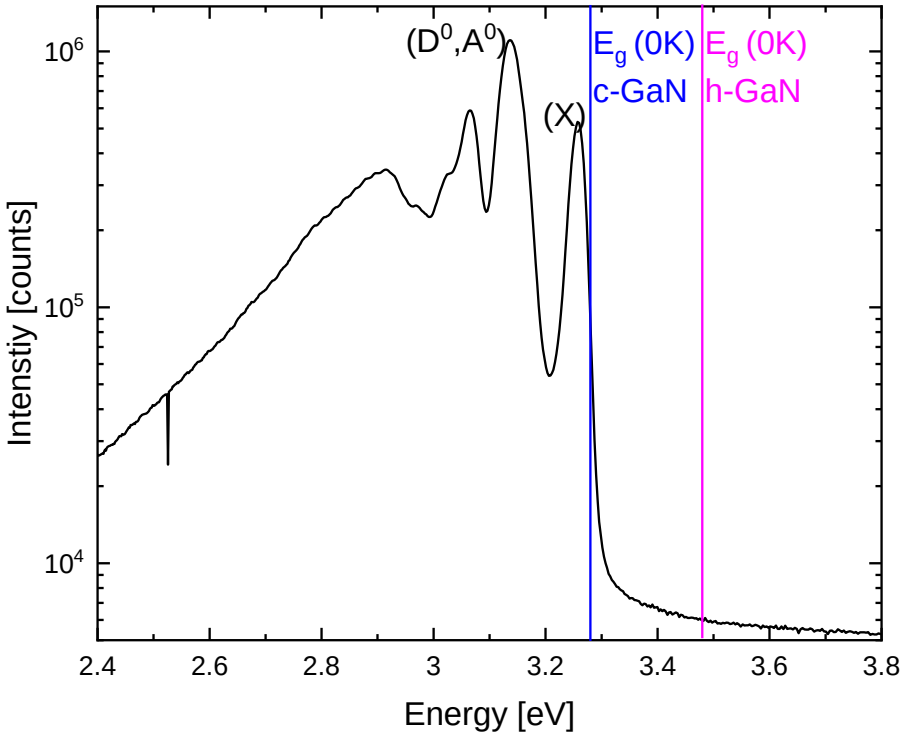

Figure 36: Spectrum of PL measurement of the sample GNL2998. The bandgap energy of the cubic and hexagonal GaN are marked. The excitonic (X) and donator to acceptor transition (D^0,A^0) are located below the cubic bandgap energy. There is no distinct peak that can be assigned to the hexagonal phase.

The most important values of the characterization are summarized in Table 2. These values will be used as reference values for comparisons in the following chapters.

Table 2: Basic parameters of the sample GNL2998

Sample	AFM roughness in nm [10x10] µm²	FWHM in arcmin	Hexagonal inclusions	GaN layer thickness in nm
GNL2998	3.9	29.8	<1%	580

6. Remote epitaxy

This chapter describes the development of the remote epitaxy process for the epitaxy of c-GaN. In the beginning, the sample preparation is described. The graphene transfer process is the main difference from the previously mentioned sample preparation. Subsequently, the initial attempts to grow on the graphene-covered substrate are examined. The following subchapters delve into the various optimizations made to the growth process. Each optimization is analyzed with the previously mentioned characterization methods and compared to the original c-GaN layer, which was the subject of the previous chapter.

6.1 Sample preparation and graphene transfer

As discussed in the previous chapters, the growth process of remote epitaxy is being adapted for the growth of cubic gallium nitride. The same 3C-SiC/Si (001) substrate material is used for the process. The 10 µm thick 3C-SiC layer has an average surface roughness of about 0.35 nm, which is equivalent to the monolayer thickness. This low value is essential to ensure perfect contact between the 3C-SiC and the graphene.

Different methods to cover the substrate with a graphene monolayer have been discussed in chapter 2.9. For this experiment, the transfer graphene was chosen due to its cost efficiency and quick application. The “Trivial Transfer” graphene from ACS Material was used. This graphene is delivered on a polymer and covered with a polymethyl methacrylate (PMMA) photoresist. The manufacturer states that the graphene is produced with a CVD process on copper foils[62]. It is afterward covered with a photoresist, and the copper foil is removed by an etching step. In the end, it is transferred onto a polymer and delivered to the customer.

The graphene can easily be transferred onto the target substrate. However, before that, the 3C-SiC substrate is thoroughly cleaned by an acetone and isopropyl cleaning step. A thin silicon oxide layer will be on the surface of the 3C-SiC due to natural oxidation. It is necessary to remove this oxide layer before the graphene transfer to ensure the best possible growth conditions. This should be done immediately beforehand. Otherwise, a new oxide layer will form. For this purpose, the substrate will be immersed in hydrofluoric acid.

The graphene is inserted into water to separate it from the polymer. The polymer will soak up the water and sink to the bottom, while the graphene will swim on top of the water surface. The target substrate can be used to pick the graphene out of the water, see Figure 37. The sample needs to dry for 30 minutes and then be baked for 20 minutes at 100°C to remove the water residues between the substrate and graphene layer.

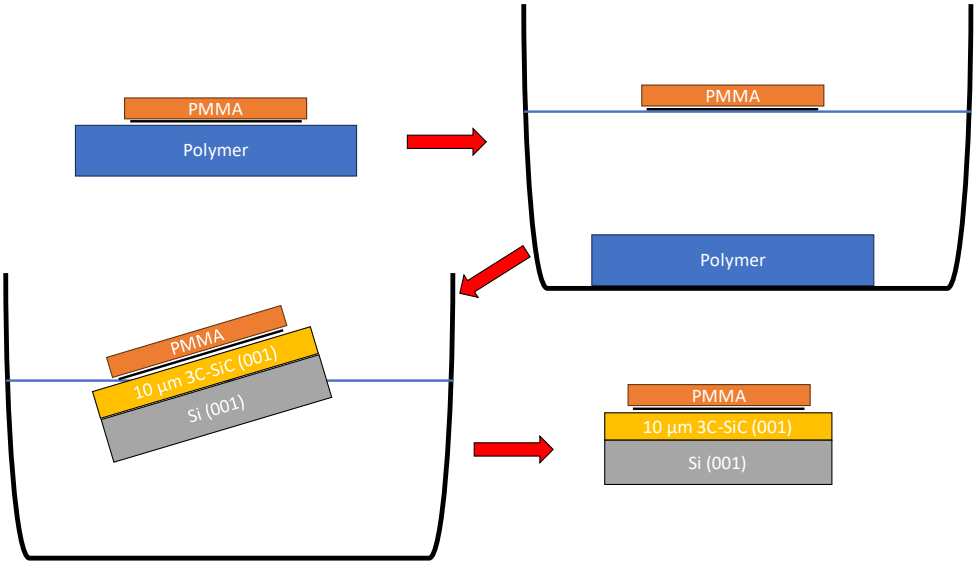

Figure 37: Visualization of the graphene transfer process onto the target substrate. First, the polymer with the graphene is placed into water. Then, the Graphene and PMMA film separate from the polymer and swim on the surface. Afterward, the target substrate can be used to take the graphene layer out of the water.

When the sample is fully dried, the PMMA layer must be removed. This can be done by immersing it in 50°C hot acetone for 30 minutes. However, this process will not remove the photoresist altogether. Small micrometer-sized residues will remain on the surface. An SEM image of these residues is shown in Figure 38 a). The work of Pirkle et al.[63] suggests a thermal vacuum annealing step to remove the residues.

The first attempts were performed by heating the sample to 750°C in a vacuum chamber for 10 minutes. However, the best result was achieved by increasing the temperature to 900°C. The result of the cleaned graphene surface can be seen in Figure 38 b). It is important that this process will only work for materials with high thermal stability. After this last cleaning step, the sample is ready for the epitaxy step.

This thermal cleaning process requires the use of a substrate material that can withstand high temperatures. If this transfer process is used for other material systems, like gallium arsenide, another cleaning process is necessary. The best alternative is to use a low-density inductively coupled plasma.[64,65]

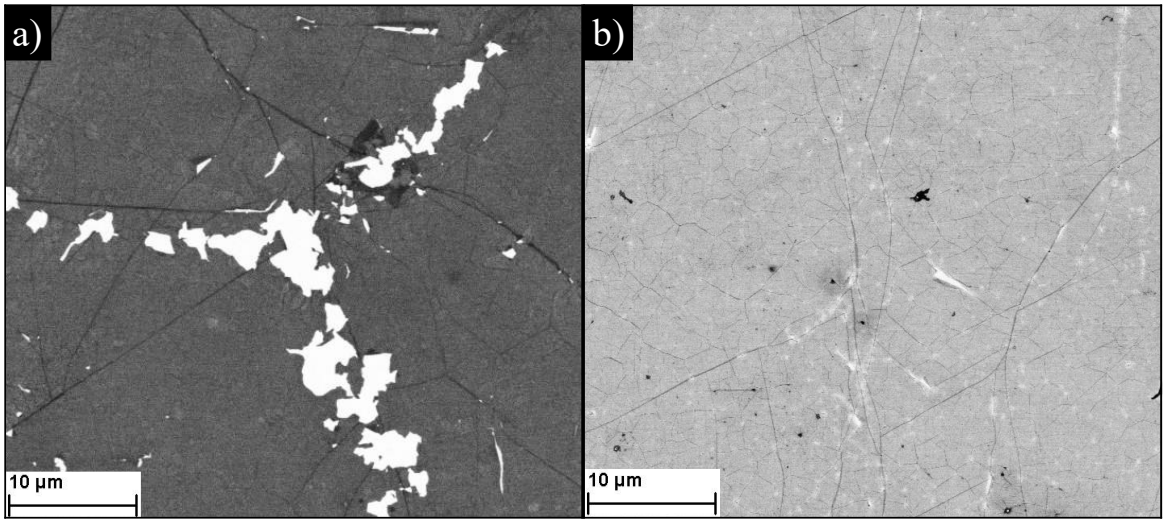

Figure 38: SEM images of the graphene transferred on a 3C-SiC/Si (001) substrate. a) After the acetone cleaning step with (white) residues of the PMMA photoresist. b) After the additional thermal cleaning step, the PMMA is fully removed. Previously published in [66].

After a closer examination of the SEM images, the presence of dark lines throughout the surface becomes apparent. These lines are the domain boundaries of graphene. Throughout the CVD process, distinct nucleation centers with varying orientations are formed. As the growth proceeds, they continue to expand until they eventually merge. The resulting visible domain boundaries align with these merging points. This process is further discussed in the work of Xiang et al.[67]. Figure 39 shows a diagram adapted from Xiang's work. It visualizes the domain formation during the nucleation of a 2D material on a sapphire substrate. The red dots symbolize the nucleation sites, and the red polygons mark the domain regions. Mathematically speaking, the domains form according to a Voronoi diagram. A Voronoi diagram partitions a 2D plane into regions defined by the closest randomly placed points. Each region is uniquely associated with its nearest point.[68]

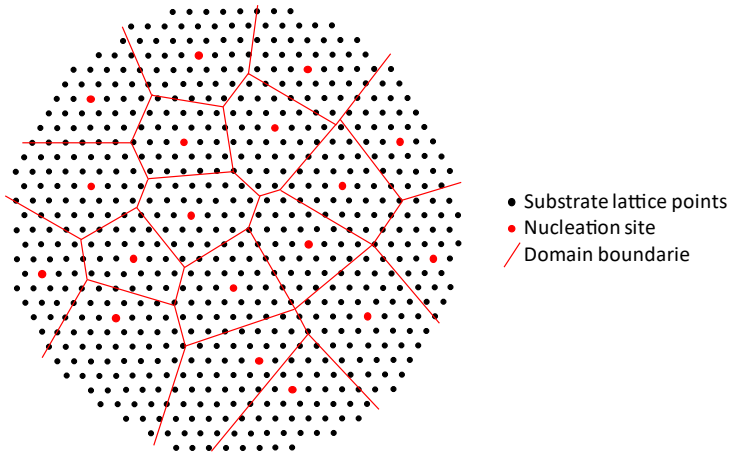

Figure 39: Illustration of a Voronoi diagram of the nucleation process of a graphene layer. The domain regions (red polygons) with the nearest nucleation sites (red dots) on a sapphire lattice. Adapted from [67]

The average diameter of these domains is one micrometer. It is worth noting that the 3C-SiC substrate also consists of antiphase domains. However, the average diameter of these is ten times bigger. Therefore, the influence of the graphene domain boundaries is more dominant[69].

6.2 Comparison of the graphene quality of two different manufactures

At the time of this work, there were two different manufacturers for transfer graphene monolayers. The first one is the previously mentioned ACS Material. The preparation and cleaning process was developed with the transfer graphene they supplied. ACS Material is an American chemical supplier located in Pasadena California, specialized in advanced nanomaterials. They guarantee monolayer graphene, which they verified by Raman spectroscopy.

The second supplier is Graphenea. It is a Spanish company located in San Sebastián. They provide a wide range of graphene-related products. One of these products is a transfer graphene that is comparable to the one by ACS Material. It is also a graphene Monolayer covered by a PMMA photoresist layer delivered on a polymer. They also guarantee a monolayer characteristic of the graphene.

Raman spectroscopy measurements were applied to verify the claims of the manufacturers. For each manufacturer, one sample was prepared according to the

preparation procedure discussed in the previous chapter. The Raman measurements were performed by Elias Kluth from the Otto-von-Guericke University Magdeburg. For these measurements, a 532 nm Nd:YAG laser was used. The results are shown in Figure 40. The upper diagram shows the measurement for the graphene monolayer from Graphenea, and the bottom diagram shows the measurement for the ACS Material graphene. Both measurements are compared to a Raman spectrum of graphite sample shown in blue.

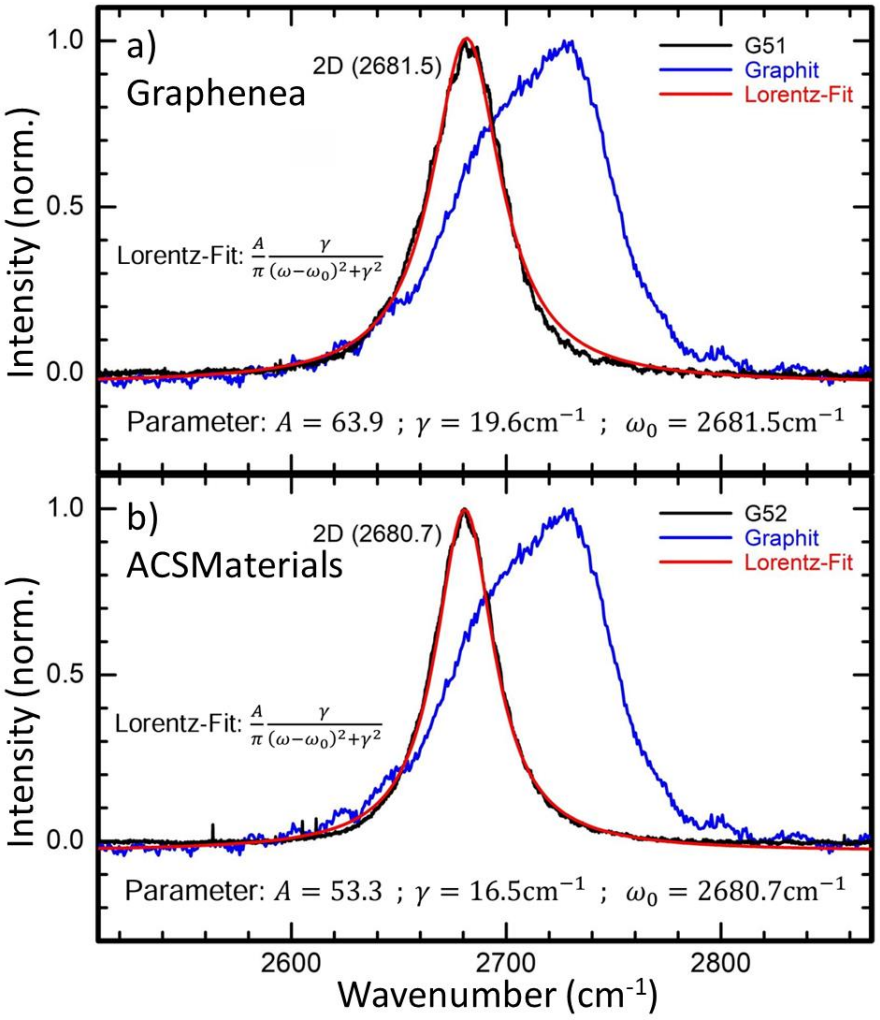

Figure 40: Raman spectra for a) Graphenea and b) ACS Material graphene monolayers. Both spectra are compared to a Raman spectrum of graphite (shown in blue). Both exhibit a single peak consistent with monolayer graphene. However, ACS Material's curve is narrower, indicating superior quality.

The Raman spectra of the graphene samples were then fitted with a Lorentz-Fit according to the formula shown in the diagram. The parameter ω_0 determines the location of the maximum. Both values are close to the expected position of 2670 cm^{-1} for monolayer graphene[42,43]. Furthermore, both measurements seem to contain only one distinct peak

and not a band of multiple peaks, as can be seen for the graphite measurement. In conclusion, both graphene layers possess the required characteristics for monolayer graphene. However, the direct comparison between the two curves shows that the width of the ACS Material curve is smaller than the Graphenea measurement. The Lorentz-Fit contains the parameter γ, which determines the width of the curve. This parameter has the smallest value of 16.5 cm^{-1} for the ACS Material graphene. Since the width of the peaks increases for multilayer graphene, it can be concluded that the quality of the ACS Material graphene is the preferable choice.

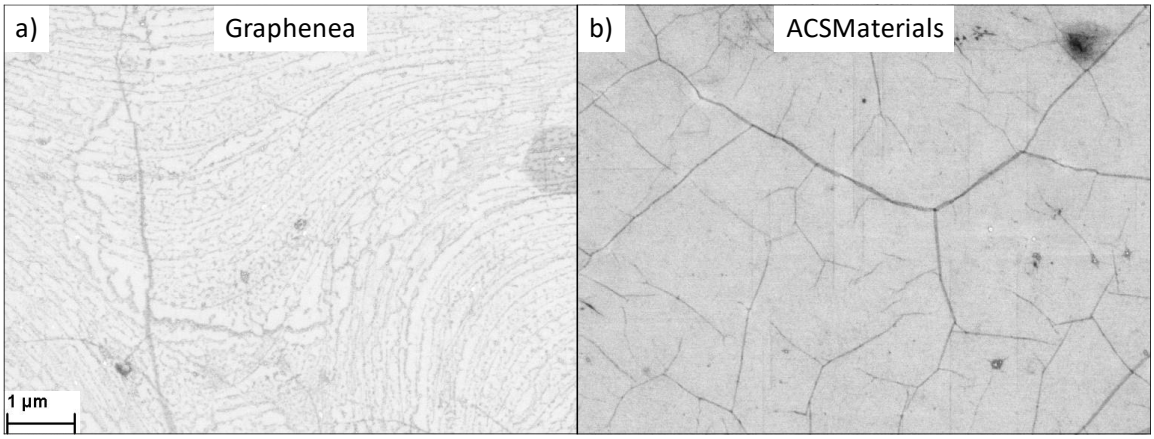

Figure 41: SEM images of the graphene-covered 3C-SiC surface. a) shows a graphene monolayer from the manufacturer Graphenea and b) shows a graphene monolayer from ACS Material

Additionally, the prepared samples were investigated by SEM imaging. Figure 41 shows a comparison between the two kinds of graphene. A significant difference between the two types of graphene becomes visible. While the ACS Material graphene contains strongly pronounced domain boundaries, the areas between them look smooth. The graphene layer from Graphenea, on the other hand, seems to be covered with different kinds of defects. It could be considered that this high number of defects is responsible for the broader peak in the Raman measurement.

In Conclusion, the ACS Material has a smaller peak width in the Raman spectra, and the SEM image shows a smoother surface. Both factors prove a higher quality for the ACS Material graphene. From here on forward, only the ACS Material graphene will be used.

6.3 Remote epitaxy of cubic gallium nitride

For a better distinguishability of each prepared substrate, an additional sample numeration was introduced. The first sample was named G1. G stands for graphene, and the number was increased with each new sample. When the sample is transferred into the MBE, it gets additionally the MBE sample number. A finished sample will then have a combined sample name of both numbers. One example of this is the sample G5_GNL3118.

The fully prepared and graphene-covered 3C-SiC/Si (001) substrate is then ready for the epitaxy process. The initial attempts to perform remote epitaxy were performed under the standard growth conditions described in chapter 5.1. However, one must keep in mind that the growth process cannot be fully adapted for the growth on graphene. The most significant change is that the interaction between the adatoms and the substrate is significantly weakened since the adatoms can no longer form covalent bonds and only interact with van-der-Waals forces.

One of the first and most noticeable deviations is seen when analyzing the RHEED pattern of the graphene-covered substrate. Comparing the patterns of samples with and without graphene yields significant insights, see Figure 42. The RHEED pattern for the graphene-covered sample distinctly portrays only the 0-diffraction order. A peculiar observation of this pattern is its independence concerning the orientation of the incoming electron beam. The sample can be rotated by 360° without changing the form of the RHEED pattern. This is hypothesized to be due to the differing orientations of the domains in the monolayer of graphene, which do not have a preferred direction.

Even though the RHEED pattern looks different from the uncovered 3C-SiC substrate, the pattern still contains an intense specular spot, which allows to perform Ga-flashes. However, it turned out that the Ga sticking coefficient was higher on the graphene monolayer than directly on the 3C-SiC for the same temperature. Since it is unknown which Ga sticking coefficient is the best for the growth on graphene, it was chosen to keep the same substrate temperature used in the standard growth process of 740°C. Additionally, the sticking coefficient will change as soon as the graphene monolayer is completely covered by GaN. At that point, it is probably better to use a temperature, which ensures a sticking coefficient of 0.5.

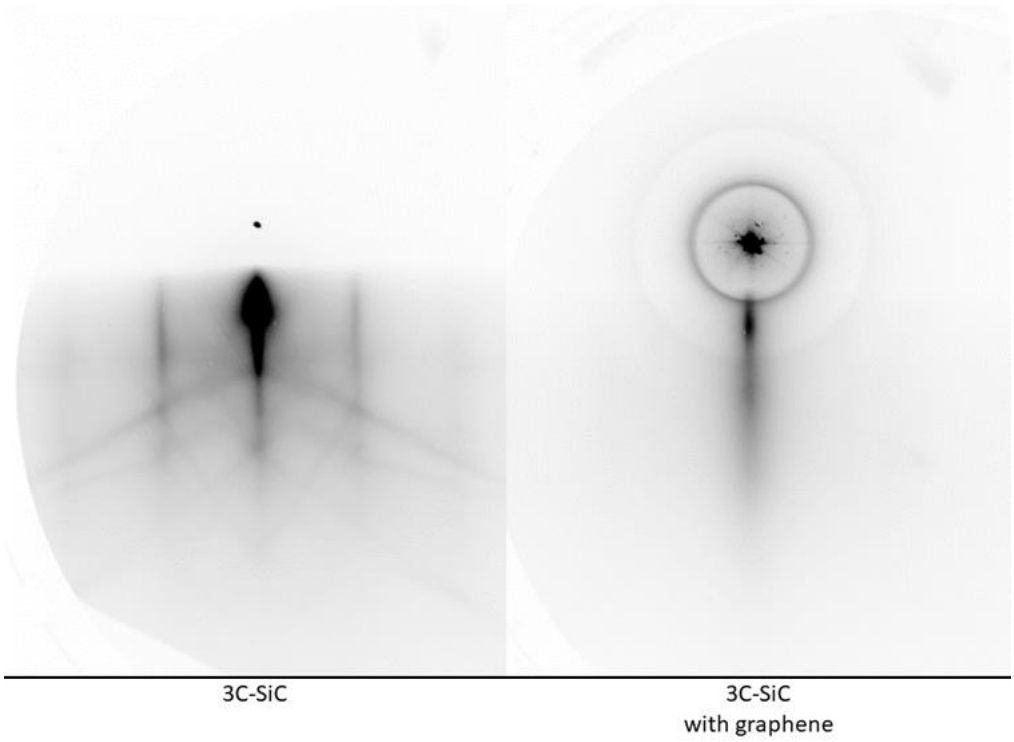

Figure 42: Comparison of the RHEED pattern of a 3C-SiC substrate without (left) and with (right) a graphene monolayer.

In the following part, the growth process of the first sample with the number G5_GNL3118 is described. The growth started at a substrate temperature of 740°C with the same recipe as discussed in chapter 5.1. The Ga shutter is opened first for seven seconds to deposit a monolayer amount of gallium. Secondly, the nitrogen shutter is opened, and the epitaxy process starts. After 30 seconds, the shutters are closed once again, and the growth is paused for 30 seconds. This sequence is repeated ten times.

The diagram in Figure 43 shows the change in the RHEED intensity during the first minutes of the growth. The diagram also contains the intensity data for the growth directly on the 3C-SiC layer, which has already been discussed in Figure 30. A rapid decrease in RHEED intensity can be observed when the growth recipe is started. This is a comparable observation to the growth without graphene. However, the first significant difference becomes visible when the nitrogen shutter is opened. Without graphene, the RHEED intensity begins to recover. In the case of the remote epitaxy process, however, the intensity drops even more rapidly. Additionally, during the pauses, the RHEED intensity would normally increase rapidly at first but reach a plateau after a short time. This plateau signifies that the unincorporated Ga atoms have evaporated, and the surface atoms have

settled. During the remote epitaxy process, the intensity does not reach a plateau. The intensity would further increase, even if the pauses were longer. This indicates that the surplus of unincorporated Ga atoms is higher and, therefore, the growth velocity is lower. As discussed previously, the nucleation probability is lower on the graphene monolayer caused by the lacking possibility to form covalent bonds. Therefore, a lower growth velocity was expected.

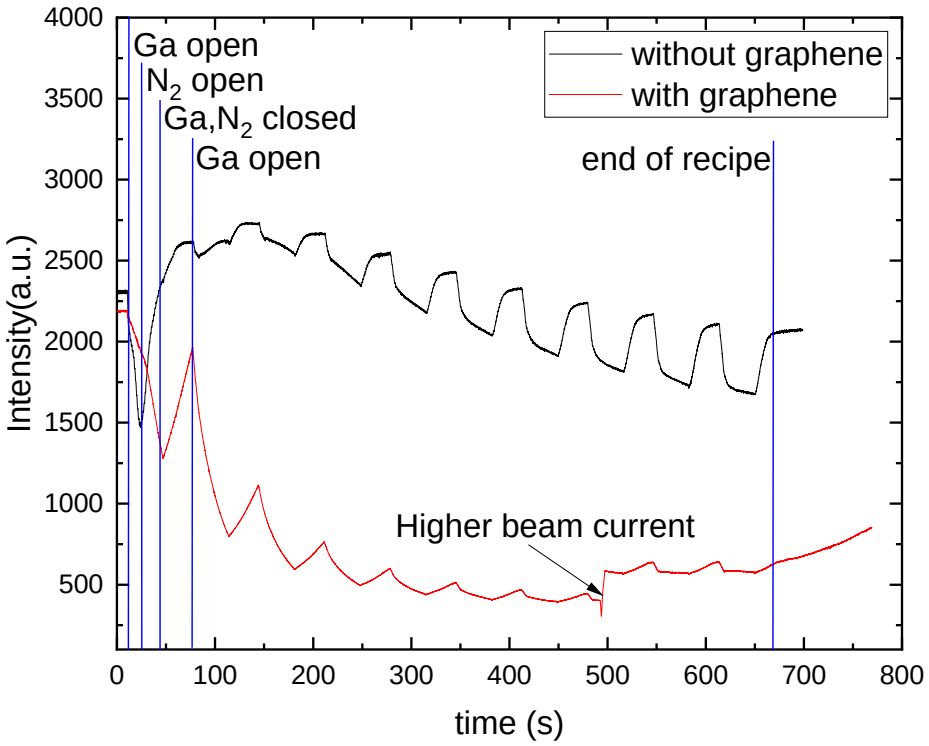

Figure 43: Comparison of the RHEED intensity over time during the start of the growth recipe. The growth is segmented into 30-second intervals followed by 30-second-long pauses. The standard growth without graphene restores the intensity during the growth pauses and ends at a comparable intensity level to the one it started at. The intensity during the remote epitaxy process decreases drastically. After 500 seconds, the beam current had to be increased to be still able to see the RHEED pattern.

Overall, the comparison also shows a high decrease in the RHEED intensity during the whole recipe. Meanwhile, the intensity during the standard growth process reaches approximately the same intensity level from the beginning in the end. The Intensity for the remote epitaxy decreases so much that it is necessary to increase the RHEED electron beam current to still be able to observe the RHEED pattern. As mentioned in chapter 3.2,

there is a correlation between the RHEED intensity and the surface roughness. This means that the surface roughness of the remote epitaxy sample can be expected to be much higher than the sample grown under standard conditions.

After the initial growth recipe, the continuous growth was started. However, due to the low RHEED intensity, it was not possible to calibrate the substrate temperature as accurately as it was done in Figure 31. The continuous growth was stopped after one hour to perform the other characterization methods. The RHEED pattern shown in Figure 44 was measured at the end of the growth on the graphene monolayer. A further increase of the electron beam current was necessary to create this picture. Especially the comparison to the background noise shows the weak intensity.

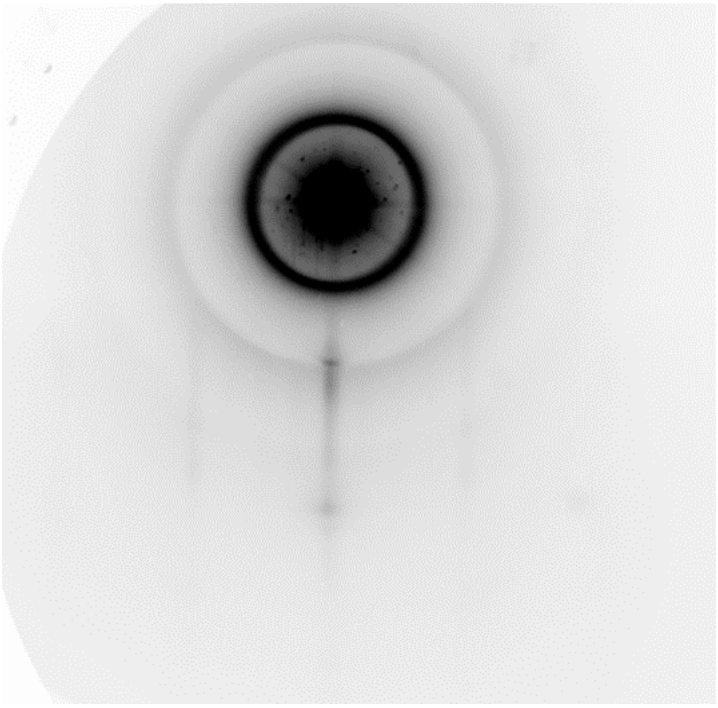

Figure 44: RHEED-pattern of G5_GNL3118 shows a low-intensity line pattern. The low intensity implies a high surface roughness.

SEM measurements can be employed to validate the hypothesis concerning increased surface roughness. The SEM image (Figure 45) reveals a predominantly polycrystalline GaN layer on the graphene-covered 3C-SiC/Si (001) substrate. An intriguing aspect of the SEM image is the discernible hexagonal form of numerous polycrystals, pointing towards significant hexagonal inclusion. The high difference in the height profile is already clearly visible in the SEM image. AFM measurements were not performed because it can be expected that the sample would wear down the cantilever tip during the measurement.

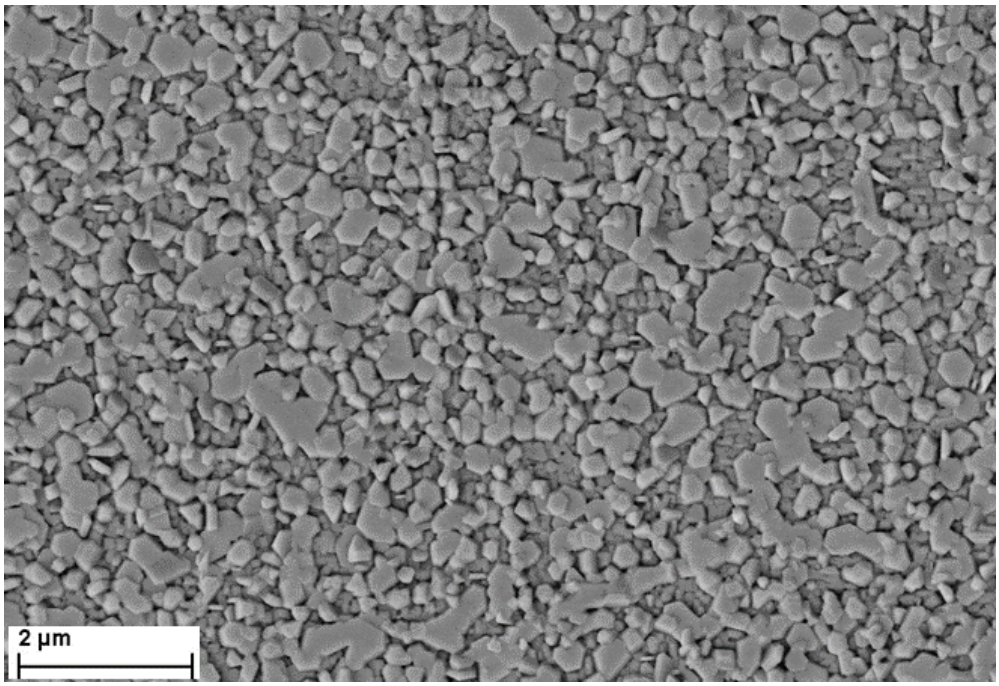

Figure 45: SEM-image of G5_GNL3118 shows a rough polycrystalline surface. The shape of the polycrystalline crystals implies a high amount of hexagonal GaN.

This high number of hexagonal inclusions can be verified by PL measurements. The PL spectrum in Figure 46 shows the measured spectrum at a temperature of 13K. The sample with graphene G5_GNL3118 is compared to a sample without graphene (GNL3006). The high amount of luminescence above the bandgap of cubic GaN indicates a high amount of hexagonal inclusions.

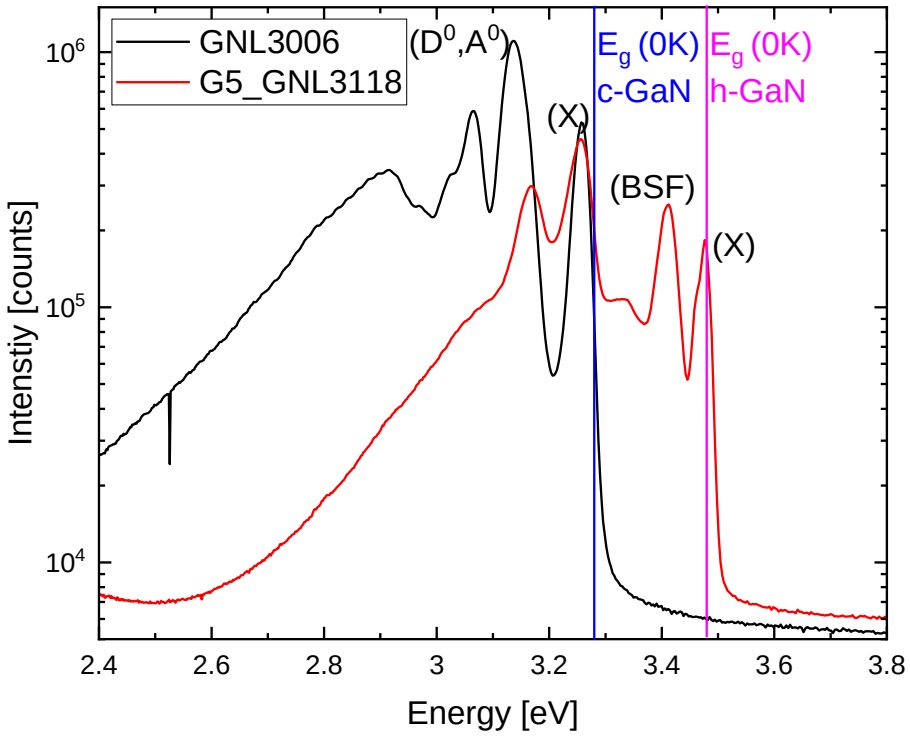

Figure 46: Spectrum of the photoluminescence measurement of G5_GNL3118 in comparison with the sample GNL3006 (without graphene). The remote epitaxially grown sample G5_GNL3118 has three distinct peaks above the cubic bandgap energy, which implies a high number of hexagonal inclusions.

In summary, this first attempt to remote epitaxially grow cubic GaN demonstrated the many challenges one must overcome to achieve a high-quality c-GaN layer. The most important part of the growth process is the nucleation phase. As the RHEED observations have shown, the nucleation on the graphene monolayer acts entirely differently due to the lack of covalent bonds. The SEM image also shows that there seems to be nearly no interaction with the underlying 3C-SiC substrate. The hexagonal form of the polycrystalline inclusions indicates that the majority of the nucleation happens in the h-GaN (0001) direction. Therefore, for the following samples, the primary focus was put on the growth starts.

6.4 Optimization of the growth recipe

The first step to optimize the nucleation step is to make changes to the growth recipe. Different changes were investigated. The length of the growth intervals and pauses were varied. The most promising results were achieved by reducing the intervals from 30 seconds to 15 seconds. By using this optimization of the growth recipe, it was possible to reduce the polycrystal nature of the epitaxial layer. By reducing the time length of the growth intervals, it was possible to grow samples like the SEM image shown in Figure 47 b). Besides the change of the recipe, the parameters and growth time of the sample G20_GNL3148 are identical to the previously discussed sample G5_GNL3118.

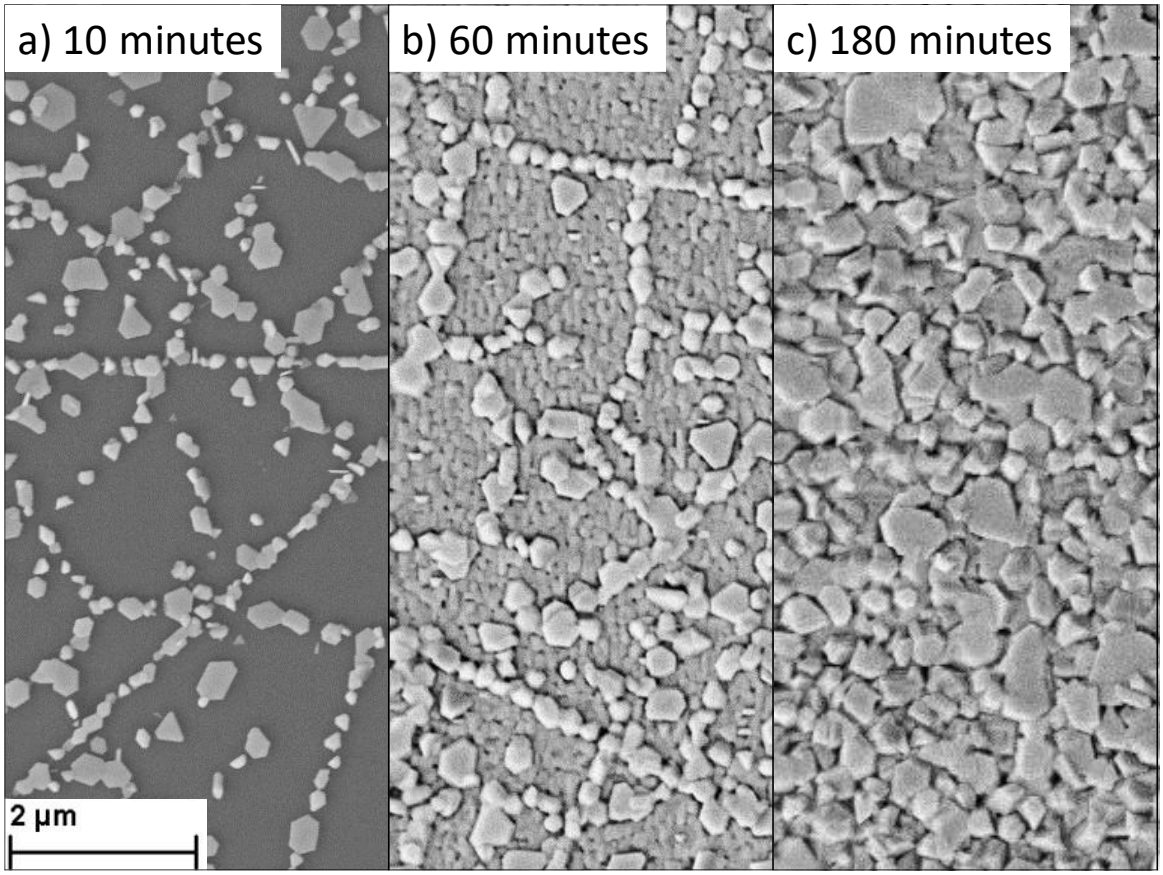

Figure 47: SEM image of a) after 10 minutes of deposition, the nucleation occurred only at the domain boundaries b) G20_GNL3148 after 60 minutes, the surface has been completely overgrown. The crystal structure is different between the domain boundaries and at the boundaries. c)G22_GNL3150 After 180 minutes, the surface turns into a completely polycrystalline structure, and the domain boundaries cannot be distinguished from the other parts.

Noticeable is that the layer still contains highly polycrystalline structures. However, these seem to be oriented along the lines of the graphene domain boundaries. In between these lines, a smoother layer has been formed. Even though these smoother layers still consist of smaller islands that have grown together. This indicates the nucleation process can be described as a Volmer-Weber process. While the areas in between the domain boundaries look smooth, the overall height profile of the sample is still too rough to perform AFM measurements.

To further understand this growth process, one has to look at the growth at the beginning. The SEM image shown in Figure 47 a) shows a GaN layer that was only grown for 10 minutes. It is noticeable that the immediate growth only occurs along the domain boundaries and other defects in the graphene layer. The areas in between seem to be uncovered at this point. This observation shows us that the defects in the graphene highly enhance the nucleation process. The adatoms seem to be trapped in these defects and forced to nucleate at a higher rate. Additionally, the nucleated parts have a hexagonal or triangular shape, which indicates that they are all hexagonal GaN.

The defect-free areas of the graphene, however, seem to be still uncovered after the first 10 minutes. This is understandable since the nucleation probability in the intact areas is reduced, which results in a delayed nucleation process. It can be expected that due to the shorter deposition times in the growth recipe, the nucleation was further delayed. However, this key aspect was beneficial to at least grow a smoother layer in between the domain boundaries.

But even with this adapted growth process, it is not possible to grow a high-quality homogeneous layer of cubic gallium nitride. After longer durations, the surface turns once again into a highly polycrystalline layer (Figure 47 c). The polycrystalline layer contains mostly hexagonal-formed pieces, which indicates a predominantly hexagonal GaN layer. This can be further verified by the PL measurements (Figure 48), which confirm no significant change in the number of hexagonal inclusions. In comparison to the first sample (G5_GNL3118), the intensity ratio of the hexagonal phase to the cubic phase remains almost unchanged.

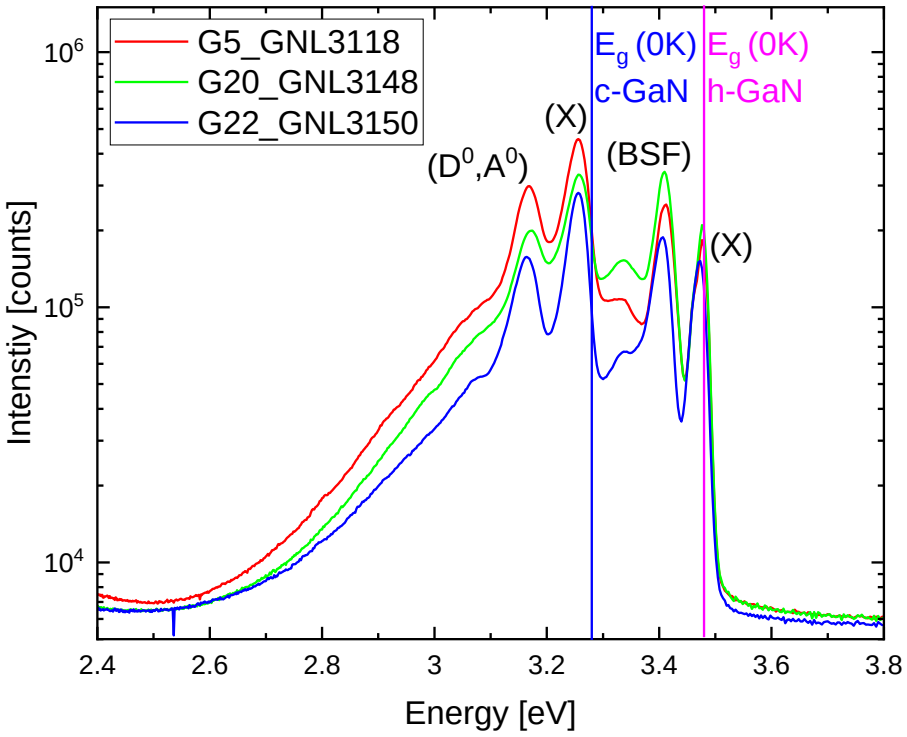

Figure 48: PL of samples up to G5_GNL3118, G20_GNL3148, and G22_GNL3150. The PL spectra only show small variations between the samples, suggesting that the amount of hexagonal inclusions does not change drastically due to the different growth conditions.

With the increased thickness of sample G22_GNL3150, it is possible to perform HRXRD measurements. The (002) RSM of the sample is shown in Figure 49. According to these measurements, the GaN layer does not only contain hexagonal inclusions. It consists of more than 80% of hexagonal GaN. The majority of the h-GaN has been grown in the (0002) direction. This means that the formation of the hexagonal phase occurred directly on top of the substrate surface and not on the (111) facet of the cubic crystal. The FWHM of the (002) reflection rocking curve has a value of 57.6 arcmin, nearly twice as high as the sample GNL2998 without the graphene.

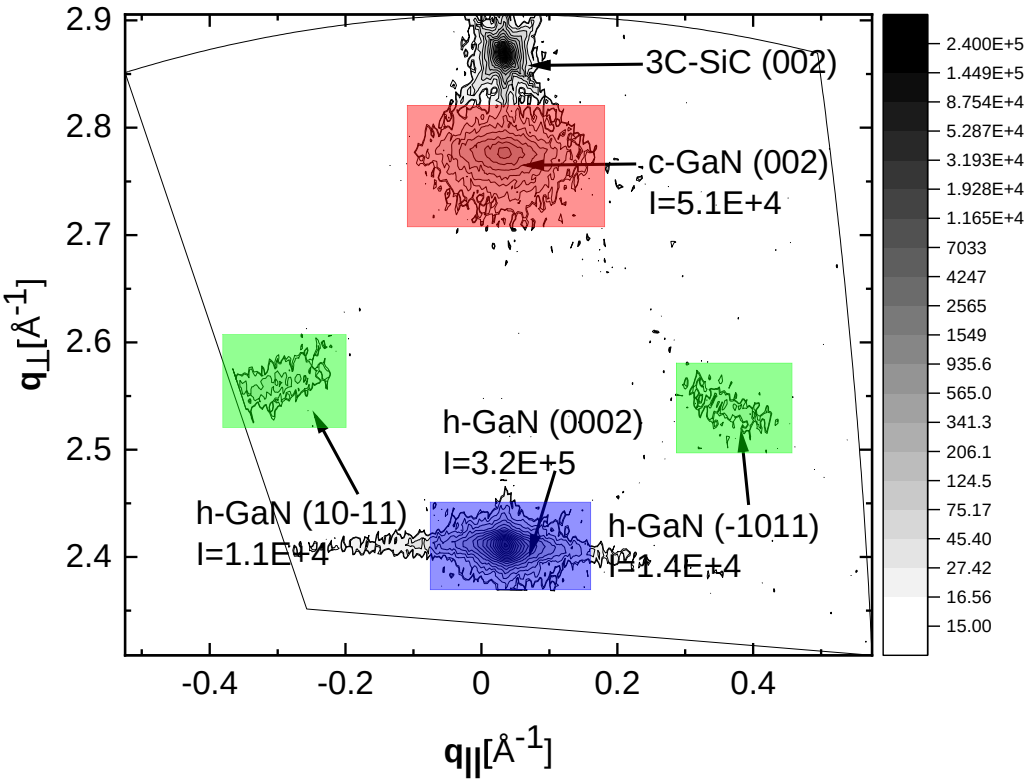

Figure 49: RSM of the (002) reflection of the sample G22_GNL3150. The highest integral intensity is assigned to the hexagonal (0002) reflection. The comparison of the intensities results in a composition of 80% hexagonal GaN. Small intensities for the h-GaN grown on the (111) facets of the cubic crystal are also visible. The color scheme is chosen according to the colors used in Figure 50.

To better understand the different crystal phases and orientations measured by PL and HRXRD, the schematic illustration in Figure 50 was created. It shows a substrate material (grey) covered with a monolayer of graphene. On top of the graphene, three possible kinds of orientations, measured by the RSM measurement, are visualized. The color scheme used is identical to the colored reflections in the RSM in Figure 49.

On the left side in blue is the hexagonal (0001) GaN phase. This phase is not the desired one, but it occurs when the interaction between the substrate and the epilayer is too weak. Since the majority of the RSM intensity of 80%, is attributed to this phase, it can be concluded that the influence of the substrate orientation is nearly nonexistent. The red cube in the middle symbolizes the cubic (001) GaN. This is the desired meta-stable phase. It is attributed to 15% of the overall RSM intensity. The third kind is the hexagonal GaN that grows on the (111) facets of the cubic crystal. To be more precise, this GaN phase can

be separated into four different orientations. The four orientations are shown in green on the right side of Figure 50.

Due to this separation into four orientations, it is also necessary to measure all four orientations independently with the HRXRD measurement. The RSM in Figure 49 contains two of the orientations labeled (10-11) and (-1011). One RSM contains the two opposite-located phases. It is necessary to rotate the sample by 90° to gain information about the other two. In both cases, the X-ray beam has to be parallel to the (110) plane of the cubic phase.

The number of hexagonal formations on the (111) facets of the cubic phase mainly depends on the growth mode. A 3D island growth of the c-GaN layer will enhance the growth on the facets. In contrast, the 2D growth mode, on the other hand, suppresses the nucleation on the facets since the surface of the epilayer will only consist of the (001) plane.

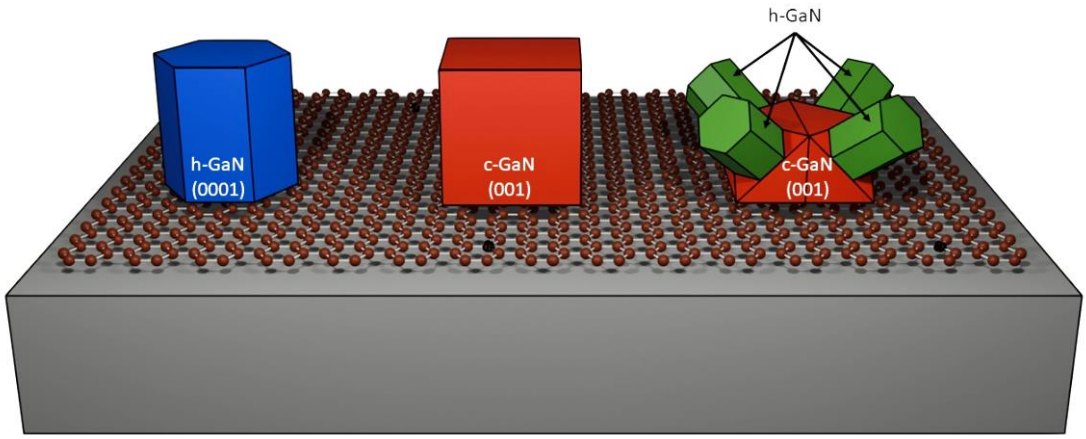

Figure 50: Schematic illustration of the possible crystal orientations and phases of GaN grown by remote epitaxy. The blue phase is hexagonal GaN with the (0001) plane parallel to the underlying substrate surface. The red phase is cubic GaN with the (001) plane parallel to the underlying substrate surface. The green phase is hexagonal GaN grown on the (111) facets of the cubic crystal.

The comparison of the characteristics of the sample G22_GNL3150 with the sample GNL2998 can be seen in Table 3. The sample G22 is worse than the sample grown under standard conditions in every aspect.

Table 3: Comparison of the basic parameters of the previously discussed samples.

Sample	AFM roughness in nm [10x10] µm^2	FWHM in arcmin	Hexagonal inclusions	GaN layer thickness in nm
GNL2998	3.9	29.8	<1%	580
G22_GNL3150	N/A	57.6	80%	342

6.5 Optimization of the substrate temperature

A significant change was necessary to improve the layer quality. Even though other publications suggested the growth at lower temperatures[5,70–72], this work has shown that this is not possible for the growth of a metastable phase.

While the best conditions for the growth of cubic GaN are at a substrate temperature of 740°C, new works by Falco Meier[73] have shown that it is possible to grow cubic GaN at higher temperatures with only a slight reduction in crystal quality.

The increase of the substrate temperature will change the nucleation process drastically. As discussed previously, the nucleation probability is already low on the graphene monolayer. By increasing the substrate temperature, the evaporation rate is increased, and therefore, the nucleation probability is decreased. However, under the previous condition, we observed a high amount of h-GaN in the (0001) direction. This can only occur when nucleation happens without an interaction through the graphene monolayer. The structure of the underlying 3C-SiC substrate seems to have no influence on the nucleation under the colder conditions.

Therefore, a series of multiple samples were grown to find the maximum growth temperature. A sample series beginning at 830°C was started. Additionally, the samples were grown without a growth recipe at the beginning. The growth time was one hour. With each new sample, the substrate temperature was increased by 5°C. The highest possible temperature was 850°C. Above this value, it is not possible to nucleate GaN.

The SEM images of the five samples are shown in Figure 51. The most prominent feature of the images is the more homogenous nature of the layer grown at higher temperatures. The strong polycrystalline feature of the samples grown at lower temperatures has been significantly reduced. However, there are still differences between each layer. With

increasing temperature, the surface seems to get smoother. The best-looking surface is achieved with a substrate temperature of 845°C. Therefore, for the following samples, the substrate temperature of 845°C was chosen.

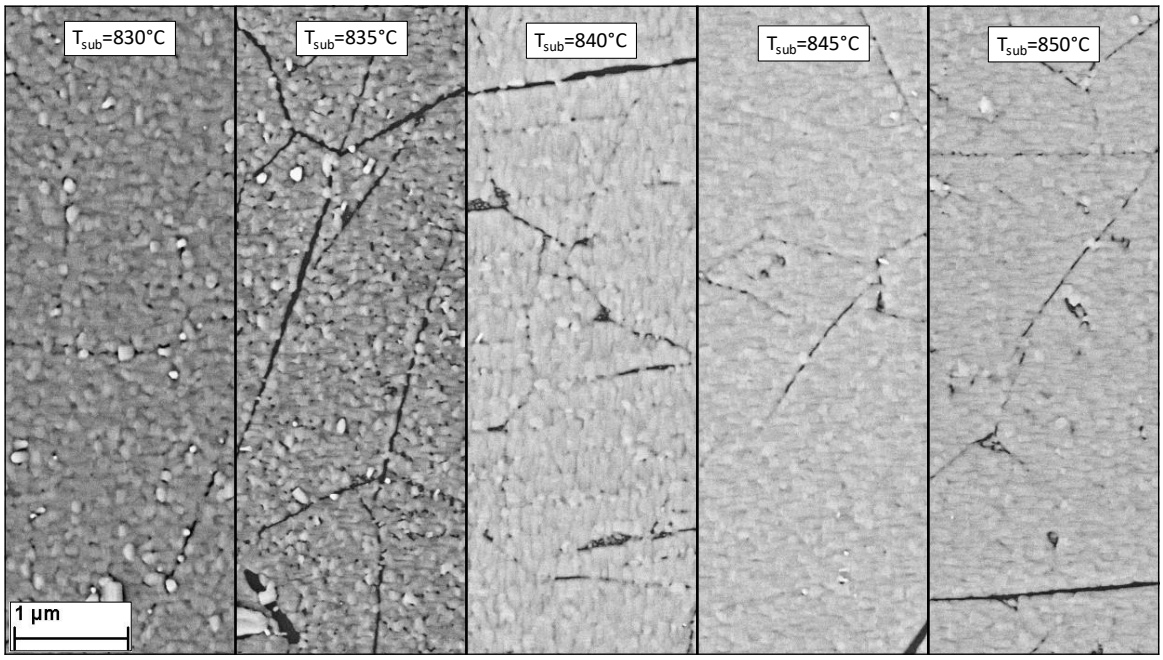

Figure 51: SEM images of the substrate temperature series. The substrate temperature varies from 830°C to 850°C.

By further investigation of the sample G38_GNL3168 (845°C), it can be observed that the highly polycrystalline nucleation along the domain boundaries of the graphene no longer occurs. In contrast, under these conditions, there seems to be no nucleation happening along the domain boundaries. Figure 52 shows the comparison between the layer of G38_GNL3168 and an SEM image of the graphene-covered substrate. The dimensions of the domain boundaries and the lines through the epitaxial layer have the same order of magnitude.

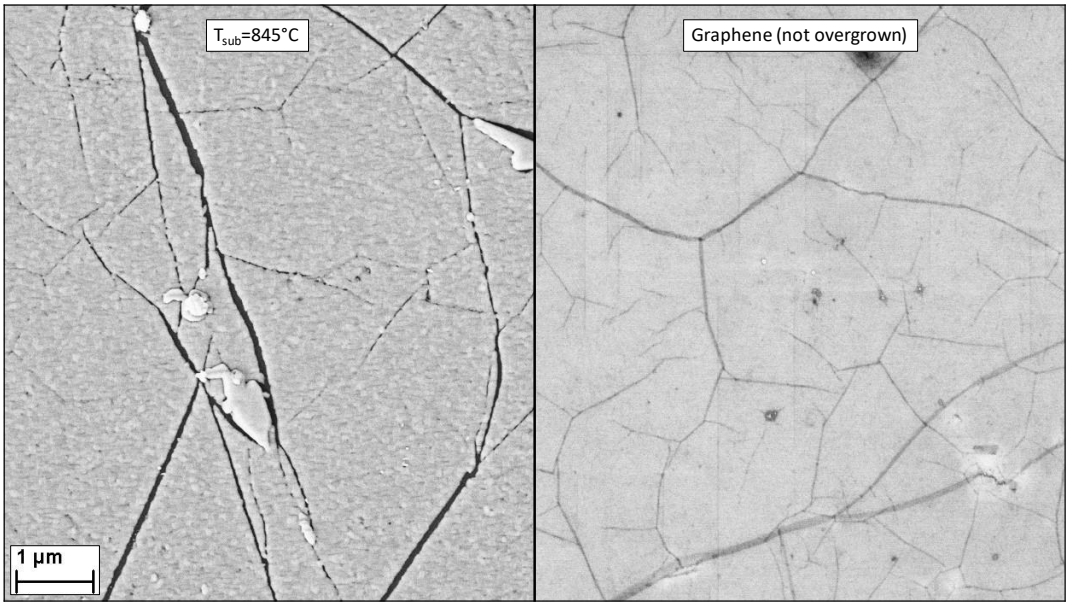

Figure 52: SEM image comparison of the sample G38 with the underlying graphene structure. The increased substrate temperature of 845°C prevents nucleation at the domain boundaries. Previously published in [66].

Thicker samples were grown to analyze the growth further at higher temperatures. The sample G38 is only 50 nm thick, which makes it challenging to characterize. Figure 53 shows the SEM images of two layers grown at 745°C with a thickness of a) 100 nm and b) 350 nm. These samples have been previously shown in Figure 47.

The direct comparison to the layers grown under colder conditions shows a significant improvement in roughness and a reduction in polycrystallinity. In Figure 53 d), the 250 nm thick GaN layer grown at 845°C is shown. Interestingly, with an increased growth time, the gaps along the domain boundaries are entirely overgrown. The lines of the thinner layer in Figure 53 c) are no longer visible. Additionally, AFM measurements confirm a roughness of 5 nm, which is close to the standard growth conditions, where a roughness of 3.9 nm can be achieved.

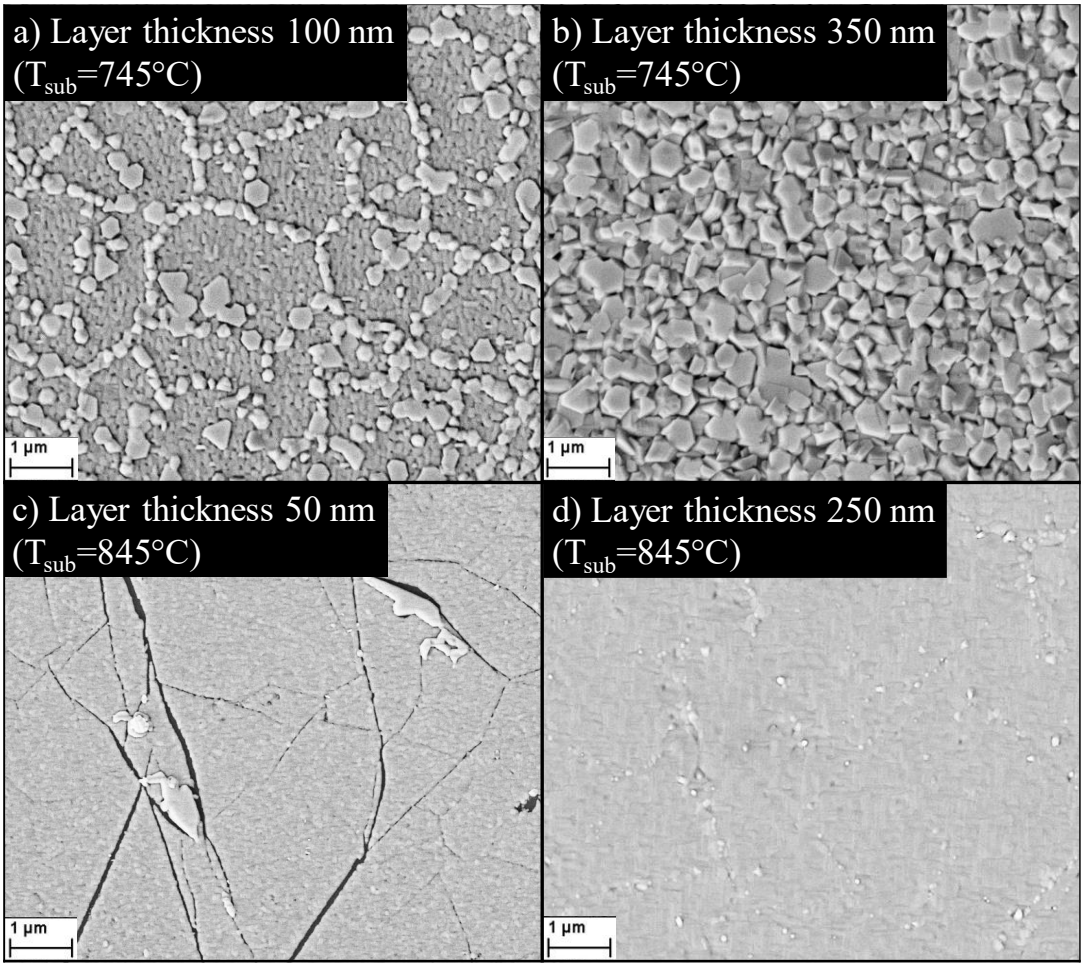

Figure 53: SEM images of the surface of several 3C-SiC samples covered with graphene and overgrown with GaN: a) GaN layer grown on top of a graphene layer (Tsub = 745 °C). b) Thicker GaN (Tsub = 745 °C). c) Thin GaN layer grown (Tsub = 845 °C). d) Thicker GaN layer (Tsub=845°C). Previously published in [66].

The improved surface roughness also results in a more intense RHEED pattern, see Figure 54. In comparison to Figure 44, the intensity and signal-to-noise ratio were significantly improved due to the smoother surface. The intensity of the line pattern was increased as well. However, compared to the ideal pattern of Figure 32, the lines are still more elliptical.

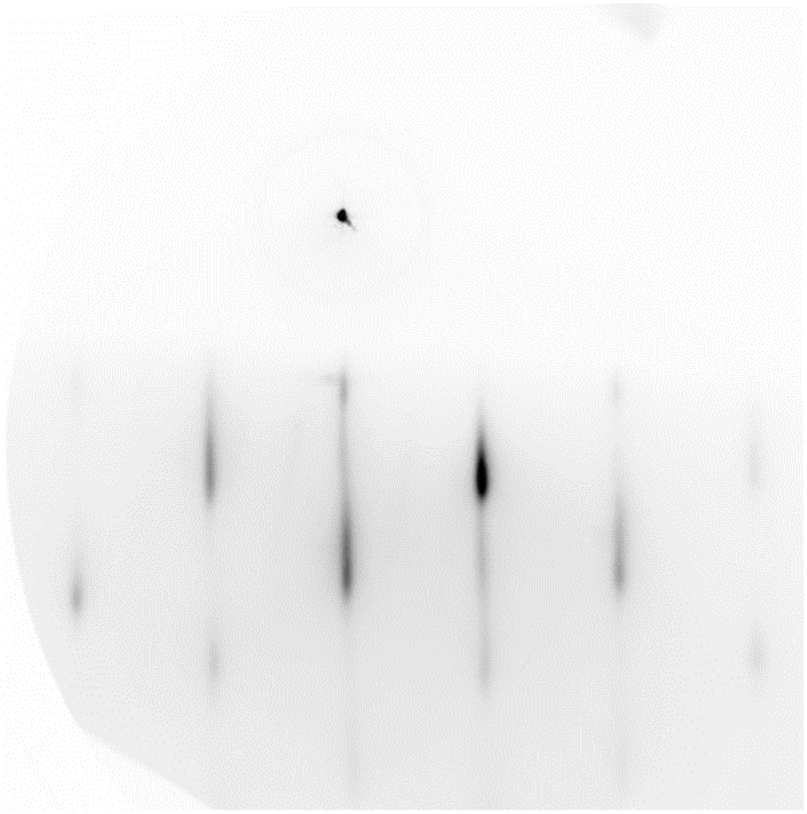

Figure 54: RHEED pattern of 250 nm thick sample G40_GNL3170 grown at a substrate temperature of 845°C. In comparison with Figure 44, the intensity is increased, indicating a smoother surface.

The HRXRD measurements show a significant shift of the intensity from the h-GaN (0002) reflection towards the (10-11) and (-1011) reflections (Figure 55). Especially the c-GaN (002) has become the most intense reflection. By comparing the intensities, it can be concluded that the hexagonal inclusions only amount to 40% of the total intensity. This is a significant reduction to the 80% hexagonal layer grown at lower temperatures (see Figure 49).

Furthermore, the intensity of the (0002) reflection was reduced by two orders of magnitude. This means that the majority of the nucleation at the higher temperature occurs in the cubic phase. However, it must be mentioned that a new problem arose. The majority of the hexagonal inclusions are now being formed on the (111) facets of the cubic crystal as stacking faults.

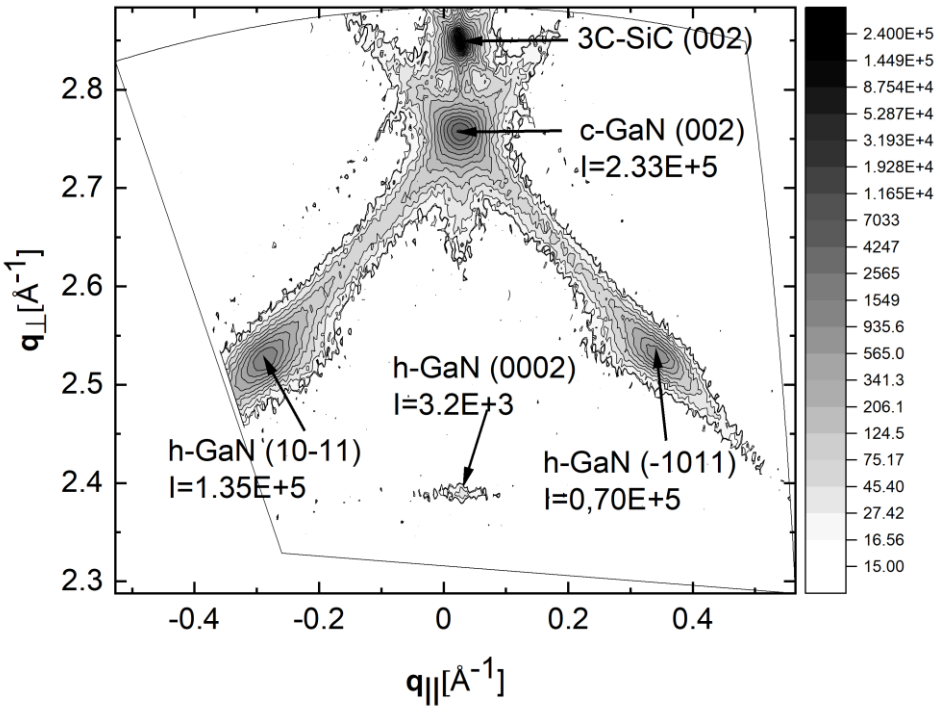

Figure 55: RSM of the (002) reflection of the 250 nm thick GaN layer grown on graphene (G40_GNL3170). The majority of the intensity of the hexagonal phase is located at the (10-11) and (-1011) reflection. The formation in the (0002) direction is reduced by two orders of magnitude in comparison to Figure 49. The comparison of the integral intensities determines the hexagonal inclusions at 40%. Previously published in[66].

These measurements indicated that the epitaxy at lower temperatures enhances the formation of the hexagonal (0001) phase. However, increasing the substrate temperature was beneficial for the formation of the cubic (001) phase. This phenomenon can be attributed to the enhanced evaporation rate and diffusion length. While this also reduces the nucleation rate, it encourages the adatoms to nucleate at energetically desirable positions above the dangling bonds of the underlying substrate. By orienting themselves along the dangling bonds, the epitaxial layer also takes the structure of the substrate.

This can be further demonstrated by the PL measurements. In Figure 56, the spectrum sample G40_GNL3170 is compared to the first sample, G5_GNL3118. While the total intensity has been drastically decreased, it is noticeable that the highest peak is now caused by the basal stacking fault (BSF)[54]. As described in chapter 2.7, a stacking fault is a planar defect that occurs when the stacking order changes in one direction. In this material system, a stacking fault between the hexagonal and cubic phases occurs in the

cubic (111) direction. With the highly increased intensity at the (10-11) and (-1011) reflection, the amount of stacking faults increased accordingly.

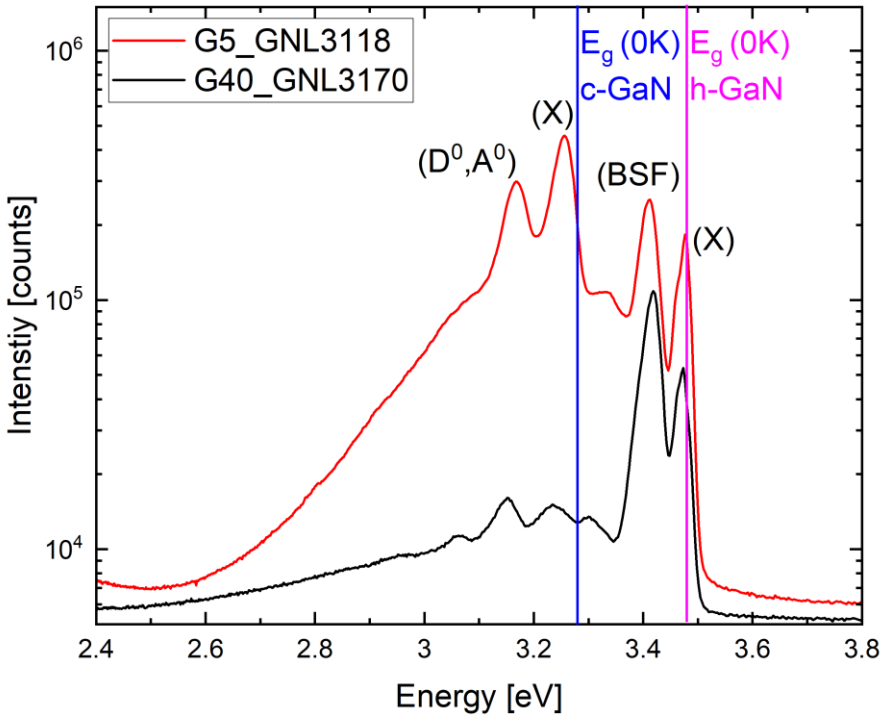

Figure 56: Comparison of the PL spectra of a sample grown at 740°C (G5_GNL3118) and a sample grown at 845°C (G40_GNL3170).

The comparison with the previously in chapter 6.4 discussed sample G22_GNL3150 shows a significant improvement in every aspect (Table 4). The AFM roughness is already comparable to the standard sample GNL2998. The FWHM of the rocking curve was further reduced, and the amount of hexagonal inclusions was halved to 40%.

Table 4: Comparison of the basic parameters of the previously discussed samples

Sample	AFM roughness in nm [10x10] µm^2	FWHM in arcmin	Hexagonal inclusions	GaN layer thickness in nm
GNL2998	3.9	29.8	<1%	580
G22_GNL3150	N/A	57.6	80%	342
G40_GNL3170	5	49.6	40%	220

6.6 Aluminum nitride buffer layer

While the increase in the substrate temperature reduced the amount of hexagonal inclusions, the current value is still significantly too high for device applications. Therefore, further optimizations are necessary. The main reason for the improved quality is the increased influence of the underlying dangling bonds of the substrate. It is necessary to increase this interaction further to increase the layer quality. Since the length of the dangling bonds depends on the chemical polarity of the atomic bonds, a change of the substrate material could be beneficial.

The length of the dangling bonds depends on the chemical polarity of the atomic bonds in the substrate. While the 3C-SiC is still the best possible substrate material, it is possible to grow a small buffer layer underneath the graphene monolayer. The difference in the electronegativity between a silicon and a carbon atom of a SiC bond is 0.76[74]. This value is rather small in comparison to more polarized bonds. Since carbon and silicon are both part of the fourth group in the periodic table, their electronegativity values are not significantly different.

One possibility would be to grow a thin c-GaN buffer layer. The ionicity of the GaN bonds is higher than SiC and should, therefore, increase the length of the dangling bonds. However, GaN is not the best possible material. Because of the high lattice mismatch, it is not possible to grow a smooth GaN buffer layer. While the 3C-SiC substrate has a root mean square roughness of 0.35 nm, it was not possible to create a c-GaN layer with a similar roughness. Multiple thin GaN buffer layers were grown under varying growth conditions and durations. However, the best layers had a roughness of at least 1 nm.

For the best growth conditions during the remote epitaxy, using an atomically smooth substrate is especially important to ensure perfect contact between the substrate and the graphene monolayer. Because of this, GaN cannot be used as a buffer layer material.

The material of choice for this is cubic aluminum nitride. With a lattice constant of 4.373 Å[17], it is the closest to 3C-SiC with 4.3596 Å. The lattice mismatch is only 0.3% and allows the growth of atomically thin buffer layers, which are pseudomorph. Furthermore, the difference in the electronegativity has a value of 1.45 [74], which is higher than that of GaN. In comparison, the value for SiC is 0.76 [74].

The used PAMBE system already contains an aluminum cell and is therefore also able to grow aluminum nitride layers. The buffer layer growth step will extend the sample preparation. Figure 57 shows a standard sample structure, including the c-AlN buffer layer. Different tests have shown that the best properties could be achieved by growing a 10 nm thin c-AlN buffer layer.

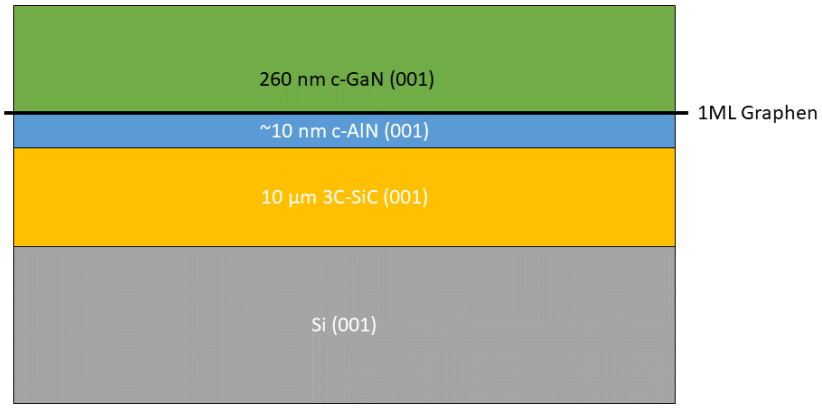

Figure 57: Sample structure with 10 nm thick c-AlN buffer layer underneath the graphene monolayer

The c-AlN were grown at a substrate temperature of 740°C and an Al flux of 1.4 x 10^{14} atoms $[cm^2s]^{-1}$. The parameters for the nitrogen source were identical to the growth of GaN with 260 W and 0.5 sccm. The thickness of 10 nm has been confirmed by x-ray reflection measurements. Within this thickness, the layer should be grown pseudomorphically and, therefore, should have a low defect density.

The RHEED pattern of one of these c-AlN buffer layers is shown in Figure 58. The pattern consists of streaks. This confirms a very smooth surface, which can be confirmed by AFM measurements. The AFM image in b) shows a roughness of 0.5 nm. While it isn't as perfect as the 0.35 nm of the 3C-SiC, the value is still small to ensure the contact between substrate and graphene.

After the growth of the c-AlN buffer layer, the samples were again covered by a monolayer of graphene according to the previously described transfer and cleaning procedure. Thereafter, the graphene-covered c-AlN buffer layer was transferred into the MBE chamber and overgrown with GaN at a substrate temperature of 845°C.

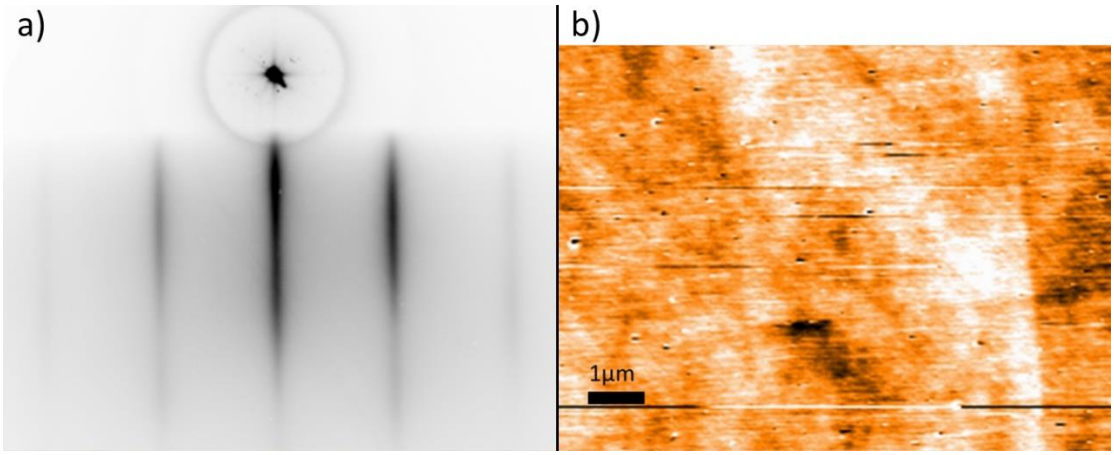

Figure 58: a) RHEED-pattern and b) AFM-image of a c-AlN buffer layer. The roughness of the AFM measurement in a 10 µm by 10 µm area is 0.5 nm.

6.7 HRXRD analysis

Additionally, the new sample grown on the c-AlN buffer layer was also characterized by HRXRD measurements. The reciprocal space map of the (002) reflection of the GaN layer grown with the c-AlN buffer layer is shown in Figure 59 c). The previously shown RSMs of the samples grown without the c-AlN layer at 745°C (a) and 845°C (b) are included in the figure to compare them with each other. The RSM in c) indicates a further reduction of the hexagonal inclusions to about 23%. This is another improvement compared to the 40% achieved by the optimized substrate temperature (b). It can be concluded that the buffer layer had the anticipated effect.

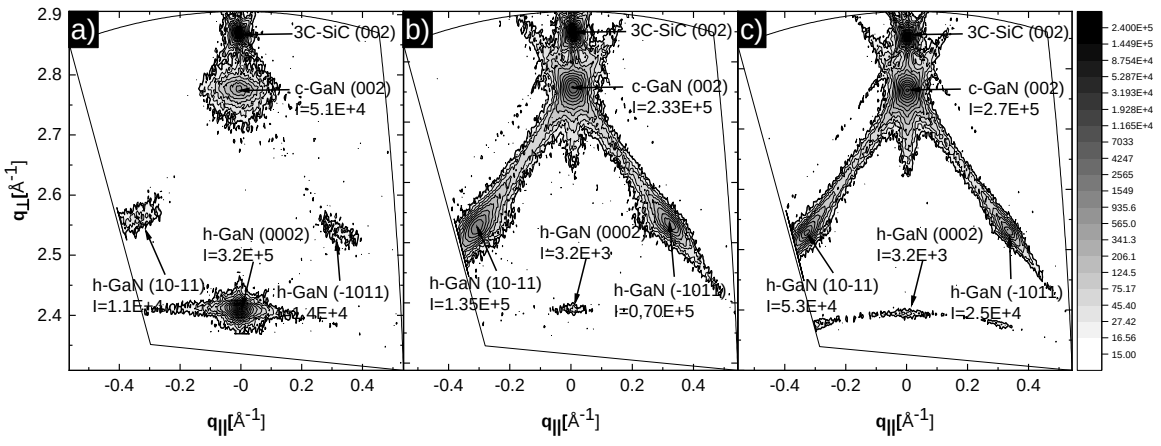

Figure 59: Reciprocal space maps containing the cubic (002) and the hexagonal (0002),(10-11), and (-1011) reflections of three samples grown on a graphene monolayer: a) 350 nm thick GaN grown on a 3C-SiC/Si substrate at Tsub=745°C (G22_GNL3150) b) 260 nm thick GaN grown on a 3C-SiC/Si substrate at Tsub=840°C (G40_GNL3170) c) 300 nm thick GaN grown on a thin c-AlN buffer layer at Tsub=845°C (G63_GNL3269). Previously published in[66].

Figure 59 perfectly visualizes the effects of the advancements caused by the optimization of the growth process. The first RSM (a) shows one of the first samples grown at a lower temperature of 745°C. By raising the substrate temperature to 845°C, the hexagonal inclusions were reduced from 80% to 40%. This was the most significant change because it not only reduced the hexagonal inclusions but also changed the crystal orientation of these inclusions. At a lower temperature, the majority of the nucleation occurs directly in the hexagonal (0002) orientation. By increasing the temperature, the intensity of the (0002) reflection was reduced by two orders of magnitude. However, it also increased the (10-11) and (-1011) reflections.

These reflections are caused by the stacking faults on the (111) facets of the cubic crystal. They are a result of the three-dimensional growth at the beginning. The formation of the islands will always contain (111) facets. By introducing the c-AlN buffer layer, it was possible to reduce the hexagonal inclusions further. The third figure shows an additional reduction of the hexagonal reflections.

The improvement of the layer quality over the different changes in the growth procedure can be seen in Table 5. With the introduction of the c-AlN buffer layer, the surface roughness was further decreased to 4 nm (G64_GNL3270) and is now comparable to the sample grown without graphene (GNL2998). The FWHM of the rocking curve measurements has a value of 33.0 arcmin, which is also close to the value of 29.8 of the reference sample. However, the hexagonal inclusion has a value of 23%, which is still too high for device applications. It is important to mention that the FWHM can only be compared if the samples have a comparable layer thickness. Therefore, a comparison is only possible between the reference sample GNL2998 and the sample G64_GNL3270.

Table 5: Comparison of the basic parameters of the previously discussed samples

Sample	AFM roughness in nm [10x10] μm^2	FWHM in arcmin	Hexagonal inclusions	GaN layer thickness in nm
GNL2998	3.9	29.8	<1%	580
G22_GNL3150	N/A	57.6	80%	342
G40_GNL3170	5.0	49.6	40%	220
G63_GNL3269	2.0	45.2	21%	260
G64_GNL3270	4.0	33.0	23%	590

6.8 Remote epitaxy on c-AlN buffer layer

A sample series with different growth durations was created to further investigate the growth with an underlying c-AlN buffer layer. The growth conditions were identical to the previously grown samples at 845°C. The only difference is the growth time, which varies from 5 minutes to 6 hours. The results are shown in Figure 60. The Figure contains an SEM image of the surface and the RHEED pattern for every sample at the end of the growth process. Interestingly, the images show a kind of delayed growth process. After the first 5 minutes, the surface is still uncovered. It takes up to 15 minutes for the first nucleation islands to form. However, these spots only cover less than 1% of the total surface area.

After an additional 15 minutes, the GaN begins to spread over the entire surface. However, the layer is not a closed film yet. This is also verified by the fact that the RHEED pattern consists predominantly of dots. This pattern indicated a three-dimensional surface morphology [41]. In the following 30 minutes, the epitaxial layer begins to close the gaps and form a smoother surface. The change is also evident through the transformation of the RHEED pattern towards a streak pattern, which indicates a smooth 2D surface [41]. A further increase in the growth duration improves the layer quality even more. The lines of the RHEED pattern gain in intensity, and the SEM images show a more homogenous and smoother surface.

With these observations, one can suspect that the growth process resembles a pin-hole epitaxy process rather than a remote epitaxy. Since the graphene will be in direct contact with the nitrogen plasma during the first 15 to 30 minutes, the nitrogen ions can interact with the graphene monolayer during this time and be incorporated or induce holes in the layer[75]. This phenomenon would explain the sudden nucleation that occurs after a time delay. Pin-hole epitaxy does not necessarily have a negative effect since it has many of the same benefits as the remote epitaxy process. For example, it can still be possible to perform a lift-off process if the number and size of the holes are not too big[35]. The characteristics of pin-hole epitaxy have been described in more detail in Chapter 2.8. Transmission electron microscopy measurements are planned for future works to verify these assumptions.

Small defect-free areas were investigated using AFM measurement to validate the enhanced surface roughness. The measurements confirm an RMS roughness of 3 nm for

the 260 nm sample (SEM see Figure 60 e) and 4 nm for the 580 nm sample (SEM see Figure 60 f). This is comparable to the roughness achievable under standard conditions.

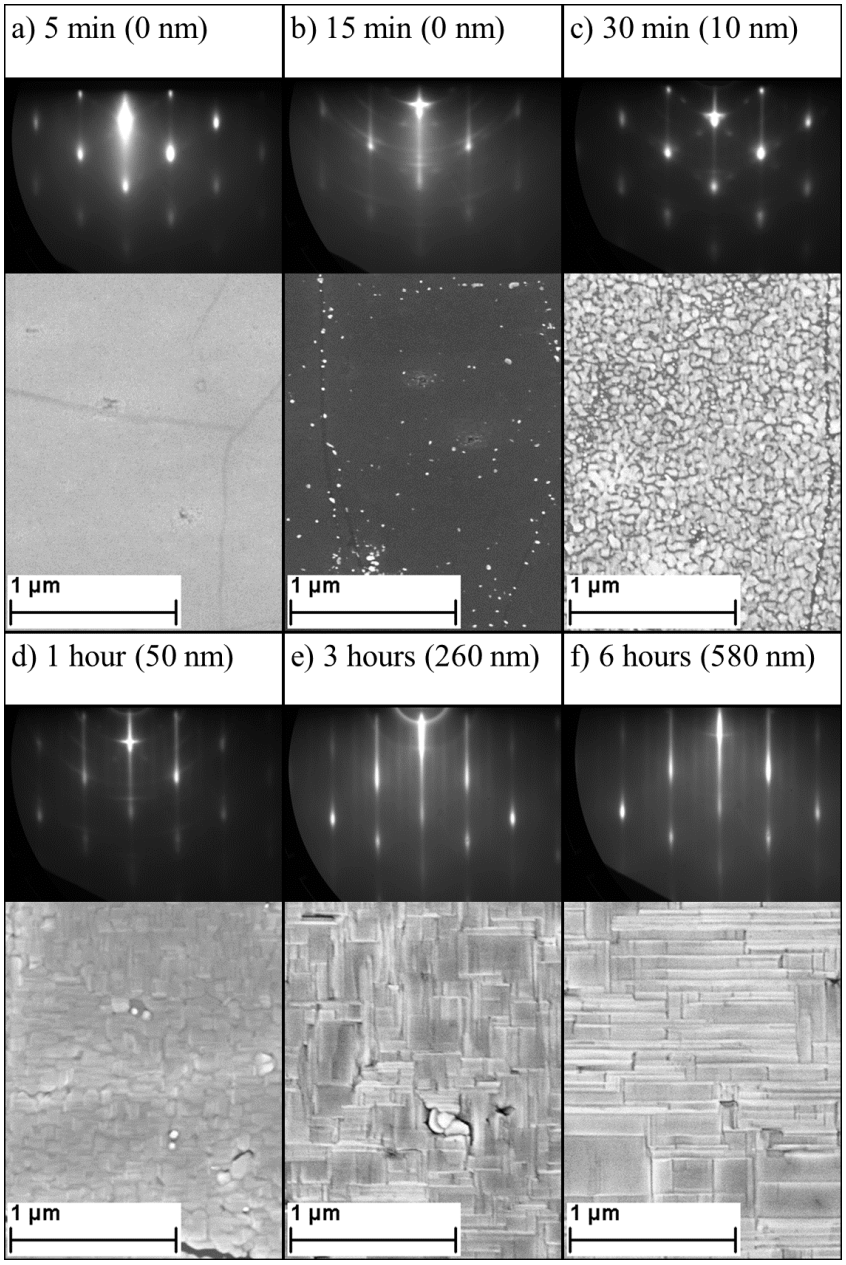

Figure 60: RHEED pattern and SEM images of a sample series with different growth durations. The samples were all grown on a c-AlN buffer layer with a substrate temperature of 845°C. Previously published in[66].

Despite this, the samples still contain a high number of defects on the surface. As mentioned previously, the characteristics of the transfer graphene include different kinds of defects. The first one is the domain boundaries. Under the given growth conditions, growth along the domain boundaries is prevented. Figure 61 a) shows the gap in the film

at the domain boundaries in a 50 nm thick GaN layer. It takes up to 100 nm for these gaps to begin to close. An example of an overgrown and closed domain boundary is shown in Figure 61 c). The gap remains underneath, and it is only closed from the sides.

Additionally, the graphene layer contains point defects. These are holes in the film or other defects that occurred during the CVD process. Furthermore, the graphene monolayer will also be damaged during the transfer process by dirt particles or other means. These point defects result in the formation of small polycrystalline inclusions. They are still visible in thicker films, as shown in Figure 61 b). The cross-section image in Figure 61 d) shows the polycrystalline nature of these defects. The concentration of these defect points is approximately 10^7 cm^{-2}.

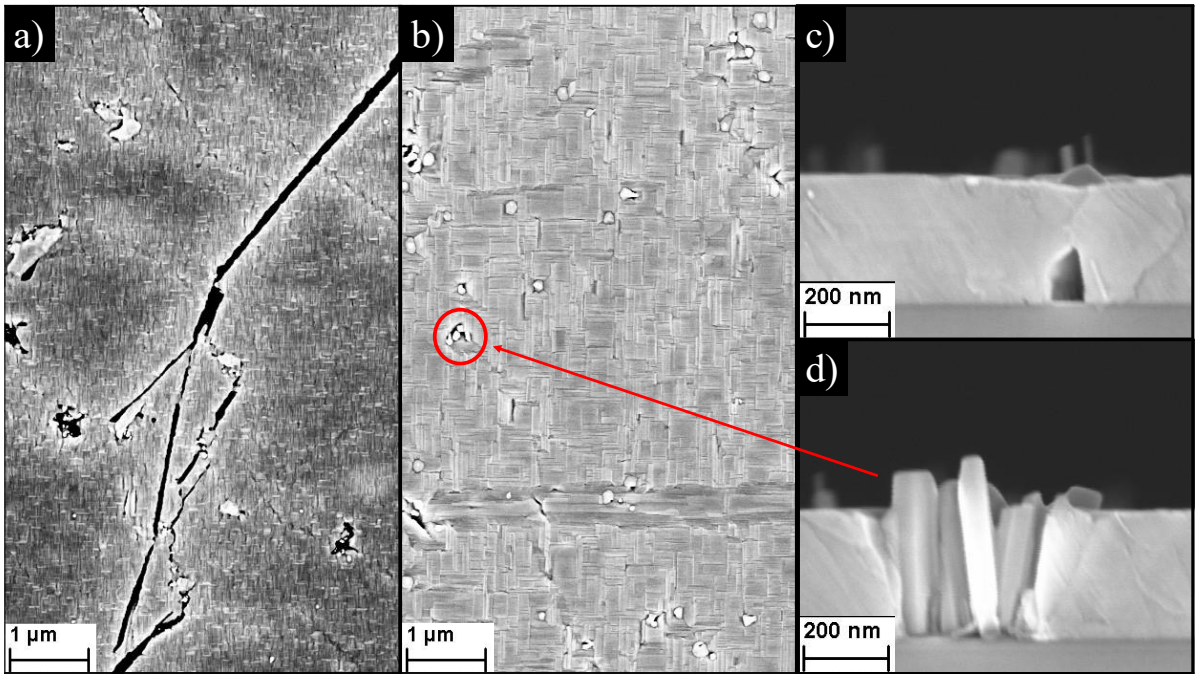

Figure 61: SEM-images of GaN layers grown on top of a graphene-covered AlN-buffer layer: a) 50 nm thick GaN layer with visible gaps caused by the graphene domain boundaries b) 300 nm thick GaN layer c) side view of an overgrown domain boundary d) side view of a polycrystalline defect indicated exemplarily by the red circle in b). Previously published in[66].

6.9 Electron backscatter diffraction

Another method to analyze these influences of the graphene defects on the epitaxial layer is electron backscatter diffraction. This method allows us to distinguish between the different cubic and hexagonal phases on a microscopic level. EBSD measurements were performed by Olga Augst of the group of Prof. Jürgen Christen from Otto von Guericke University Magdeburg. The result of an EBSD measurement of the sample G46_GNL3176

is shown in Figure 62. The left side shows the standard SEM image of the sample surface. On the right side is the result of the EBSD measurement for the same area shown. The cubic parts of the layer are colored red, and the hexagonal parts are marked green. By comparing the SEM image to the EBSD measurement, one can see that the majority of the hexagonal phase is located along the defects of the graphene. This is the case for both defects. When we look at the single white dots in the SEM image, we can see that all these points are marked as green in the EBSD measurement. Additionally, the majority of the green areas are located along the walls of the domain boundaries.

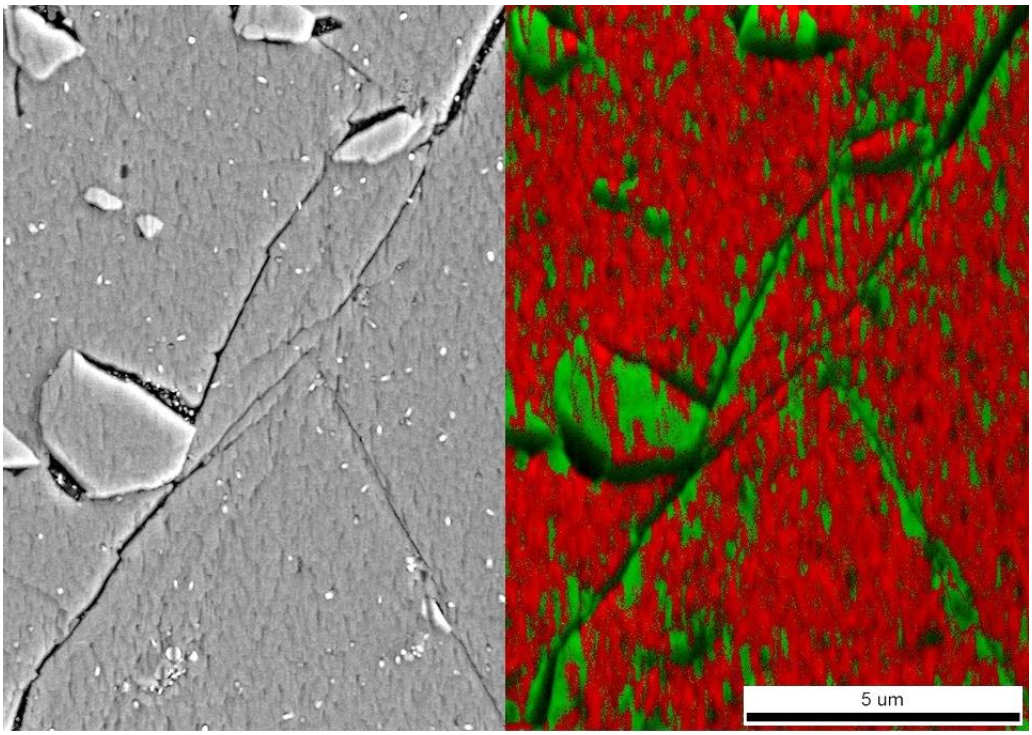

Figure 62: (left) SEM image of the remote epitaxial grown cubic GaN layer (G46_GNL3176). (right) Color-coded EBSD measurement of the same area. The cubic phase is marked in red, and the hexagonal phase is green. The majority of the hexagonal inclusions are located at the defects of the graphene monolayer. This indicates that the defects, in particular the domain boundaries, enhance the formation of the hexagonal phase.

These observations indicate that the main obstacle in the way to a high-quality remote epitaxial layer of cubic GaN is the quality of the graphene monolayer. An alternative method to the CVD-transfer process that eliminates the need for the transfer step in graphene production is needed, as this step often introduces these undesired defects. One noteworthy alternative, which holds promising potential for future research, involves the thermal breakdown of SiC as a new method. Looking at recent studies done by Ouerghi et al. [76] shows that using thermal decomposition is indeed a viable route also for 3C-SiC.

In more detail, this method requires heating the SiC to an intense temperature of around 1300°C in a controlled vacuum. Such conditions encourage the surface silicon atoms to evaporate. In their absence, the carbon atoms left behind naturally form a graphene layer. Theoretically, this technique has the capability of producing high-quality graphene, perhaps the best we can obtain.

However, it is worth noting that this high-quality production process has its limitations. Primarily, it prevents the option to use the c-AlN buffer layer. Previous experiments have shown that this AlN layer plays an important role in enhancing the overall quality of the resulting remote epitaxially grown c-GaN layer.

Seeking other alternatives, researchers have also demonstrated the possibility of growing a graphene layer with CVD on any desired substrate material[38,39]. By adapting this process for the growth on c-AlN, it could be possible to achieve higher-quality graphene monolayers without the defects caused by the transfer process. However, in comparison, this method produces graphene of lower quality than thermal decomposition. The main benefit is the option to still use the c-AlN buffer layer to reduce the hexagonal inclusions.

6.10 Photoluminescence spectroscopy

Besides the HRXRD measurements, PL measurements can also be performed to gain insights into the phase compositions of a material. This is due to the fact that variances in the crystal phase influence the band gap energy of the material. For example, the wurtzite GaN at 0 K has a bandgap energy of 3.47 eV [59]. This energy level deviates from the bandgap energy of zinc-blende GaN, which is slightly lower at 3.293 eV[22]. As a consequence of these deviations in bandgap energies, differences in luminescence can be observed and attributed to the varying phases.

One key detail to consider when employing PL measurements is the penetration depth of the laser used. The penetration depth is limited to approximately 100 nm[22]. Hence, the data retrieved from PL measurements predominantly reflects information concerning the top layers of the investigated sample.

Delving deeper into the results, Figure 63 depicts the PL spectra of three distinct samples. Each of these samples showcases a different thickness. Not including the varying growth durations, all samples were grown under identical conditions on a graphene/c-AlN substrate. When analyzed and compared with the HRXRD measurements, the spectral

data reveals a high intensity for the cubic phase. The peak with the highest intensity can be assigned to the cubic excitonic peak (X). Notably, as the film thickness increases, there is a discernible rise in the cubic-to-hexagonal intensity ratio. Taking the laser penetration depth into consideration, one can conclude that the hexagonal phase predominantly forms during the initial stages of growth. The hexagonal phase predominantly forms during the nucleation stage to be more specific. This observation aligns with what is depicted in Figure 60.

Given that the growth at the nucleation phase is three-dimensional, there is a higher potential for nucleation to take place on the (111) facets. Consequently, this enhances the likelihood of hexagonal inclusions to form. This interpretation is further supported for by the high amount of basal stacking faults (BSF) [54]. The corresponding peak can be seen at an energy of 3.42 eV.

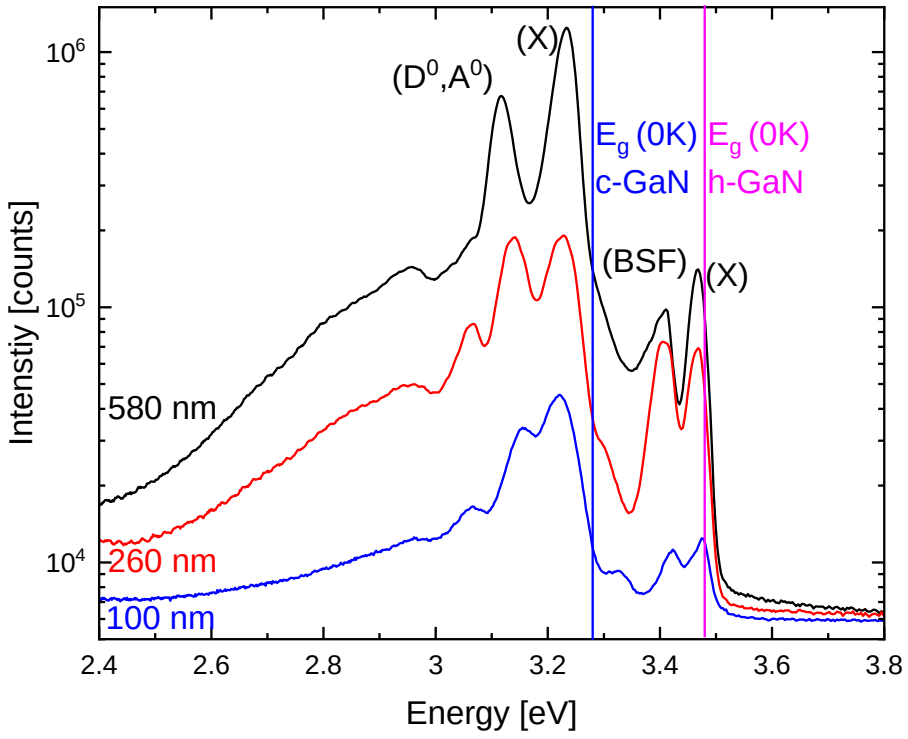

Figure 63: Photoluminescence spectra of three GaN layers grown on an AlN buffer layer with different thicknesses. The measurements were performed at 13 K. The peaks correspond to the donor-acceptor transition (D^0,A^0), the exciton transition (X), and the basal stacking fault (BSF). Previously published in[66].

7. Double AlN buffer

While the introduction of the c-AlN buffer layer showed a further improvement in the layer quality, the amounts of hexagonal inclusions are still too high for device applications. As a potential further development of this method, a second c-AlN buffer layer was investigated. The idea for this is to grow an additional c-AlN over the graphene monolayer. In that case, the graphene would be in between the two c-AlN layers. In an ideal case, the second layer would grow without the influence of the lattice mismatch and form a relaxed buffer layer, which can be overgrown by a c-GaN layer. The possible structure is shown in Figure 64.

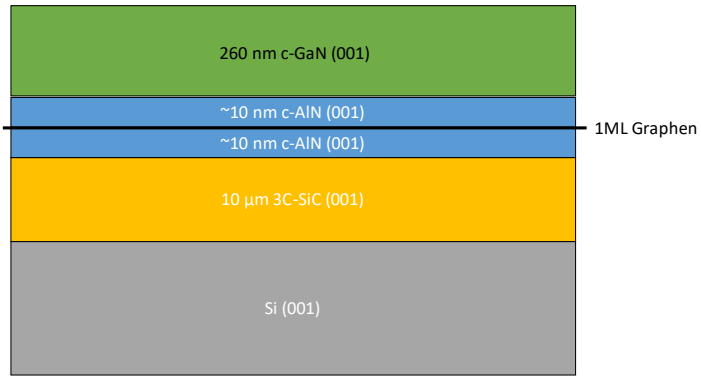

Figure 64: Sample structure with two 10 nm thick c-AlN buffer layers above and underneath the graphene monolayer

However, the attempts to grow a homogenous thin c-AlN layer on top of the graphene have failed. One of the resulting samples is shown in the SEM image of Figure 65. As can be seen, the nucleation of the c-AlN layer is as complicated as that of the c-GaN layer. It is not possible to form a homogenous, smooth layer. Instead, the result is a polycrystalline film that enhances the formation of defects and stacking faults. Different growth conditions were tested. The substrate temperature was varied from 750°C to 900°C. However, it was not possible to grow a monocrystalline layer.

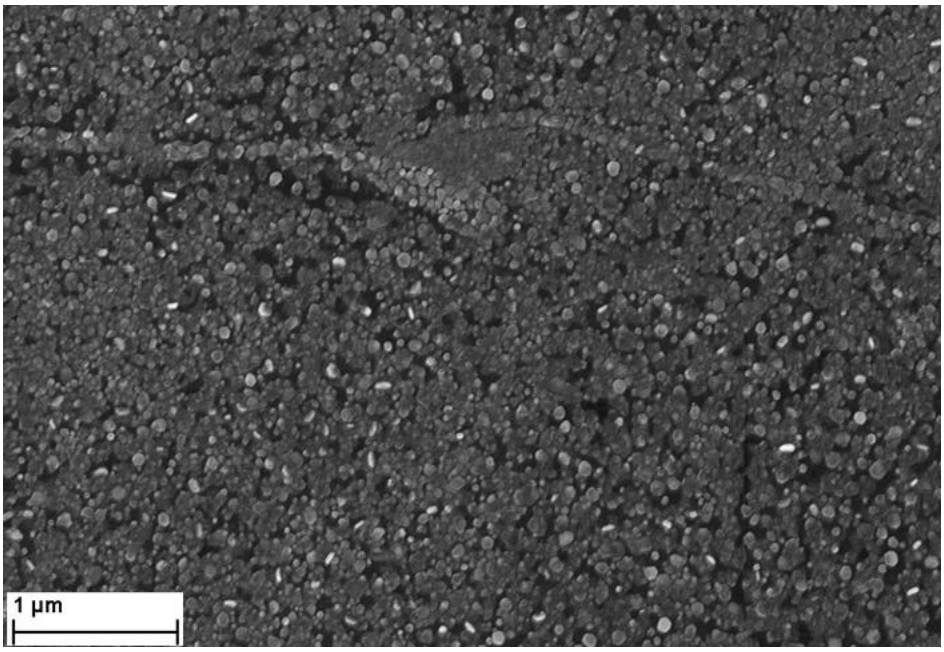

Figure 65: SEM-image of the c-AlN grown on a graphene/c-AlN substrate. The surface is completely polycrystalline and consists of 3D islands.

8. Lift-off

One of the main advantages of the remote epitaxy growth process is the possibility to perform a lift-off process. This can be beneficial for different applications. Especially for the nitrides, different kinds of lift-off processes are difficult to perform due to the high chemical resistance[7]. While it is possible to perform a chemical lift-off process based on the wet etching of a sacrificial layer, it requires the introduction of a new non-nitride-based material layer. For the hexagonal nitrides, for example, a gallium oxide layer can be used[77,78]. This brings some disadvantages as it requires the additional growth of a lattice mismatch layer that can introduce more defects into the epilayer. Additionally, it requires an oxygen source in the used epitaxy system.

Besides the chemical etching of a sacrificial layer, it is also possible to remove the GaN layer from sapphire substrates with a laser lift-off process[79]. However, it is only possible for GaN layers grown on transparent substrates. Therefore, it is not possible to perform a laser lift-off for c-GaN layers grown on 3C-SiC/Si substrates.

Considering the disadvantages of these lift-off processes, the exfoliation process of the remote epitaxially grown layer seems to be beneficial. Multiple works[5,8–10] have reported on the successful transfer of remote epitaxially grown GaN layers and devices. Furthermore, the process used did not damage the graphene film, and it was possible to reuse the substrate.

Multiple tests were performed to try performing a lift-off process with the cubic GaN samples grown during this work. However, it was not possible to remove the remote epitaxial layer from the substrate for the monocrystalline layers. It was only possible to perform this for polycrystalline samples.

Figure 66 shows pictures taken during the attempted lift-off process of the sample G76_GNL3339. An adhesive tape was pressed to the surface of the sample. The tape was carefully pressed to the surface to ensure maximum contact between the tape and the GaN layer. Afterward, it was pulled from the sample, and the majority of the GaN layer was also removed.

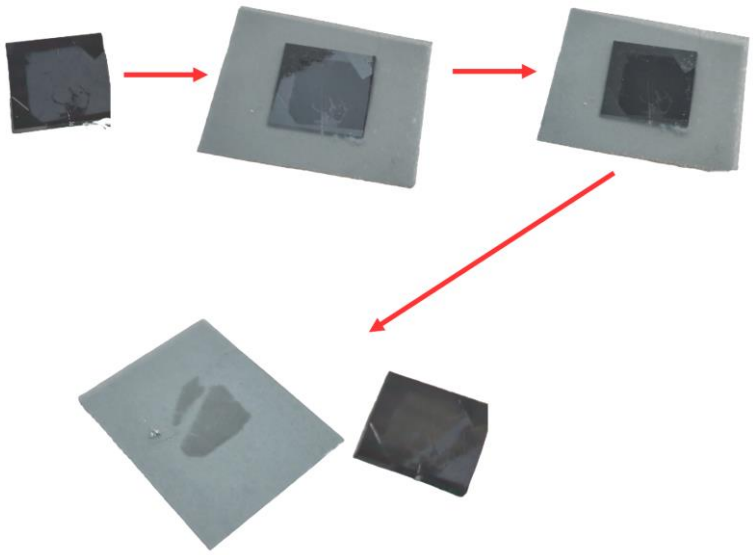

Figure 66: Pictures taken during the attempted lift-off process. The GaN sample was covered with a tape, and the tape was pressed evenly over the whole surface. By tearing the tape off again, a large amount of the polycrystalline GaN layer was removed from the substrate. However, this process was only possible for polycrystalline samples.

The used sample is a polycrystalline sample. The SEM image shows the layer before and after the lift-off. The image after the lift-off was taken along the lines of the remaining GaN. It can be seen that the GaN was removed completely, and the Graphene remains on the surface.

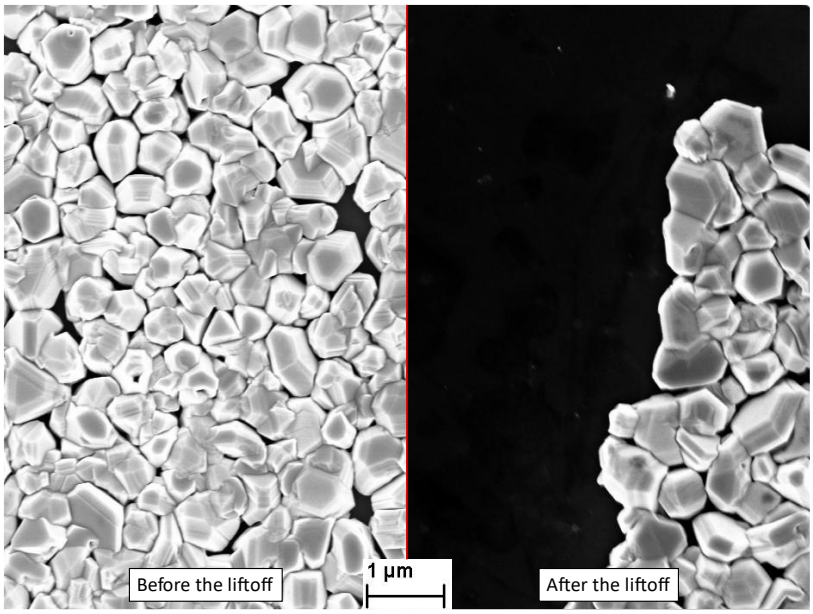

Figure 67: SEM image of the sample before and after the lift-off. The image after the lift-off was taken along the edge of the remaining GaN.

Additional tests were performed to apply the process also for monocrystalline layers. Unfortunately, it was not possible to remove the layer from the substrate. We assume that this is due to the many defects in the graphene layer. Tiny holes that are throughout the monolayer result in direct connections between the GaN layer and the substrate. This effect is also discussed in the work of Han et al.[80]. They investigated the exfoliation of h-GaN on Graphene and observed that the MOCVD growth process could damage the graphene film. The existence of these tiny holes allowed the epitaxial film to form covalent bonds with the substrate. Due to these connections, it was no longer possible to exfoliate the GaN layer from the substrate.

While the process in the MBE chamber is fundamentally different from the MOCVD process, the exposure of the graphene film to the nitrogen plasma could also damage the film and create holes[75,81]. Additionally, the graphene layer gets wrinkled and torn during the transfer process, which can also introduce new holes[82]. The latter is expected to be the main obstacle to the lift-off process. The plasma-induced holes are expected to be much smaller than the mechanically caused holes by the transfer process.

To discuss this effect in detail, cross-section TEM images of the interface would be necessary, which are planned in future works. As the previous SEM images have shown, the quality of the transfer graphene is not good enough to ensure a hole-free layer. Therefore, the best possible step to increase the probability of exfoliation is to use a different kind of graphene synthetization. The possible solutions were discussed at the end of chapter 6.9.

9. Conclusion

In summary, this thesis reports on adapting the remote epitaxy process to grow the meta-stable zincblende GaN. The 3C-SiC/Si (001) substrates were covered with a graphene monolayer using a transfer graphene process. A thermal cleaning process was developed to remove the residues from the photoresists required for the transfer. For this, the graphene-covered substrate samples were heated to 900°C in a vacuum chamber.

Different growth conditions were investigated to optimize the layer quality. In contrast to previous works on remote epitaxy for other materials, it was observed that performing the growth at an increased substrate temperature rather than at a lower temperature is beneficial. This is because the formation of the undesired stable hexagonal phase is enhanced at lower temperatures. The higher substrate temperature of 840°C reduced the hexagonal inclusions from 80% to 40%. Further improvements were achieved by introducing an additional c-AlN buffer layer between the 3C-SiC/Si (001) substrate and the graphene monolayer. The higher polarity of the AlN bonds enhanced the interactions of the adatoms with the underlying substrate. This step resulted in a further decrease of the hexagonal inclusions to 23%.

The nucleation process was further investigated by characterizing samples grown with varying growth durations. These experiments revealed that the nucleation occurs after a time delay of 15 to 30 minutes. Since the graphene is in direct contact with the nitrogen plasma during this time, the nitrogen ions may create holes in the graphene layer. This would result in a change from an actual remote epitaxy process towards pin-hole epitaxy. The change is not necessarily negative since pin-hole epitaxy has comparable benefits. For example, it will also reduce the influence of the lattice mismatch while ensuring an alignment with the substrate orientations. However, it can become more difficult to perform a lift-off process depending on the size and number of induced holes. To verify this assumption, transmission electron measurements are planned for future works.

Further characterizations showed that the rocking curve FWHM and AFM roughness of the samples grown on the c-AlN buffer were nearly the same level as those grown without the remote epitaxy. However, besides the still high amount of hexagonal inclusions, the layer contains defects caused by the quality of the transfer graphene used. SEM images have shown that the domain boundaries and other graphene defects also introduce

defects in the GaN layers. EBSD measurements have also shown that the majority of the hexagonal inclusions are located along these defects.

Additionally, multiple attempts were made to perform a lift-of process with the grown samples. However, it was only possible to detach the polycrystalline layers from the substrate. The monocrystalline layers were impossible to remove from the graphene layer. This is expected to be caused by the many hole defects in the transfer graphene layer.

In summary, the used transfer graphene is the main obstacle that currently prevents further improvements of the layer quality. For these improvements, it will be necessary to use a different kind of graphene synthetization. Besides thermal evaporation of the Si on top of the 3C-SiC, the most promising would be to use a CVD process to create the graphene monolayer directly on top of a c-AlN buffer layer to be still able to use the benefits of the higher polarization. With these changes, a further improvement in the layer quality can be expected. It potentially allows the growth of c-GaN layers of similar or better quality than under standard conditions. Additionally, with fewer and smaller defects in the graphene monolayer, it could become possible to perform a lift-off process, which would allow for new applications of c-GaN.

References

[1] S. Strite, *Journal of Vacuum Science & Technology B: Microelectronics and Nanometer Structures*. **1992**, *10* (4), 1237. https://doi.org/10.1116/1.585897.

[2] B. J. Baliga, *Semicond Sci Technol*. **2013**, *28* (7), 074011. https://doi.org/10.1088/0268-1242/28/7/074011.

[3] S. Nakamura, M. R. Krames, *Proceedings of the IEEE*. **2013**, *101* (10), 2211–2220. https://doi.org/10.1109/JPROC.2013.2274929.

[4] T. Journot, H. Okuno, N. Mollard, A. Michon, R. Dagher, P. Gergaud, J. Dijon, A. v Kolobov, B. Hyot, *Nanotechnology*. **2019**, *30* (50), 505603. https://doi.org/10.1088/1361-6528/ab4501.

[5] J. Kim, C. Bayram, H. Park, C.-W. Cheng, C. Dimitrakopoulos, J. A. Ott, K. B. Reuter, S. W. Bedell, D. K. Sadana, *Nat Commun*. **2014**, *5* (1), 4836. https://doi.org/10.1038/ncomms5836.

[6] S.-H. Bae, K. Lu, Y. Han, S. Kim, K. Qiao, C. Choi, Y. Nie, H. Kim, H. S. Kum, P. Chen, et al., *Nat Nanotechnol*. **2020**, *15* (4), 272–276. https://doi.org/10.1038/s41565-020-0633-5.

[7] C. Youtsey, R. McCarthy, P. Fay, in Semiconductors and Semimetals, Elsevier **2019**. https://doi.org/10.1016/bs.semsem.2019.08.003

[8] H. Kum, D. Lee, W. Kong, H. Kim, Y. Park, Y. Kim, Y. Baek, S.-H. Bae, K. Lee, J. Kim, *Nat Electron*. **2019**, *2* (10), 439–450. https://doi.org/10.1038/s41928-019-0314-2.

[9] J. Jeong, Q. Wang, J. Cha, D. K. Jin, D. H. Shin, S. Kwon, B. K. Kang, J. H. Jang, W. S. Yang, Y. S. Choi, et al., *Sci Adv*. **2020**, *6* (23). https://doi.org/10.1126/sciadv.aaz5180.

[10] Y. Kim, S. S. Cruz, K. Lee, B. O. Alawode, C. Choi, Y. Song, J. M. Johnson, C. Heidelberger, W. Kong, S. Choi, et al., *Nature*. **2017**, *544* (7650), 340–343. https://doi.org/10.1038/nature22053.

[11] A. Koma, *Thin Solid Films*. **1992**, *216* (1), 72–76. https://doi.org/10.1016/0040-6090(92)90872-9.

[12] T. Henksmeier, J. F. Schulz, E. Kluth, M. Feneberg, R. Goldhahn, A. M. Sanchez, M. Voigt, G. Grundmeier, D. Reuter, *J Cryst Growth*. **2022**, *593*, 126756. https://doi.org/10.1016/j.jcrysgro.2022.126756.

[13] M. Deppe, Germanium Doping of Aluminum-Containing Cubic Group III-Nitride Heterostructures, Paderborn **2020**. https://doi.org/10.17619/UNIPB/1-1029

[14] K. Momma, F. Izumi, *J Appl Crystallogr*. **2011**, *44* (6), 1272–1276. https://doi.org/10.1107/S0021889811038970.

[15] J.-H. Ryou, W. Lee, in *Nitride Semiconductor Light-Emitting Diodes (LEDs)*, Elsevier **2018**. https://doi.org/10.1016/B978-0-08-101942-9.00003-4

[16] L. Y. Lee, *Materials Science and Technology*. **2017**, *33* (14), 1570–1583. https://doi.org/10.1080/02670836.2017.1300726.

[17] T. Schupp, K. Lischka, D. J. As, *J Cryst Growth*. **2010**, *312* (9), 1500–1504. https://doi.org/10.1016/j.jcrysgro.2010.01.040.

[18] F. Z. Gasmi, R. Chemam, R. Graine, B. Boubir, H. Meradji, *J Mol Model*. **2020**, *26* (12), 356. https://doi.org/10.1007/s00894-020-04614-y.

[19] P. Schley, R. Goldhahn, C. Napierala, G. Gobsch, J. Schörmann, D. J. As, K. Lischka, M. Feneberg, K. Thonke, *Semicond Sci Technol*. **2008**, *23* (5), 055001. https://doi.org/10.1088/0268-1242/23/5/055001.

[20] H. Morkoç, *Handbook of Nitride Semiconductors and Devices*, Wiley **2008**. https://doi.org/10.1002/9783527628438

[21] M. Röppischer, R. Goldhahn, G. Rossbach, P. Schley, C. Cobet, N. Esser, T. Schupp, K. Lischka, D. J. As, *J Appl Phys*. **2009**, *106* (7). https://doi.org/10.1063/1.3239516.

[22] M. Feneberg, M. Röppischer, C. Cobet, N. Esser, J. Schörmann, T. Schupp, D. J. As, F. Hörich, J. Bläsing, A. Krost, et al., *Phys Rev B*. **2012**, *85* (15), 155207. https://doi.org/10.1103/PhysRevB.85.155207.

[23] Q.-D. Zhuang, in *Nitride Semiconductor Light-Emitting Diodes (LEDs)*, Elsevier **2014**. https://doi.org/10.1533/9780857099303.1.3

[24] R. J. Iwanowski, K. Fronc, W. Paszkowicz, M. Heinonen, *J Alloys Compd*. **1999**, *286* (1–2), 143–147. https://doi.org/10.1016/S0925-8388(98)00994-3.

[25] U. W. Pohl, *Epitaxy of Semiconductors*, Springer International Publishing, Cham **2020**. https://doi.org/10.1007/978-3-030-43869-2

[26] C. Kim, I. K. Robinson, J. Myoung, K. Shim, M.-C. Yoo, K. Kim, *Appl Phys Lett*. **1996**, *69* (16), 2358–2360. https://doi.org/10.1063/1.117524.

[27] M. E. Sherwin, T. J. Drummond, *J Appl Phys*. **1991**, *69* (12), 8423–8425. https://doi.org/10.1063/1.347412.

[28] M. Frentrup, L. Y. Lee, S.-L. Sahonta, M. J. Kappers, F. Massabuau, P. Gupta, R. A. Oliver, C. J. Humphreys, D. J. Wallis, *J Phys D Appl Phys*. **2017**, *50* (43), 433002. https://doi.org/10.1088/1361-6463/aa865e.

[29] A. F. Wright, *J Appl Phys*. **1997**, *82* (10), 5259–5261. https://doi.org/10.1063/1.366393.

[30] I. Roh, S. H. Goh, Y. Meng, J. S. Kim, S. Han, Z. Xu, H. E. Lee, Y. Kim, S.-H. Bae, *Nano Converg*. **2023**, *10* (1), 20. https://doi.org/10.1186/s40580-023-00369-3.

[31] C. S. Chang, K. S. Kim, B.-I. Park, J. Choi, H. Kim, J. Jeong, M. Barone, N. Parker, S. Lee, X. Zhang, et al., *Sci Adv*. **2023**, *9* (42). https://doi.org/10.1126/sciadv.adj5379.

[32] Z. Liu, B. Liu, Z. Chen, S. Yang, Z. Liu, T. Wei, P. Gao, Z. Liu, *National Science Open*. **2023**, *2* (4), 20220068. https://doi.org/10.1360/nso/20220068.

[33] W. Kong, H. Li, K. Qiao, Y. Kim, K. Lee, Y. Nie, D. Lee, T. Osadchy, R. J. Molnar, D. K. Gaskill, et al., *Nat Mater*. **2018**, *17* (11), 999–1004. https://doi.org/10.1038/s41563-018-0176-4.

[34] H. Ryu, H. Park, J.-H. Kim, F. Ren, J. Kim, G.-H. Lee, S. J. Pearton, *Appl Phys Rev*. **2022**, *9* (3). https://doi.org/10.1063/5.0090373.

[35] D. Jang, C. Ahn, Y. Lee, S. Lee, H. Lee, D. Kim, Y. Kim, J. Park, Y. Kwon, J. Choi, et al., *Adv Mater Interfaces*. **2023**, *10* (4). https://doi.org/10.1002/admi.202201406.

[36] A. K. Geim, K. S. Novoselov, *Nat Mater*. **2007**, *6* (3), 183–191. https://doi.org/10.1038/nmat1849.

[37] D. R. Cooper, B. D'Anjou, N. Ghattamaneni, B. Harack, M. Hilke, A. Horth, N. Majlis, M. Massicotte, L. Vandsburger, E. Whiteway, et al., *ISRN Condensed Matter Physics*. **2012**, *2012*, 1–56. https://doi.org/10.5402/2012/501686.

[38] A. Summerfield, A. Davies, T. S. Cheng, V. v. Korolkov, Y. Cho, C. J. Mellor, C. T. Foxon, A. N. Khlobystov, K. Watanabe, T. Taniguchi, et al., *Sci Rep*. **2016**, *6* (1), 22440. https://doi.org/10.1038/srep22440.

[39] S. Lee, M. S. Abbas, D. Yoo, K. Lee, T. G. Fabunmi, E. Lee, I. Kim, D. Jang, S. Lee, J. Lee, et al., **2023**. https://doi.org/https://doi.org/10.48550/arXiv.2310.05127.

[40] F. Banhart, J. Kotakoski, A. V. Krasheninnikov, *ACS Nano*. **2011**, *5* (1), 26–41. https://doi.org/10.1021/nn102598m.

[41] S. Hasegawa, in *Characterization of Materials* (Ed: E. Kaufmann), Vol. 3, Wiley **2012**.

[42] Z. Ni, Y. Wang, T. Yu, Z. Shen, *Nano Res*. **2008**, *1* (4), 273–291. https://doi.org/10.1007/s12274-008-8036-1.

[43] A. C. Ferrari, J. C. Meyer, V. Scardaci, C. Casiraghi, M. Lazzeri, F. Mauri, S. Piscanec, D. Jiang, K. S. Novoselov, S. Roth, et al., *Phys Rev Lett*. **2006**, *97* (18), 187401. https://doi.org/10.1103/PhysRevLett.97.187401.

[44] T. Oeser, *Kristallstrukturanalyse Durch Röntgenbeugung*, Springer Fachmedien Wiesbaden, Wiesbaden **2019**. https://doi.org/10.1007/978-3-658-25439-1

[45] U. Köhler, A Study of Growth and Doping of Cubic Group III Nitride Structures, University Paderborn, Paderborn **2003**.

[46] L. Spieß, G. Teichert, R. Schwarzer, H. Behnken, C. Genzel, *Moderne Röntgenbeugung*, Springer Fachmedien Wiesbaden, Wiesbaden **2019**. https://doi.org/10.1007/978-3-8348-8232-5

[47] Nanosurf AG, "AFM Working Principle," available at https://www.nanosurf.com/en/support/afm-operating-principle, **2023**.

[48] J. Kamimura, M. Ramsteiner, U. Jahn, C.-Y. James Lu, A. Kikuchi, K. Kishino, H. Riechert, *J Phys D Appl Phys*. **2016**, *49* (15), 155106. https://doi.org/10.1088/0022-3727/49/15/155106.

[49] G. Nolze, R. Hielscher, A. Winkelmann, *Crystal Research and Technology*. **2017**, *52* (1). https://doi.org/10.1002/crat.201600252.

[50] A. J. Schwartz, *Electron Backscatter Diffraction in Materials Science*, Springer US, Boston, MA **2009**. https://doi.org/10.1007/978-0-387-88136-2

[51] D. K. Schroder, *Semiconductor Material and Device Characterization*, Wiley **2005**. https://doi.org/10.1002/0471749095

[52] P. J. Dean, *Progress in Crystal Growth and Characterization*. **1982**, *5* (1–2), 89–174. https://doi.org/10.1016/0146-3535(82)90010-7.

[53] J. Jimenez, J. W. Tomm, *Spectroscopic Analysis of Optoelectronic Semiconductors*, Vol. 202, Springer International Publishing, Cham **2016**. https://doi.org/10.1007/978-3-319-42349-4

[54] J. Lähnemann, U. Jahn, O. Brandt, T. Flissikowski, P. Dogan, H. T. Grahn, *J Phys D Appl Phys*. **2014**, *47* (42), 423001. https://doi.org/10.1088/0022-3727/47/42/423001.

[55] J. Schörmann, S. Potthast, D. J. As, K. Lischka, *Appl Phys Lett*. **2007**, *90* (4), 041918. https://doi.org/10.1063/1.2432293.

[56] G. Mula, C. Adelmann, S. Moehl, J. Oullier, B. Daudin, *Phys Rev B*. **2001**, *64* (19), 195406. https://doi.org/10.1103/PhysRevB.64.195406.

[57] J. Neugebauer, T. K. Zywietz, M. Scheffler, J. E. Northrup, H. Chen, R. M. Feenstra, *Phys Rev Lett*. **2003**, *90* (5), 056101. https://doi.org/10.1103/PhysRevLett.90.056101.

[58] N. Gogneau, E. Sarigiannidou, E. Monroy, S. Monnoye, H. Mank, B. Daudin, *Appl Phys Lett*. **2004**, *85* (8), 1421–1423. https://doi.org/10.1063/1.1782264.

[59] Y. Goldberg, M. Levinshtein, S. Rumyantsev, *SciTech Book News*. **2001**, *25*, 93–146. https://doi.org/10.1007/978-3-319-42349-4

[60] D. J. As, F. Schmilgus, C. Wang, B. Schöttker, D. Schikora, K. Lischka, *Appl Phys Lett*. **1997**, *70* (10), 1311–1313. https://doi.org/10.1063/1.118521.

[61] D. J. As, T. Frey, D. Schikora, K. Lischka, V. Cimalla, J. Pezoldt, R. Goldhahn, S. Kaiser, W. Gebhardt, *Appl Phys Lett*. **2000**, *76* (13), 1686–1688. https://doi.org/10.1063/1.126136.

[62] X. Li, W. Cai, J. An, S. Kim, J. Nah, D. Yang, R. Piner, A. Velamakanni, I. Jung, E. Tutuc, et al., *Science (1979)*. **2009**, *324* (5932), 1312–1314. https://doi.org/10.1126/science.1171245.

[63] A. Pirkle, J. Chan, A. Venugopal, D. Hinojos, C. W. Magnuson, S. McDonnell, L. Colombo, E. M. Vogel, R. S. Ruoff, R. M. Wallace, *Appl Phys Lett*. **2011**, *99* (12), 122108. https://doi.org/10.1063/1.3643444.

[64] Y.-D. Lim, D.-Y. Lee, T.-Z. Shen, C.-H. Ra, J.-Y. Choi, W. J. Yoo, *ACS Nano*. **2012**, *6* (5), 4410–4417. https://doi.org/10.1021/nn301093h.

[65] G. Cunge, D. Ferrah, C. Petit-Etienne, A. Davydova, H. Okuno, D. Kalita, V. Bouchiat, O. Renault, *J Appl Phys*. **2015**, *118* (12). https://doi.org/10.1063/1.4931370.

[66] M. Littmann, D. Reuter, D. J. As, *physica status solidi (b)*. **2023**, *260* (7). https://doi.org/10.1002/pssb.202300034.

[67] Y. Xiang, S. Xie, Z. Lu, X. Wen, J. Shi, M. Washington, G.-C. Wang, T.-M. Lu, *J Appl Phys*. **2021**, *130* (6), 065301. https://doi.org/10.1063/5.0057417.

[68] A. Okabe, B. Boots, K. Sugihara, *Spatial Tessellations*, John Wiley & Sons, Inc., Hoboken, NJ, USA **2000**. https://doi.org/10.1002/9780470317013

[69] R. Maria Kemper, T. Schupp, M. Häberlen, T. Niendorf, H.-J. Maier, A. Dempewolf, F. Bertram, J. Christen, R. Kirste, A. Hoffmann, et al., *J Appl Phys*. **2011**, *110* (12), 123512. https://doi.org/10.1063/1.3666050.

[70] K. Badokas, A. Kadys, J. Mickevičius, I. Ignatjev, M. Skapas, S. Stanionytė, E. Radiunas, G. Juška, T. Malinauskas, *J Phys D Appl Phys*. **2021**, *54* (20), 205103. https://doi.org/10.1088/1361-6463/abe500.

[71] Y. Kim, S. S. Cruz, K. Lee, B. O. Alawode, C. Choi, Y. Song, J. M. Johnson, C. Heidelberger, W. Kong, S. Choi, et al., *Nature*. **2017**, *544* (7650), 340–343. https://doi.org/10.1038/nature22053.

[72] D. Liang, T. Wei, J. Wang, J. Li, *Nano Energy*. **2020**, *69*, 104463. https://doi.org/10.1016/j.nanoen.2020.104463.

[73] F. Meier, M. Protte, E. Baron, M. Feneberg, R. Goldhahn, D. Reuter, D. J. As, *AIP Adv*. **2021**, *11* (7). https://doi.org/10.1063/5.0053865.

[74] J. Mullay, in *Electronegativity* (Eds: K. das Sen, C. K. Jørgensen), Springer-Verlag, Berlin/Heidelberg **1987**. https://doi.org/10.1007/BFb0029834

[75] R. Yadav, C. K. Dixit, *Journal of Science: Advanced Materials and Devices*. **2017**, *2* (2), 141–149. https://doi.org/10.1016/j.jsamd.2017.05.007.

[76] A. Ouerghi, A. Balan, C. Castelli, M. Picher, R. Belkhou, M. Eddrief, M. G. Silly, M. Marangolo, A. Shukla, F. Sirotti, *Appl Phys Lett*. **2012**, *101* (2), 021603. https://doi.org/10.1063/1.4734396.

[77] H.-H. Hsueh, S.-L. Ou, D.-S. Wuu, R.-H. Horng, *Vacuum*. **2015**, *118*, 8–12. https://doi.org/10.1016/j.vacuum.2015.02.002.

[78] T.-Y. Tsai, R.-H. Horng, D.-S. Wuu, S.-L. Ou, M.-T. Hung, H.-H. Hsueh, *Electrochemical and Solid-State Letters*. **2011**, *14* (11), H434. https://doi.org/10.1149/2.002111esl.

[79] K.-T. Lee, Y.-C. Lee, S.-H. Tu, C.-L. Lin, P.-H. Chen, C.-Y. Liu, J.-Y. Chang, *Jpn J Appl Phys*. **2008**, *47* (2R), 930. https://doi.org/10.1143/JJAP.47.930.

[80] X. Han, J. Yu, Z. Li, X. Wang, Z. Hao, Y. Luo, C. Sun, Y. Han, B. Xiong, J. Wang, et al., *ACS Appl Electron Mater*. **2022**, *4* (11), 5326–5332. https://doi.org/10.1021/acsaelm.2c00997.

[81] H. Kim, K. Lu, Y. Liu, H. S. Kum, K. S. Kim, K. Qiao, S.-H. Bae, S. Lee, Y. J. Ji, K. H. Kim, et al., *ACS Nano*. **2021**, *15* (6), 10587–10596. https://doi.org/10.1021/acsnano.1c03296.

[82] W. Kong, H. Kum, S.-H. Bae, J. Shim, H. Kim, L. Kong, Y. Meng, K. Wang, C. Kim, J. Kim, *Nat Nanotechnol*. **2019**, *14* (10), 927–938. https://doi.org/10.1038/s41565-019-0555-2.

List of Figures

List of Tables

Appendix A – Sample list

G Number	MBE Number	Substrate	Comment
	GNL2998	16CO175	580 nm c-GaN
	GNL3006	16CO175	580 nm c-GaN
G1		16CO175	Graphene transfer test
G2		16CO175	Graphene transfer test
G3		16CO175	Graphene transfer test
G4		X-6536-05	New substrate with smal roughness
G5	GNL3118	X-6536-05	First remote epitaxy test
G6	GNL3120	X-6536-05	1h growth on graphene
G7	GNL3121	X-6536-05	1h growth on graphene
G8	GNL3125	X-6536-05	1h growth on graphene
G9	GNL3128	X-6536-05	1h growth on graphene
G10	GNL3129	X-6536-05	1h growth on graphene
G11	GNL3131	X-6536-05	1h growth on graphene
G12	GNL3133	X-6536-05	Al-Flash test
G13	GNL3134	X-6536-05	Ga-Flash test
G14		X-6536-05	Sample broke in half
G15	GNL3137	X-6536-05	1h growth on graphene
G16	GNL3144	X-6536-05	1h growth on graphene
G17	GNL3145	OKM-4A-18	First test on a tilted substrate
G18	GNL3146	X-6536-05	5 min growth on graphene
G19	GNL3147	X-6536-05	10 min growth on graphene
G20	GNL3148	X-6536-05	1h growth on graphene
G21	GNL3149	X-6536-05	No growth recipe
G22	GNL3150	X-6536-05	3h sample
G23	GNL3151	X-6536-05	Half graphene covered sample
G24	GNL3152	X-6526-05	Half graphene covered sample
G25		X-6536-05	900°C thermal treatment
G26	GNL3153	X-6536-05	900°C thermal treatment
G27	GNL3154	X-6536-05	6h sample
G28	GNL3155	X-6536-05	1h sample
G29	GNL3156	X-6536-05	30 min sample
G30	GNL3157	OKM-4A-18	30 min sample
G31	GNL3159	X-6536-05	1h sample
G32	GNL3160	OKM-4A-18	1h sample
G33	GNL3161	OKM-4A-18	900°C thermal treatment
G34	GNL3162	OKM-4A-18	First sample with Graphenea graphene
G35	GNL3164	OKM-4A-19	1h sample
G36	GNL3165	OKM-4A-19	1h sample

G37	GNL3166	OKM-4A-19	1h sample
G38	GNL3168	OKM-4A-19	1h sample
G39	GNL3169	OKM-4A-19	1h sample
G40	GNL3170	OKM-4A-19	3h sample
G41	GNL3171	OKM-4A-19	1h Graphenea sample
G42	GNL3172	OKM-4A-19	Graphenea sample thermal cleaning
G43	GNL3173	OKM-4A-19	30 min Graphenea sample
G44	GNL3174	OKM-4A-19	1h sample
G45	GNL3175	OKM-4A-19	1h sample
G46	GNL3176	OKM-4A-19	3h sample
G47		OKM-4A-19	Sample broke in half
G48	GNL3178	OKM-4A-19	2h Graphenea
G49	GNL3179	OKM-4A-19	2h Graphenea
G50	GNL3180	OKM-4A-19	2h Graphenea
G51		OKM-4A-19	Graphenea Raman sample
G52		OKM-4A-19	ACS Material Raman sample
	GNL3182	OKM-4A-19	Reference sample without graphene
	GNL3183	OKM-4A-19	Reference sample without graphene
G53	GNL3184	OKM-4A-19	6h sample
	GNL3211	19CO281	Thin GaN layer as new graphene substrate
G54	GNL3212	19CO281	First remote epitaxy on new NocaSiC substrate
G55	GNL3218	19CO281	Ga cell at 930°C instead 923°C
G56	GNL3219	GNL3211	Graphene on GaN buffer (GNL3211)
	GNL3222	19CO281	10min GaN buffer
G57	GNL3223	19CO281	Ga cell at 930°C instead 923°C
G58	GNL3224	19CO281	Ga cell at 930°C instead 923°C
G59	GNL3225	GNL3222	Graphene on10min GaN buffer
	GNl3226	19CO281	N2 Plasma shut off
	ANL3229	OKM-4A-19	First AlN buffer
	ANL3231	19CO281	AlN-Buffer for G60_GNL3235
G60	GNL3235	ANL3231	Graphene on AlN Buffer
	ANL3237	19CO281	AlN-Buffer
	ANL3238	19CO281	AlN-Buffer for G61_GNL3239
G61	GNL3239	ANL3238	Graphene on AlN Buffer
G62	GNL3241	ANL3237	Graphene on AlN Buffer
	ANL3244	19CO281	AlN-Buffer
	ANL3245	19CO281	AlN-Buffer
	GNL3248	19CO281	Reference sample for G61_GNL3239 no graphene
	ANL3249	19CO281	AlN-Buffer (change of Al Temp)
	ANL3267	19CO281	AlN-Buffer
G63	GNL3269	ANL3244	Graphene on AlN buffer 300nm

G64	GNL3270	ANL3245	Graphene on AlN buffer 600nm
G65	GNL3272	ANL3267	Graphene on AlN buffer 50nm
	ANL3276	19CO281	AlN-Buffer on 2cmx2cm sample
G66	GNL3278	ANL3276-A	1h Graphene on AlN Buffer
G67	GNL3280	ANL3276-B	5 min Graphene on AlN Buffer
G68	GNL3281	ANL3276-C	3h Graphene on AlN Buffer
G69	GNL3283	ANL3276-D	15 min Graphene on AlN Buffer
	ANL3285	OKM-4A-19	Test AlN Buffer tilted substrate
G70	GNL3288	ANL3285	Test on tilted substrate
	ANL3289	19CO281	AlN-Buffer on 2cmx2cm sample
G71	GNL3291	ANL3289-A	Reference sample for GNL3288
G72	GNL3293	ANL3289-B	30 min sample
G73	GNL3294	ANL3289-C	15 min sample
	ANL3310	19CO281	AlN-Buffer on 2cmx2cm sample
	GNL3311		1h sample
G74	GNL3318	ANL3310-A	1h sample
G75	GNL3319	ANL3310-B	6h sample
	ANL3327	16CO147	First sample after MBE opening
	ANL3329	21CO68	Optimization of AlN growth parameters
	ANL3331	21CO71	Optimization of AlN growth parameters
	ANL3332	21CO71	Optimization of AlN growth parameters
	ANL3333	21CO71	Optimization of AlN growth parameters
	ANL3335	21CO71	Optimization of AlN growth parameters
	ANL3337	19CO281	AlN-Buffer on 2cmx2cm sample
	ANL3338	19CO281	AlN-Buffer on 2cmx2cm sample
G76	GNL3339	ANL3338-A	Substrate temperatur optimization
G77	GNL3340	ANL3338-B	Substrate temperatur optimization
G78	GNL3343	ANL3337-A	Substrate temperatur optimization
G79	GNL3344	ANL3337-B	Substrate temperatur optimization
	ANL3346	19CO281	AlN-Buffer on 2cmx2cm sample
G80	GNL3348	ANL3337-C	Substrate temperatur optimization
G81	GNL3349	ANL3337-D	Substrate temperatur optimization
G82	GNL3353	ANL3333	Substrate temperatur optimization
G83	GNL3356	OKM-4A-19	Substrate temperatur optimization
	GNL3357	OKM-4A-19	RHEED defekt
	GNL3358	21CO-068	Parameter optimization
	GNL3359	OKM-4A-19	Parameter optimization
	ANL3361	21CO71	Parameter optimization
	ANL3364	21CO71	Parameter optimization
	GNL3366	21CO71	2cmx2cm Parameter optimization
G84	GNL3368	ANL3361	3h sample
G85	GNL3370	ANL3364	3h sample
G86	GNL3371	ANL3366-A	3h sample

G87	ANL3375	ANL3366-B	Second AlN on Graphene
G88	ANL3376	ANL3366-C	Second AlN on Graphene
G89	GNL3378	ANL3366-D	AlN plus GaN on Graphene
	ANL3379	21CO71	AlN buffer
	ANL3381	21CO71	AlN buffer 2cmx2cm
	ANL3382	21CO71	AlN buffer 2cmx2cm
G90	GNL3387	21CO71	Test sample without AlN Buffer
G91	GNL3388	21CO71	Test sample without AlN Buffer
G92	GNL3392	ANL3379	1h sample
G93	GNL3393	ANL3382-A	1h sample
G94	GNL3394	ANL3382-B	1h sample
	ANL3397	19CO281	2cmx2cm AlN buffer
G95	GNL3398	ANL3397-A	1h sample
G96	GNL3399	ANL3397-B	1h sample
G97	GNL3400	ANL3397-C	1h sample
G98	GNL3402	ANL3397-D	1h sample
	ANL3403	21CO71	2cmx2cm AlN buffer
	ANL3404	21CO71	2cmx2cm AlN buffer
G99	GNL3405	ANL3403-A	1h sample
G100	GNL3406	ANL3403-B	1h sample
	GNL3407	21CO71	N2 Plasma optimization
G101	GNL3408	ANL3403-C	1h sample
G102	GNL3409	ANL3403-D	1h sample
	GNL3410	21CO71	N2 Plasma optimization
G103	GNL3411	ANL3404-A	1h sample
G104	GNL3413	ANL3404-B	1h sample
G105	GNL3415	ANL3404-C	1h sample

Appendix B – List of Publications

During the PhD studies, the following publications and submissions to conferences were published:

Scientific publications

- F. Meier, **M. Littmann**, J. Bürger, T. Riedl, D. Kool, J. Lindner, D. Reuter and D. J. As, (2023), Selective Area Growth of Cubic Gallium Nitride in Nanoscopic Silicon Dioxide Masks. Phys. Status Solidi B, 260: 2200508. (16 December 2022); https://doi.org/10.1002/pssb.202200508
- M. F. Zscherp, S. A. Jentsch, M. J. Müller, **M. Littmann**, F. Meier, D. M. Hofmann, D. J. As, S. Chatterjee, J. Schörmann, Growth of cubic InxGa1-xN over whole composition by MBE. Proc. SPIE 12421, Gallium Nitride Materials and Devices XVIII, 124210B. (15 March 2023); https://doi.org/10.1117/12.2648296
- **M. Littmann**, D. Reuter, and D. J. As, (2023), Remote Epitaxy of Cubic Gallium Nitride on Graphene-Covered 3C-SiC Substrates by Plasma-Assisted Molecular Beam Epitaxy. Phys. Status Solidi B, 260: 2300034. (23 March 2023); https://doi.org/10.1002/pssb.202300034
- M. F. Zscherp, S. A. Jentsch, M. J. Müller, V. Lider, C. Becker, L. Chen, **M. Littmann**, F. Meier, A. Beyer, D. M. Hofmann, D. J. As, P. J. Klar, K. Volz, S. Chatterjee, J. Schörmann, Overcoming the Miscibility Gap of GaN/InN in MBE Growth of Cubic InGaN. ACS Applied Materials & Interfaces 2023 15 (33), 39513-39522. (2 August 2023); https://doi.org/10.1021/acsami.3c06319

Submission to conferences

- **M. Littmann**, D. Reuter, D. J. As, Remote epitaxy of cubic gallium nitride on graphene/3C-SiC substrates, DGKK/DEMBE 2022, (16-18 May 2022), Bremen, Germany
- **M. Littmann**, D. Reuter, D. J. As, Challenges of remote epitaxy of cubic gallium nitride by plasma-assisted molecular beam epitaxy, ICMBE 2022, (4-9 September 2022), Sheffield, United Kingdom

- **M. Littmann**, O. August, K. Harnisch, T. Halle, F. Bertram, J. Christen, D. Reuter, D. J. As, Cubic GaN epilayers grown by Remote Epitaxy on Graphene covered 3C-SiC(001)/Si(001) substrates, ICNS14, (12-17 November 2023), Fukuoka, Japan
- M. F. Zscherp, S. A. Jentsch, M. J. Müller, V. Lider, C. Becker, L. Chen, **M. Littmann**, F. Meier, A. Beyer, D. M. Hofmann, D. J. As, P. J. Klar, K. Volz, S. Chatterjee, J. Schörmann, MBE growth of cubic InGaN over the entire GaN/InN compositions range, ICNS14, (12-17 November 2023), Fukuoka, Japan

Acknowledgements

I want to extend my gratitude to Prof. Dr. Donat J. As and Prof. Dr. Dirk Reuter for providing me with the opportunity to work on this dissertation. I want to thank both of them for their invaluable scientific advice throughout my research journey.

I also want to thank the Co-Reviewers, Prof. Dr. Cedrik Meier, Prof. Dr. Wolf Gero Schmidt, and Dr. Ronja Köthemann, for their time and effort in reading my thesis.

I would like to specifically acknowledge Dr. Falco Meier for the helpful discussions and the support in maintaining our equipment.

I thank my collaboration partners for their helpful measurements. I thank Elias Kluth of the group of Prof. Rüdiger Goldhahn from the Otto von Guericke University Magdeburg for the Raman spectroscopy measurements. I am grateful for the EBSD measurements performed by Olga Augst of the group of Prof. Jürgen Christen from Otto von Guericke University Magdeburg.

Lastly, I would like to express my gratitude to all of my colleagues for their support, especially Dr. Tobias Henksmeier, Dennis Deutsch, Normen Auler, Pascal Mahler, and Bastian Aisenbrey.

Erklärung der Selbständigkeit

Hiermit versichere ich, Mario Littmann, die vorliegende Arbeit selbständig verfasst und keine anderen als die angegebenen Quellen und Hilfsmittel benutzt, sowie die Zitate kenntlich gemacht zu haben.

Paderborn, 1. März 2024 Mario Littmann